Technische Universität München
Faculty of Physics

Master's Thesis in Physics

The Decaying Dark Matter Model and Large-Scale Structure Formation

Lea Fuß

supervised by
PD Dr. Mathias Garny

April 11, 2022

First Examiner: PD Dr. Mathias Garny

Second Examiner: Prof. Dr. Alejandro Ibarra

Abstract

Decaying Cold Dark Matter (DCDM) is a model that is currently under investigation regarding primarily the σ_8 tension between cosmological and local measurements. Recent papers suggest that the tension can be lessened, however, no preference over ΛCDM is found. We want to contribute to these studies by following a different approach than in other works. We use Lyman-α forest data from BOSS together with a model where we find an expression of the one-dimensional flux power spectrum via the matter power spectrum up to 1-loop corrections. This model can then be fitted to the data and exclusion bounds can be extracted. We test this method at first for warm dark matter (WDM) which provides us with reasonable bounds on the more conservative side. After studying the background evolution of DCDM, we then apply the fitting method to it. We find, that we can provide tighter constraints for the upper lifetime in the $\epsilon \sim 0.001 - 0.005$ regime with $\tau \gtrsim 18$Gyrs, which can be attributed to our treatment of non-linearities. In the larger ϵ regimes, our method performs worse since we don't include an in-depth analysis of CMB data. Regarding the σ_8 tension, we observe, that our model allows for lower values and doesn't put much constraints on it. As the final word on DCDM is not yet spoken, we are curios for the future of it with regard to upcoming surveys.

Acknowledgments

At first, I want to thank my supervisor PD Dr. Mathias Garny for his helpful guidance and mentoring during the last year. He always makes time for questions and discussions which is why I look forward to keep working with him.
Then, I want to thank the developers of the modified CLASS code I am using, for their kind help. Especially Guillermo F. Abellán, who always answered all of my questions and gave me code instructions was of much assistance.
Lastly, I thank Petter Taule who also provided me with code, which was used for computing the non-linear spectra, as well as instructions for it.

Contents

1 | Introduction

The standard model of cosmology known as ΛCDM is a very successful model in explaining the large scale structure (LSS) of the universe. At the heart of this sits cold dark matter (CDM) which causes the typical bottom-to-top structure formation we see in the LSS by being non-relativistic during the clustering process. Despite the success of CDM, there are still unresolved issues that are hinting that there may be more. This sparks of course interest in different cosmological models that are able to address these issues. Mostly the two large unknowns, meaning dark energy or dark matter, are altered in some way to try and achieve better results. The challenge hereby lies in conserving the winning properties of ΛCDM on larger scales while still tackling problems of todays cosmology. These are mainly given by three larger issues [1].
The first one is the Hubble tension [2] which arises between mostly cosmic microwave background (CMB) and supernovae data. CMB data from Planck with $H_0 = 67.27 \pm 0.60$km/(sMpc) [3] is an example of a probe of the early universe since it relies on the recombination time. More precisely, it measures the angular scale of the sound horizon. Values derived by other CMB independent early universe probes like the Big Bang Nucleosynthesis (BBN) and baryonic acoustic oscillations (BAOs) also tend towards lower H_0 values [4, 5]. This makes it even more worrying that methods of inferring H_0 directly, arrive at a much larger value resulting in a 4 to 6σ tension. SHOES for example, measures $H_0 = 73.2 \pm 1.2$km/(sMpc) [6], which is based on a calibration of the cosmic distance ladder using Cepheids. Again, other methods based on supernovae with e.g. calibrating the tip of the red giant branch or even methods not based on supernovae tend to higher values, hinting at either unknown systematic errors, like for example dust modeling in SN1a, or a problem with the cosmological model [7]. Systematic errors seem unlikely at this point regarding this large number of independent measurements. If so, a single source of uncertainty will probably not suffice [5]. More interesting are new cosmological models. Possible solutions either try to alter the early universe and the sound horizon or they focus on the late universe. Early universe solutions like early dark energy seem the most promising, however, their preference relies on the included datasets [2].
The second problem is the weaker but still unexplained tension for σ_8, which is a measure of the amplitude of matter fluctuations at a scale of 8Mpc/h. Usually, it is additionally given in terms of $S_8 = \sigma_8\sqrt{\Omega_m/0.3}$ that also includes the matter density Ω_m. Similar to Hubble, the $2-3\sigma$ tension arises between early universe cosmological data preferring larger values of S_8, and local, low redshift measurements tending towards lower values [1, 8]. CMB measures by

e.g. Planck are at $S_8 = 0.834 \pm 0.016$ [3] which also perfectly coincides with other CMB data like from ACT [9]. On the other hand, weak gravitational lensing surveys provide constraints via cosmic shear and galaxy clustering with e.g. $S_8 = 0.759^{+0.024}_{-0.021}$ from the Kilo-Degree Survey KiDS-1000 [10]. Other similar measurements [11, 12] might not produce such large deviations but they are still significantly lower compared to CMB data. To account for this, there either needs to be some unknown systematic error or alternatives to ΛCDM where proposed models need some kind of suppression of the matter power spectrum in the $k \sim 0.1 - 1\text{h/Mpc}$ regime. This can be achieved in multiple ways [8] with for example interacting dark energy models [13], massive neutrinos [14], cannibal DM [15], decaying CDM [16] and many more. Currently, there is no model which can ease the tension completely but even more in depth investigations based on newer surveys in the future will hopefully help shedding some light on this issue.
Lastly, there are several incongruities regarding the simulation and observation of structure on smaller scales [17]. These include the cusp-core problem of DM halos, where the inner densities are less dense and less cuspy when determined by e.g. rotation curves [18] compared to simulations. Another one is the famous missing satellite problem which addresses the larger number of predicted satellite galaxies compared to how many are actually observed. Even if one argues that we may not be able to see all of them since they are lacking visible stars, this still leads to another famous problem. Called 'Too Big To Fail', it states that predicted satellites are too massive to not include stars we can observe. These issues rely on numerical simulations that, while being a powerful cosmological tool, often don't include the more complex baryonic physics like stellar feedback and tidal effects which are able to alter and ease the observed properties [19, 20, 17]. Further advancement in hydrodynamical simulations will therefore be crucial in studying such effects. Apart from such explanations, DM and its properties can also provide solutions [21, 17]. One possibility is decreasing the DM fluctuation on small scales which damps halo substructure and lowers their central densities. Another way is to consider self interactions of DM (SIDM). Depending on its cross section, these could produce less cuspy density cores and also lower the number of observed halos [22, 23].

A combined effort of observations in astrophysics, numerical simulations including baryonic processes and theoretical work will be needed to ultimately solve such questions which makes the next decades promising to look forward to.
Overall, we can see that a model with some kind of suppression on the smaller scales is a popular idea for tackling several cosmological issues. While not very promising regarding the Hubble tension, σ_8 and deviating halo and galaxy properties prove very interesting to study. A suppression can be achieved in many ways, with for example the well known warm dark matter (WDM) model. Its larger free streaming length inhibits structure growth and causes a cutoff on small scales. A similar effect can be achieved by a decaying dark matter model with one massless and one massive daughter particle taking the part of WDM. Such a model has the additional advantage of being flexible in time, depending on the decay width of the mother particle. Thus, it can keep the early universe almost completely unaffected, conserving the LSS and background evolution, while still allowing for a reduction at small scales. Since it can still affect the

background and thus H_0, it was also previously discussed regarding the Hubble tension. Even when not considering cosmological problems, it is still interesting to try and constrain meaningful properties like the lifetime of DM. Especially regarding how little we know about the actual nature of DM, as well as the fact that very few particles are naturally stable [24], the scope at which decaying DM is compatible with ΛCDM is very study worthy.

The goal of this thesis is to ultimately study the large and small-scale structure formation of a decaying cold dark matter (DCDM) model with regard to Lyman-α BOSS data. The biggest issue for such data sets is the extraction of the actual matter fluctuations from the measured flux power spectrum since it requires a modeling of the complex intergalactic medium (IGM). We use a physically well motivated model relating the power spectra to the data which leaves overall six parameters free to capture the complicated IGM behavior and the non-linearities among other things. Nonetheless, we include non-linear corrections for the power spectra in order to sufficiently describe the smaller scales. To generate them, we make use of a newly developed modified CLASS code [16] and use cosmological perturbation theory for computing the 1-loop spectra. This then allows us to determine robust constraints on first WDM masses and then DCDM parameters.

The structure of this work is now as follows: First, we give an overview of the formalism of DCDM, the basic background dynamics and the work that has already been done regarding this model. Then, we explain our data set and the fitting model we will use, as well as our handling with the non-linearities arising for small scales. Afterwards, our ΛCDM reference model is fitted to the data and different aspects and variations of the method are discussed. This is followed by an analysis of the fit and its variations regarding a warm dark matter model which serves mainly as a test for our method. It is completed by an extraction of mass constraints that are evaluated.

The last main point finally deals with DCDM. We make a more detailed discussion about the background evolution and the power spectra before we use the latter in several fits. Lastly, we present our resulting constraints and set them in context with other measurements.

2 | Review of Decaying Cold Dark Matter

At first, we will now start to give an overview of the Decaying Cold Dark Matter (DCDM) model we want to study. That includes explaining the model and its parameters, the changes in the background dynamics and discussing the current state of investigations.

2.1 Mathematical Description

The general idea is that of ordinary collisonless cold dark matter particles that aren't stable and are instead decaying into two components. One is warm dark matter (WDM) whereas the other is dark radiation (DR). To describe this model mathematically, we mostly follow [16, 25, 26]. The ratio characterizing how much energy goes into the DR compared to the WDM is given by

$$\epsilon = \frac{1}{2}\left(1 - \frac{m_{wdm}^2}{m_{dcdm}^2}\right). \tag{2.1}$$

In the case of $m_{wdm} \to m_{dcdm}$ – so $\epsilon = 0$ – the daughter particle has the same mass as the mother particle and therefore no energy is transferred to DR which would of course correspond to ΛCDM. In the opposite case of $m_{wdm} \to 0$ – so $\epsilon = 0.5$ – only dark radiation is produced. This corresponds to a decay into only massless daughters and is also separately studied in the literature. The second parameter describing DCDM is the decay time τ or Γ^{-1} with $\tau \to \infty$ leading again to ΛCDM.

For the formalism, we use a synchronous gauge which is co-moving with the mother particle, so we have $P_{dcdm} = (m_{dcdm}, 0)$, $P_{wdm} = (\sqrt{m_{wdm}^2 + p^2}, \vec{p})$ and $P_{dr} = (p, -\vec{p})$. Therefore, we can calculate the maximum momentum of the daughter particles:

$$\begin{aligned} m_{dcdm} &= \sqrt{m_{wdm}^2 + p^2} + p \\ \Rightarrow p_{max} &= \frac{1}{2m_{dcdm}}(m_{dcdm}^2 - m_{wdm}^2) = m_{dcdm}\epsilon. \end{aligned} \tag{2.2}$$

The density parameter of DCDM today at t_0 is given by an initial density times an exponential factor describing the decay

$$\Omega_{dcdm}^0 = \Omega_{dcdm}^{ini} e^{-\Gamma t_0} = \frac{\rho(t_0)}{\rho_{\text{crit},0}} \tag{2.3}$$

with the critical density today, $\rho_{\text{crit},0}$. The density at an arbitrary time is in turn given by

$$\rho_{dcdm} = \rho_{\text{crit},0}\Omega_{dcdm}^{ini} e^{-\Gamma t} a^{-3} = m_{dcdm} \bar{N} a^{-3} \tag{2.4}$$

where a^{-3} gives the additional expansion factor. It can alternatively be written as the time dependent number density $\bar{N}_{dcdm} = \frac{\Omega_{dcdm}^{ini}\rho_{\text{crit},0}}{m_{dcdm}} e^{-\Gamma t}$ times the energy of the mother particle expanding in time. Now, we can look at the Boltzmann equations which in general relates the total time derivative of the phase-space-distribution to the collision term describing for example scattering events or in our case the decay. In our model they are given by

$$\begin{aligned} \dot{\bar{f}}_{dcdm} &= -a\Gamma \bar{f}_{dcdm} \quad \text{and} \\ \dot{\bar{f}}_{dr} = \dot{\bar{f}}_{wdm} &= \frac{a\Gamma \bar{N}_{dcdm}}{4\pi q^2}\delta(q - ap_{max}). \end{aligned} \tag{2.5}$$

The collision term for DCDM is only depending on Γ due to the exponential decay. The scale factor a comes from switching to conformal time with $\mathrm{d}\tau = \mathrm{d}t/a$. For WDM and DR, the collision term has the opposite sign and the energy transferred to them is proportional to the number density $\bar{N}$ of DCDM and a factor of $1/q^2$. The momentum q is determined by the delta function to ap_{max}, the momentum transferred to the daughter particles.
The phase-space-distribution is related to the mean energy density $\bar{\rho}$ and pressure $\bar{P}$ by the integrals

$$\begin{aligned} \bar{\rho} &= \frac{1}{a^4}\int_0^\infty \mathrm{d}q 4\pi q^2 E \bar{f} \quad \text{and} \\ \bar{P} &= \frac{1}{3a^4}\int_0^\infty \mathrm{d}q 4\pi q^2 \frac{q^2}{E}\bar{f}. \end{aligned} \tag{2.6}$$

$E = \sqrt{m^2a^2 + q^2}$ is here the co-moving energy and – in the case of DCDM – reduces to $E_{dcdm} = m_{dcdm}$ due to our gauge choice. Making use of these definitions, we can transform the Boltzmann equations to

$$\dot{\bar{\rho}}_{dcdm} = -3\mathcal{H}\bar{\rho}_{dcdm} - a\Gamma\bar{\rho}_{dcdm}, \tag{2.7}$$
$$\dot{\bar{\rho}}_{dr} = -4\mathcal{H}\bar{\rho}_{dr} + \epsilon a\Gamma\bar{\rho}_{dcdm}, \tag{2.8}$$
$$\dot{\bar{\rho}}_{wdm} = -3(1+\omega)\mathcal{H}\bar{\rho}_{wdm} + (1-\epsilon)a\Gamma\bar{\rho}_{dcdm}, \tag{2.9}$$

with the equation-of-state parameter $\omega = \frac{\bar{P}_{wdm}}{\bar{\rho}_{wdm}}$ for WDM. The more detailed derivations can be found in appendix B.1.1.
Solving these coupled equations is not completely straight forward but for a numerical solution we can bring it in a different form (see cite2021PhRvD.104l3533A. For this, we start again with equation 2.5 for at first WDM and rewrite the delta function. Since the co-moving momentum is given by $q = a(\tau_q)p_{max}$ with τ_q being the time the daughter particles with q are produced, we can write

$$\delta(q - ap_{max}) = \delta((a(\tau_q) - a(\tau))p_{max}) = \frac{\delta(\tau - \tau_q)}{\dot{a}(\tau_q)p_{max}} = \frac{\delta(\tau - \tau_q)}{\mathcal{H}_q q}. \tag{2.10}$$

The subscript $_q$ will now be used to indicate τ_q. Integrating over τ, we then get

$$\begin{aligned}\int \mathrm{d}\tau \dot{\bar{f}}_{wdm} &= \int \mathrm{d}\tau \frac{a\Gamma\bar{N}}{4\pi q^2}\frac{\delta(\tau-\tau_q)}{\mathcal{H}_q q} \\ \bar{f}_{wdm} &= \frac{a_q\Gamma\bar{N}}{4\pi q^2}\frac{1}{\mathcal{H}_q q}.\end{aligned}$$

Now, we multiply by $\frac{4\pi q^2 E}{a^4}$ and integrate over q:

$$\begin{aligned}\bar{\rho}_{wdm}(a) &= \int \mathrm{d}q \frac{a_q\Gamma\bar{N}_q}{\mathcal{H}_q a^4}\frac{\sqrt{m_{wdm}^2 a^2+q^2}}{q} \\ &= \frac{C}{a^4}\int \mathrm{d}q \frac{e^{-\Gamma t_q}}{\mathcal{H}_q}\frac{m_{wdm}^2 a^2 + a_q^2\epsilon^2 m_{dcdm}^2}{m_{dcdm}^2\epsilon} \\ &= \frac{C}{a^4}\int_0^a \mathrm{d}a_q \frac{e^{-\Gamma t_q}}{\mathcal{H}_q}\sqrt{\epsilon^2 a_q^2 + (1-2\epsilon)a^2}\end{aligned}$$

In the second step we used the short notation $C = \rho_{\mathrm{crit},0}\Omega_{dcdm}^{ini}\Gamma$ and in the next step we switched to the new variable a_q with $\mathrm{d}q = \epsilon m_{dcdm}\mathrm{d}a_q$. In the case of DR, we lack the mass and thus the result changes to

$$\bar{\rho}_{dr}(a) = \frac{C}{a^4}\int_0^a \mathrm{d}a_q \frac{e^{-\Gamma t_q}}{\mathcal{H}_q}\epsilon a_q. \tag{2.11}$$

Together with the equation for DCDM 2.4, we now have a set of equations that can be solved iteratively. The only two other quantities needed, are the Hubble parameter $\mathcal{H} = aH_0\sqrt{\Omega_\Lambda + \Omega_m a^{-3} + \Omega_r a^{-4}}$ and the time $t = \int_0^a \frac{\mathrm{d}a'}{\mathcal{H}'}$. Ω_m means here all matter species, Ω_r all relativistic species and Ω_Λ dark energy. With this setup, we can now solve for the densities. More details on the implementation of this solution can be found in appendix B.1.2.

The resulting densities for DCDM, WDM and DR for the parameters $\epsilon = 0.01$ and $\tau = 20$Gyrs in purple as well as $\epsilon = 0.3$ and $\tau = 1$Gyrs in orange can be seen in Figure 2.1. The black line indicates the evolution of normal cold dark matter without any decays. In both parameter cases, the DCDM density traces the CDM one since the model should and does resemble ΛCDM for large z. For the lower τ, the decrease of DCDM and increase of the daughter particles starts much earlier. Additionally, for a higher ϵ, WDM and DR evolve more closely together. Depending on the parameters, the matter content can be manipulated very subtly or strongly, affecting in turn the matter power spectrum.

Another change is visible for the Hubble rate which is plotted in Figure 2.2 for the same parameter cases as above. In the first case, with the lifetime being larger than the age of the universe and a not too large ϵ, $\mathcal{H}(z)$ almost perfectly traces the one of ΛCDM. In the second case however, the extremely short lifetime and large ϵ cause a visible deviation of $\mathcal{H}(z)$. Since H_0 was fixed in the solution, it also converges to ΛCDM for high and low z. In between, we have a decrease. This is a result of gradually replacing matter with dark radiation, which scales with a^{-4} instead of a^{-3}. Since this happens during matter domination, the energy content decreases. To keep the sum of all energy densities at 1, Ω_Λ will be corrected upwards. Whereas $\Omega_\Lambda \sim 0.69$ for the first case, we have $\Omega_\Lambda \sim 0.77$ in the second, more extreme case.

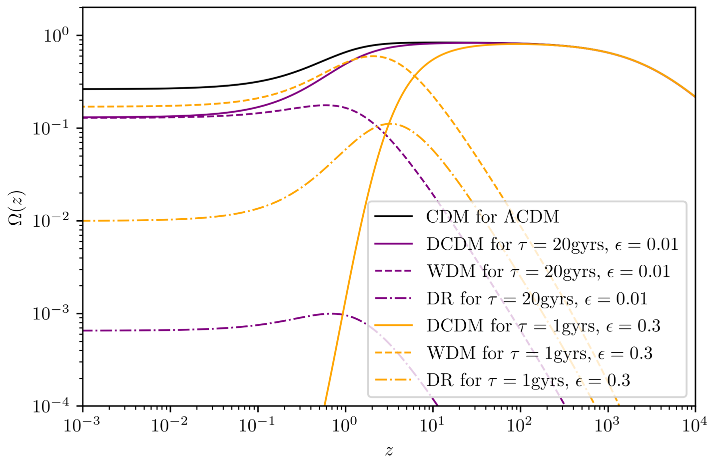

Figure 2.1: Evolution of the densities for DCDM, WDM and DR with redshift z for two different parameter sets. For comparison, CDM without any decay is plotted in black. For large z the CDM density is traced by DCDM.

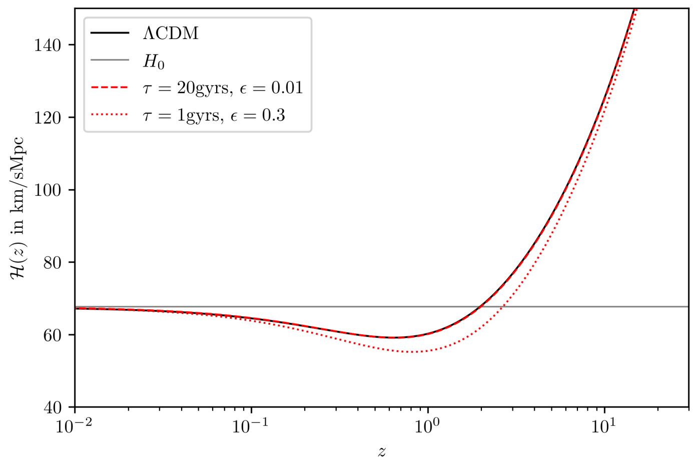

Figure 2.2: The conformal Hubble rate $\mathcal{H}(z)$ with redshift z for two different parameter sets. For large and small z, the ΛCDM case is again traced. For intermediate values, a decrease of $\mathcal{H}$ is possible for large ϵ and short τ.

The deviating matter densities induce of course also a change in the matter power spectrum, namely a suppression with its scale and depth being determined by ϵ and τ. They are discussed in detail in the DCDM section later on. Nonetheless, to give a general idea, the matter power spectrum for $\epsilon = 0.001, 0.01$ and $\tau = 20$Gyrs normalized to ΛCDM at a redshift of $z = 3.0$ is shown in Figure 2.3. The suppression on small scales is clearly visible and the reason why DCDM is discussed regarding cosmological problems.

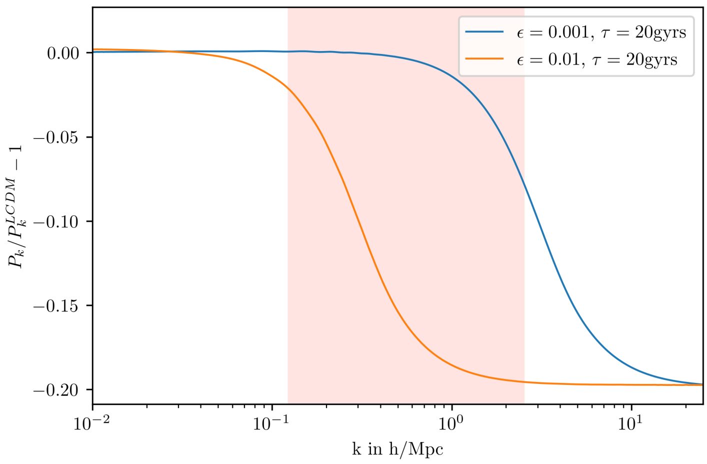

Figure 2.3: The matter power spectrum normalized to ΛCDM at a redshift of $z = 3.0$ for two different ϵ at the same τ. A suppression depending on the parameters is clearly visible.

2.2 State of Decaying Dark Matter and Constraints

Since we already talked about the current challenges in cosmology, we now want to focus on the discussions regarding variations of decaying dark matter models and their resulting constraints.
There are mainly two different kind of models, one describing a decay into only relativistic particles and the other one including two daughter particles where one is massless and the other massive. They are of course related since the first one corresponds to the limit of $\epsilon \to 0.5$ in the second one. Therefore, both were studied regarding the Hubble and S_8 tension, especially in recent years. Usually, these are done with Monte Carlo Markov Chain (MCMC) algorithms that are applied to different datasets but are mostly including CMB and BAO data.

Work regarding the sole decay into DR started a bit earlier than the more complicated 2-body decay scenarios. General discussions about the lifetime of DM were for example done in [24]. They focus on the gravitational implications and compute the change in the background evolution. They then apply an MCMC algorithm to CMB and BAO data to arrive at a lower bound of $\tau > 160$ Gyrs. A similar study using additional weak lensing data and also considering non-linearities in their analysis, derives a weaker bound of $\tau \geq 97$Gyrs [27]. Only for solely CMB data their value is competitive with $\tau \geq 140$Gyrs. Regarding the σ_8 tension, they actually find a substantial alleviation which seemed promising but is challenged by later papers. These often study a variation of this model which allows for an additional parameter f describing the ratio of DM that undergoes the decay. This allows for more freedom and can describe either a 2-body decay, if one daughter is cold again, or DM composed of multiple particles that are partly unstable. Studied e.g. in [28, 29], it was found that they don't seem to solve the Hubble or σ_8 tension. The latest work for this model [30] confirms this even more while also providing tight contraints. For short lifetimes, they find $f < 2.16\%$ and for $f \to 1$ the lower bound of $\tau > 250$Gyrs. For specifically $f = 1$, the unresolving of the Hubble tension was also validated in [31]. Overall, the decay into purely DR will most likely not be able to solve cosmological tensions and requires minimum lifetimes of around ~ 200Gyrs.

Regarding now our model with a 2-body decay into WDM and DR, the results are similar for the Hubble tension, meaning it is probably not to be resolved with DCDM [32, 33, 34]. Regarding the σ_8 tension, it is however not so clear. While [34] suggests that this tension can also not be addressed, [35], which includes a better treatment of perturbations, finds that it actually can be solved for $\tau \sim 55$Gyrs and $\epsilon \sim 0.7\%$. In two follow-up papers the authors of [35] make use of a newly developed code for much faster computation of the DCDM power spectra. This allows for a more in depth analysis, like in [16], where they also find a mild preference for DCDM which depends on the used measurements for S_8. The latest paper [30] which was only published last month, then also includes a treatment of non-linear effects. They find again that DCDM can explain lower S_8 values but is still not preferred over ΛCDM. In the best fit model they also find the stronger estimatinos of $\tau \sim 120$Gyrs when including their non-linear treatment compared to $\tau \sim 43$Gyrs without.

While these constraints are all derived using MCMC methods with CMB, BAO and further datasets, there is also the possibility to study DCDM via galaxy and halo properties with more regards towards the small scale problems. For a decay into pure DR, [36] argues for example that a decay for half of the DM particles can result in lower inner halo densities and a lower number of visible dwarf galaxies. For DCDM with 2 daughter particles, [37] tries to connect the model to the observed population of the Milky Way satellites. More precisely, they look at three different properties that are affected by DCDM and use them for constraining the parameters. These properties are M_{300} – the mass inside of a 300pc radius – , the maximum circular velocity of the satellites, and stellar properties. Combining numerical and semi-analytic methods, they find that the best constraints originate from the number of satellites with certain M_{300} and arrive at $\tau \gtrsim 30$Gyrs for $20 \lesssim v_k \lesssim 200$km/s. Instead of ϵ, they use the so-called kick-velocity $v_k \sim \epsilon c$ which is transferred to the daughter particles during the decay. In [38], they build up on this work and also use Milky Way Satellite Galaxies for deriving their constraints. They exclude $\tau < 18$Gyrs for $v_k = 20$km/s which means they are extremely sensitive to the low ϵ regime which still affects the halo distribution and substructure. These are overall conservative bounds, so future studies will tighten this range even more.

Overall, a lot of studies of decaying DM models have been published in only recent years, so a final statement regarding DCDM is not yet spoken. In summary, the current investigations suggests, that DCDM may not be preferred over ΛCDM and can't account for the Hubble tension. The σ_8 tension however, seems to be improved. Additionally, it is compatible for sufficient lifetimes. Thus, it is not ruled out yet and is maybe not a strongly preferred, but still a viable option. Since this model is still under investigation, further studies will

hopefully be able to more strongly prefer or reject the model.
A large role will probably be played by future surveys providing more accurate weak lensing, BAO and galaxy clustering measurements [39]. Examples are the upcoming survey by the Rubin Observatory/LSST, scheduled to go into operation in 2023 [40, 41], the Dark Energy Spectroscopic Instrument (DESI) studying growth of structure via redshift-space distortions as well as BAOs [42], and the Euclid satellite focusing on weak lensing and also BAO measurements [43]. They will constrain observables like the growth function with more accuracy and thus be helpful for studying DCDM among other models.

We want to contribute to all these studies by following a slightly different approach which is based on BOSS data from the Lyman-α forest at $z = 3.0 - 4.2$ in the mildly non-linear regime. This method, which includes non-linear corrections, will be explained in the next section.

3 | Fitting Model

3.1 BOSS Data

For inferring matter distributions in our universe, the Lyman-α forest is a powerful tool for precise cosmological measurements in a relatively high redshift regime [44, 45]. The name refers to a series of close absorption lines that are visible when measuring a spectra from quasistellar objects (QSOs), e.g from a quasar, which resembles a forest. These lines are a product of photons from the QSO passing through hydrogen clouds in the IGM. If the photons exite the famous Lyman-α transition, a typical absorption line is produced. Since there are several clouds in the line of sight and they are spatially separated, the absorption lines will also exhibit a shift depending on the redshift of the original transition. A typical flux spectrum can be seen in Picture 3.1 which was taken from [46]. They, in turn, use data from the Baryon Oscillation Spectroscopic Survey (BOSS) and the first extended-BOSS (eBOSS) quasars which are included in fourteenth data release of the Sloan Digital Sky Survey (SDSS) [47]. The forest shape is clearly visible between the Ly-α and Ly-β peaks.

Measurements of the Ly-α forest can be useful for two points. At first, it

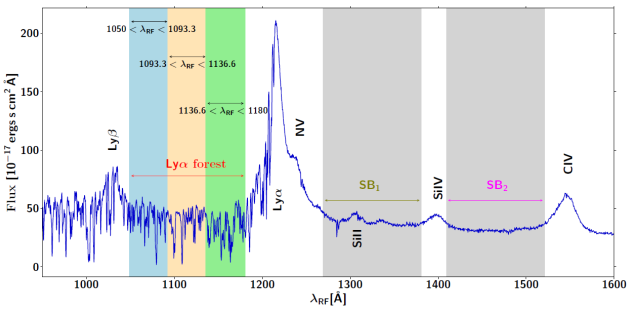

Figure 3.1: A typical flux spectrum when measuring a bright quasar taken from [46]. Between he larger Ly-α and Ly-β peaks, a series of absorption lines makes up the Ly-α forest. The grey side bands are used in the computation of the 1D flux power spectrum.

can help studying the photo-ionized warm intergalactic medium (IGM) which is quite complex and can only be studied by few observations or numerical simulations. This is usually done with high-resolution data for small-scales like the one by e.g. HIRES (High Resolution Echelle Spectograph) from the KECK ob-

servatory [48] and offers constraints for the thermal state of the IGM. Secondly, the forest is used to study the cosmological large-scale structure. Mid-resolution data, which includes larger k modes, is better suited in this case. Such data is provided by the SDSS in the form of BOSS and eBOSS data. We are overall interested in the small-scales but we also have to deal with the non-linearities in order to get reliable results. The advantage of the BOSS data we will use, is that they lie in the only weakly non-linear regime for its redshifts $z = 2.2, 2.4, ..., 4.6$. Higher strongly non-linear k modes are still having an influence on the integration of the line of sight but for the relevant scales of $k \sim 0.001 - 0.02$ s/km this effect should be manageable with additional parameters. Thus, the scales of the BOSS data are better suited for our model.
Extracting the actual 1D flux power spectrum from the data is studied well as in [49, 50, 46, 51] and we use the spectrum from [52] based on the ninth release of the BOSS data [53]. The dimensionless spectrum for all relevant redshifts we want to fit to, can be seen in Figure 3.2. We constricted ourselves to only redshifts from $z = 3.0 - 4.2$ following the approach in [54], which argues that lower redshifts are more sensitive to non-linearities and higher redshifts to the reionization process which increases the error. [55, 56].

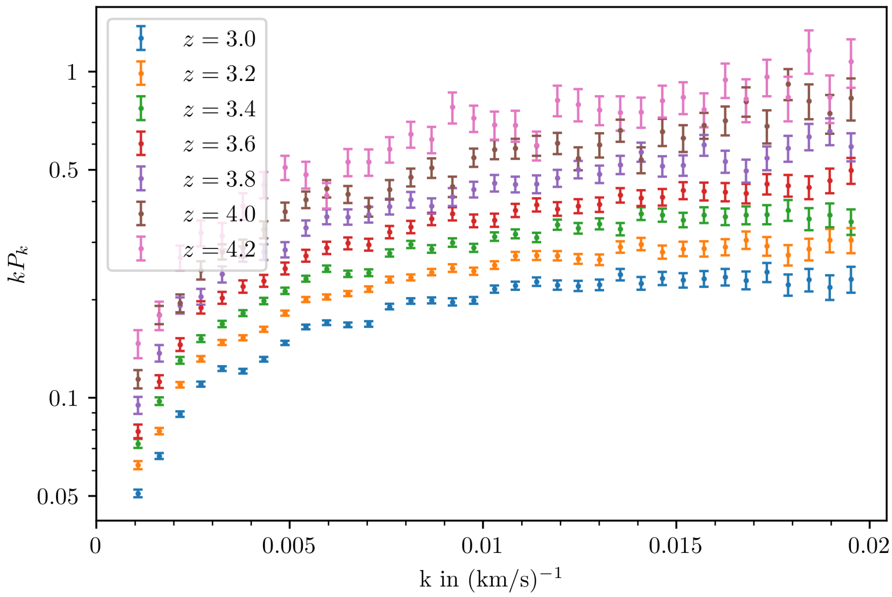

Figure 3.2: 1D flux power spectrum based on BOSS data [52] for all redshifts and with errorbars.

3.2 Modeling the one-dimensional Flux Power Spectrum

Our end goal is to model the one-dimensional flux power spectrum from the three-dimensional matter power spectrum. For this we follow the model described in [54, 57] and summarize here their approach.

The flux is determined by the transmission F which is depending on the optical depth τ via the typical exponential law $F = e^{-\tau}$. In particular we are interested in the fluctuations in the transmission spectrum, so

$$\delta_F = \frac{F}{\overline{F}} - 1, \tag{3.1}$$

where $\overline{F}$ is the average transmission. Since the hydrogen clouds usually don't have large pressure gradients compared to the gravitational forces, the underlying matter over- or under-densities are traced pretty well. Therefore the optical depth and hence the transmission depend largely on the matter fluctuations δ. Additionally, we have to account for gravitational collapse, by looking at the peculiar velocity v_p and its gradient along the line of sight. This is described by a dependency on the dimensionless quantity

$$\eta = -\frac{1}{aH}\frac{\partial v_p}{\partial x_p} \tag{3.2}$$

with the co-moving coordinate x_p. Dividing by aH sets the gradient in reference to the Hubble acceleration and cancels the units. Now, we can at first rewrite the optical depth contrast at linear order to

$$\delta_\tau = \frac{\tau(\delta, \eta)}{\overline{\tau}} - 1 = \frac{\overline{\tau} + \frac{\partial\tau}{\partial\delta}\delta + \frac{\partial\tau}{\partial\eta}\eta}{\overline{\tau}} - 1 = b_{\tau\delta}\delta + b_{\tau\eta}\delta, \tag{3.3}$$

where we introduced the proportionality parameters $b_{\tau\delta}$ and $b_{\tau\eta}$. Applied to the transmission, we then get

$$\begin{aligned}\delta_F &= \frac{e^{-\tau}(1+\delta_\tau)}{e^{-\tau}} - 1 \\ &= \frac{\partial\delta_F}{\partial\delta_\tau}\delta_\tau = -\overline{\tau}\delta_\tau = \log\left(\overline{F}\right)\delta_\tau \\ &= b_{F\delta}\delta + b_{F\eta}\delta \end{aligned} \tag{3.4}$$

with the new parameters $b_{F\square} = \log\left(\overline{F}\right)b_{\tau\square}$.
Now we can compute the three-dimensional flux power spectrum as

$$\begin{aligned}(2\pi)^3 P_F(k)\delta^3(\vec{k}+\vec{k'}) =& \langle\delta_F(\vec{k}), \delta_F(\vec{k'})\rangle \\ =& \int \mathrm{d}^3k (b_{F\delta}^2\delta(\vec{k})\delta(\vec{k'}) + \\ & b_{F\delta}b_{F\eta}(\delta(\vec{k})\eta(\vec{k'}) + \eta(\vec{k})\delta(\vec{k'})) + b_{F\eta}^2\eta(\vec{k})\eta(\vec{k'}))\end{aligned}$$

At linear order the velocity gradient is proportional to the density contrast via $\eta = f\mu^2\delta$, where the $\mu^2 = \frac{k_\parallel}{k}$ factor arises from only taking the contribution along the line of sight $k_\parallel$. In this case the above expression can be rewritten as

$$\begin{aligned}(2\pi)^3 P_F(k)\delta^3(\vec{k}+\vec{k'}) &= b_{f\delta}^2 \int \mathrm{d}^3k \left\{\delta(\vec{k})\delta(\vec{k'})(1 + 2\frac{b_{F\eta}}{b_{F\delta}}f\mu^2 + \frac{b_{F\eta}^2}{b_{F\delta}^2}f^2\mu^4)\right\} \\ &= b_{f\delta}^2(1 + \frac{b_{F\eta}}{b_{F\delta}}f\mu^2)^2(2\pi)^3 P_{\delta\delta}(k)\delta^3(\vec{k}+\vec{k'}).\end{aligned}$$

Introducing the parameter $\beta = \frac{b_{F\eta}}{b_{F\delta}} f$, we succeeded in expressing the flux power spectrum in terms of the linear matter power spectrum

$$P_F(k) = b_{f\delta}^2 (1 + \beta\mu^2)^2 P_{lin}(k). \tag{3.5}$$

At non-linear order, η actually depends on the velocity divergence $\theta = \frac{1}{aHf}\nabla\vec{v}$ via $\eta = f\mu^2\theta$. Using this relationship we arrive at the similar result

$$P_F(k) = b_{f\delta}^2 \left(P_{\delta\delta}(k) + 2\beta\mu^2 P_{\delta\theta}(k) + \beta^2\mu^4 P_{\theta\theta}(k) \right) \tag{3.6}$$

with the additional dependence on the velocity divergence power spectrum $P_{\theta\theta}$ as well as the cross-correlation spectrum $P_{\delta\theta}$.
The parameter β can be estimated with the Zel'dovich approximation [58], where it only depends on the adiabatic index γ that in turn is related to the reionization history [59]. Since we don't want to impose lots of parameters regarding the IGM, we rather model it with two parameters α_{bias} and β_{bias} determined by fitting to the data and allow a redshift dependence with $\beta(z) = \alpha_{bias}(\frac{a(z_{pivot})}{a(z)})^{\beta_{bias}}$. Our pivot redshift is here $z_{pivot} = 3.0$. This treatment allows for lots of freedom to model the IGM suitably without making restrictive assumptions.

There are also a few other physical effects we need to account for.
First of all, the collapse of baryonic matter is not only determined by gravitational forces but is also tied to their innate pressure. Unlike for dark matter, a collapse cannot happen below the Jeans scale $k_J = \frac{aH}{c_s}$, which is related to the sound velocity $c_s = \frac{\gamma T}{\mu_p m_p}$ with temperature T, adiabatic index γ and the mean particle mass μ_p of the IGM. More precisely, we have to look at the filtering scale k_F which is the redshift space average of the Jeans scale k_J [60]:

$$k_F = \frac{1}{D(t)} \int_0^t \mathrm{d}t' \frac{a^2(t')}{k_J^2(t')} \left[\frac{\mathrm{d}}{\mathrm{d}t'} \left(a^2(t') \frac{\mathrm{d}}{\mathrm{d}t'} D(t') \right) \right] \int_{t'}^t \frac{\mathrm{d}t''}{a^2(t'')}. \tag{3.7}$$

For larger k than this scale, a suppression is modeled by an exponential factor $\exp\left(-\left(\frac{k}{k_F}\right)^2 \right)$. Following [54], we fix it in our analysis to $k_F = 18\text{h/Mp}$ but we also check that our results don't really depend on its exact value later on.
Secondly, the IGM is not cold and the spectral lines are therefore subjected to thermal broadening. This broadening is also amplified by other effects like redshift distortions due to peculiar velocities as well as finite resolutions of measurements [57, 61]. To account for this, we include an overall exponential suppression factor of $\exp\left(-\left(\frac{k_\parallel}{k_s}\right)^2 \right)$ with the suppression scale k_s being mainly determined by the thermal broadening, so $k_s \approx \sqrt{\frac{m_p}{T}}$. With an approximated temperature for the IGM of $T \approx 10^4$K, we can derive $k_s \approx 0.11\,\mathrm{s\,km}^{-1}$ and fix this value accordingly like in [54]. Again, we perform a short study later on, to confirm that our results aren't sensitive to this parameter.
The last additional effect we need to account for, are absorption features imprinted by other transitions than Lyman-α on the measured spectrum. The most dominant effect stems from the SiIII absorption, that causes a factor of oscillatory nature with wavelength $\Delta V = 2\pi/0.0028$ due to interference effects

[52]. These effects are well studied by simulation data and as a result, it can be described by

$$\kappa_{\mathrm{SiIII}} = 1 + 2\left(\frac{f_{\mathrm{SiIII}}}{1-\overline{F}}\right)\cos\bigl(\Delta V k_{\parallel}\bigr) + \left(\frac{f_{\mathrm{SiIII}}}{1-\overline{F}}\right)^2, \tag{3.8}$$

where we also include the oscillation strength $f_{\mathrm{Si111}} = 10^{-6}$. The underlying transmission function can be modeled by $\log\bigl(\bar{F}\bigr)(z) = -0.0025(1+z)^{3.7}$ [54, 52]. This description was found to be sufficient and, again, doesn't produce relevant fit implications [54, 57].
To finally arrive at the one-dimensional spectrum, we now need to integrate along the two k-directions k_2, k_3 that are not along the line of sight $k_{\parallel}$:

$$\begin{aligned} P_{F,1D}(k_{\parallel}, z) &= \frac{1}{(2\pi)^2}\int \mathrm{d}k_2 \mathrm{d}k_3 P_F(k,z) \\ &= \frac{1}{(2\pi)^2}\int_0^{2\pi}\mathrm{d}\varphi \int_0^{\infty} m\mathrm{d}m P_F(\sqrt{k_{\parallel}+m^2}, z) \\ &= \frac{1}{2\pi}\int_{k_{\parallel}}^{\infty} k\mathrm{d}k P_F(k,z) \end{aligned} \tag{3.9}$$

This can be applied to each of the power spectra in 3.5 or 3.6 which leads in turn to the three integrals

$$I_0(k_{\parallel}, z) = \int_{k_{\parallel}} \mathrm{d}k k \exp\left(-\left(\frac{k}{k_F}\right)^2\right) P_{\delta\delta}(k,z), \tag{3.10}$$

$$I_2(k_{\parallel}, z) = \int_{k_{\parallel}} \mathrm{d}k \frac{k_{\parallel}^2}{k} \exp\left(-\left(\frac{k}{k_F}\right)^2\right) P_{\delta\theta}(k,z) \quad \text{and} \tag{3.11}$$

$$I_4(k_{\parallel}, z) = \int_{k_{\parallel}} \mathrm{d}k \frac{k_{\parallel}^4}{k^3} \exp\left(-\left(\frac{k}{k_F}\right)^2\right) P_{\theta\theta}(k,z). \tag{3.12}$$

In the linear case, all power spectra are replaced by the linear spectrum. We observe, that the powers of k are changing with the powers of $\mu \propto k^{-0.5}$ and we also have already included the Jeans suppression that also depends on k.
As one can see, the integrals are theoretically uncapped which would leave us to solve integrals in extremely non-linear scales. For I_2 and I_4 these scales aren't really contributing much after a certain point since the k-dependency leads to smaller and smaller corrections. For I_0 however, it takes longer until the filtering scale can suppress the integrand enough and hence we have a contribution from UV-scales. To account for this problem, we solve all integrals up to a cutoff scale and include an extra counterterm I_{ct} for I_0, which captures these problematic scales, like done in [57, 54]. Again, we allow a redshift dependence with $I_{ct} = \alpha_{ct}\left(\frac{a(z)}{a(z_{pivot})}\right)^{\beta_{ct}}$ and add thus two new free parameters.
Lastly, we add an overall amplitude A in which part of $b_{F\delta}^2$ can be absorbed so we are only left with the $\log^2(\overline{F}(z))$ and the thermal broadening as remaining factors. For the background transmission, we use the ansatz $\log\bigl(\overline{F}\bigr)(z) = \alpha_F\left(\frac{a(z_{pivot})}{a(z)}\right)^{\beta_F}$. The transmission amplitude α_F can then also be absorbed

into the overall amplitude A. Finally, with all the additional factors and the integrals, we arrive at the final model

$$\begin{aligned} P_{F,1D}(k_{\|}, z) =& A\kappa_{\mathrm{SiIII}}(k_{\|}, z)\log^2(\overline{F}(z))\exp\left(-(\frac{k_{\|}}{k_s(z)})^2\right) \\ & (I_0 + I_{ct} + 2\beta(z)I_2 + \beta(z)^2 I_4). \end{aligned} \tag{3.13}$$

This relation allows for the overall six free parameters

$$\{A, \beta_F, \alpha_{bias}, \beta_{bias}, \alpha_{ct}, \beta_{ct}\}\,. \tag{3.14}$$

The IGM properties are then determined by mainly the bias parameters (shortened now to α_b and β_b), while the non-linearities we can't sufficiently describe, are captured by our counterterm parameters. The only other more general parameters A and β_F then complete the picture. The advantage of this model is, that we don't need to determine the complex IGM physics beforehand but can leave them open which will thus lead to robust results. However, this means that the model is per design more conservative.

3.3 The 1-loop Power Spectrum

To apply the model we have derived, we need the $\delta\delta$, $\delta\theta$ and $\theta\theta$ 1-loop auto or cross-correlation spectra. For our studied cosmology models, we can always generate the linear spectrum and thus need some kind of formalism to derive the higher order corrections from there. We make use of cosmological perturbation theory which is a commonly used approach to describe ΛCDM and beyond ΛCDM models. Here, we give a short summary of the formalism as described in more detail in [62, 63, 64, 65, 66]. All formulas can basically be found in each of these sources.

The overall goal is to get an expression for the power spectrum in a perturbative expansion incorporating coupling between different modes. For this, we have to start at a general gravitational instability. With an assumption of an irrotational velocity field, the only relevant quantities are the density contrast δ and the peculiar velocity divergence θ. They are subjected to their respective equations of motion in Fourier space corresponding to the continuity and Euler equation

$$\begin{aligned} &\frac{\partial\delta(\vec{k},\tau)}{\partial\tau} + \theta(\vec{k},\tau) = \\ &\qquad = -\int \mathrm{d}^3k_1\mathrm{d}^3k_2\delta_D(\vec{k}-\vec{k_1}-\vec{k_2})\alpha(\vec{k_1},\vec{k_2})\theta(\vec{k_1},\tau)\delta(\vec{k_2},\tau) \quad \text{and} \\ &\frac{\partial\theta(\vec{k},\tau)}{\partial\tau} + \mathcal{H}(\tau)\theta(\vec{k},\tau) + \frac{3}{2}\Omega_m(\tau)\mathcal{H}^2(\tau)\delta(\vec{k},\tau) = \\ &\qquad = -\int \mathrm{d}^3k_1\mathrm{d}^3k_2\delta_D(\vec{k}-\vec{k_1}-\vec{k_2})\beta(\vec{k_1},\vec{k_2})\theta(\vec{k_1},\tau)\delta(\vec{k_2},\tau) \end{aligned} \tag{3.15}$$

with the conformal time τ and conformal Hubble rate $\mathcal{H}$. The factors $\alpha(\vec{k_1},\vec{k_2})$ and $\beta(\vec{k_1},\vec{k_2})$ induce a coupling between different k modes which is a solely non-linear effect. To solve these equations, we make use of the perturbative expansions

$$\delta(\vec{k},\tau) = \sum_{n=1}^{\infty} a^n(\tau)\delta_n(k) \quad \text{and}$$
$$\theta(\vec{k},\tau) = -\mathcal{H}(\tau)\sum_{n=1}^{\infty} a^n(\tau)\theta_n(k). \tag{3.16}$$

This is only valid for Einstein-de-Sitter standard perturbation theory (EdS-SPT) with $\Omega_m = 1$ and $\Omega_\Lambda = 0$. This simpler case has the advantage of leading to a factorization in time with $a(\tau)$ representing the linear growth factor D. Only the fastest growing modes are considered, meaning modes proportional to D. Less fast growing or even decaying modes which can occur due to scattering are subdominant and can be neglected.
Now, the equations of motion can be solved and lead to

$$\delta_n(\vec{k}) = \int \mathrm{d}^3\vec{q_1}... \int \mathrm{d}^3\vec{q_n}\delta_D(\vec{k} - \vec{q_{1...n}})F_n(q_1, \vec{...}, q_n)...\delta_0(\vec{q_n}) \quad \text{and}$$
$$\theta_n(\vec{k}) = \int \mathrm{d}^3\vec{q_1}... \int \mathrm{d}^3\vec{q_n}\delta_D(\vec{k} - \vec{q_{1...n}})G_n(q_1, \vec{...}, q_n)...\delta_0(\vec{q_n}). \tag{3.17}$$

The recursive functions F_n and G_n are constructed with the coupling functions and also depend on each other. The detailed formula isn't really needed to understand the concept so we omit it here, but it can be looked up in e.g. [66, 64]. The initial fluctuations fulfill $\delta_0(\vec{k}) = \delta_1(\vec{k}) = \theta_1(\vec{k})$. For an even compacter expression we can introduce the tuple $(\delta, -\theta/\mathcal{H})$. In this case, the coupling functions are replaced by $\gamma(\vec{k}, \vec{k_1}, \vec{k_2})$ and we are left to solve

$$\frac{\partial\psi(\vec{k},\eta)}{\partial\eta} + \Omega_{ab}\psi_b(\vec{k},\eta) =$$
$$= -\int \mathrm{d}^3k_1\mathrm{d}^3k_2\delta_D(\vec{k} - \vec{k_1} - \vec{k_2})\gamma(\vec{k}, \vec{k_1}, \vec{k_2})\psi_b(\vec{k_1},\eta)\psi_c(\vec{k_2},\eta) \tag{3.18}$$

where we have switched to the time coordinate $\eta = \ln(a(\tau))$ and
$\Omega_{ab} = ((0, -1), (-3/2, 1/2))$ in the case of EdS-SPT. In a general universe, this matrix would be time-dependent and the time-factorization would not be a given anymore. With a series expansion of ψ, the solution now takes the similar form

$$\psi_a(\vec{k},\eta) = \sum_{n=1}^{\infty} \int \mathrm{d}^3\vec{q_1}... \int \mathrm{d}^3\vec{q_n}\delta_D(\vec{k} - \vec{q}_{1...n})\mathcal{F}_a^{(n)}(\vec{q_1}, ..., \vec{q_n}, \eta)\delta_0(\vec{q_1})...\delta_0(\vec{q_n}), \tag{3.19}$$

where the initial fluctuations δ_0 can be assumed to be a Gaussian random field determining our initial linear power spectrum P_0. $\mathcal{F}^{(n)}$ is again recursively defined and contains the time propagation and the interaction term. For EdS-SPT, $\mathcal{F}^{(n)} = a^n(F_n, G_n)$, and a factorized time dependence holds. This principle can be well represented with "Feynman diagrams" which help greatly in visualizing the concept. In Figure 3.3 the series expansion of ψ can be seen. On the left is the linear spectrum ψ^1 which is simply the primordial spectrum propagated in time. Next to it is the next higher order ψ^2, where two modes couple with each other via γ and are then again propagated in time. For the third diagram on the right, two modes couple first with each other and then to a new k mode to produce ψ^3. The higher the order, the more couplings are considered.

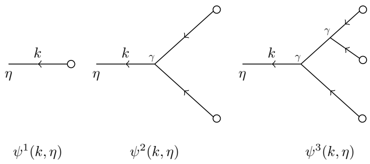

Figure 3.3: Diagrams for the first orders of the $\psi(\vec{k},\eta)$ expansion.

We are interested in the auto- or cross-correlations $\langle \psi_a(\vec{k},\eta), \psi_b(\vec{k'},\eta)\rangle = \delta_D(\vec{k}+\vec{k'})P_{ab}(k,\eta)$. Using this with expression 3.19, we arrive at the series for the power spectrum [64]

$$
\begin{aligned}
P_{ab}(k,\eta) =& P_{ab}^{lin}(k,\eta) + P_{ab}^{1loop}(k,\eta) + P_{ab}^{2loop}(k,\eta) + ... \\
& \text{with} \\
P_{ab}^{lin}(k,\eta) =& F_a^{(1)}(k,\eta)P_0(k)F_b^{(1)}(k,\eta), \\
P_{ab}^{1loop}(k,\eta) =& \int \mathrm{d}^3\vec{q}P_0(q)[3F_a^{(1)}(k,\eta)P_0(k)F_b^{(3)}(\vec{k},\vec{q},-\vec{q},\eta)+ \\
& 3F_a^{(3)}(\vec{k},\vec{q},-\vec{q},\eta)P_0(k)F_b^{(1)}(k,\eta)+ \\
& 2F_a^{(2)}(\vec{k}-\vec{q},\vec{q},\eta)P_0\left(\left|\vec{k}-\vec{q}\right|\right)F_b^{(2)}(\vec{k}-\vec{q},\vec{q},\eta)].
\end{aligned} \tag{3.20}
$$

where Wick's theorem lets us write the higher order correlations as a sum of the different pairings.
The new diagrams we are getting from this expression, are simply the old ones glued together since we are looking at the correlation of two ψ. The linear and 1-loop diagrams can be seen in Picture 3.4. For P_0 on the left, two ψ^1 diagrams are glued together at their initial spectra (represented by the cross) giving us something quadratic. For the three possible P_1 diagrams we have either the pair ψ^2 and ψ^2 or one of the two ψ^1 and ψ^3 pairs giving us something quartic. The same concept would be applied to higher orders resulting in more and more contributing diagrams.

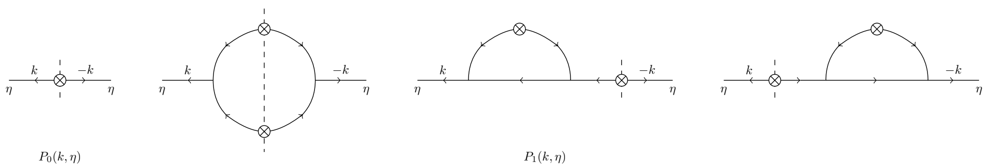

Figure 3.4: Linear and 1-loop diagrams for $P_{ab}(k,\eta)$.

With this formalism, we have finally arrived at our goal of getting a method able to compute higher order spectra. The not so simple implementation of this concept is luckily already done and we can use existing code in this work [65, 64].
In principle, this approach can be used to consider higher orders than the 1-loop corrections as well. Of course, this would make the treatment of non-linearities

even more accurate, however, the main difference towards the linear spectrum should still be captured which we will also see later on. With our additional counterterm treatment of the smaller scales, we thus should be able to describe the non-linearities sufficiently.

4 | ΛCDM Model

4.1 Power Spectra

At first, we want to test our fit with a standard ΛCDM Model. To generate the linear power spectrum we made use of the freely available CLASS (Cosmic Linear Anisotropy Solving System) [67, 68] which is a Boltzmann code computing the evolution of linear perturbations and large scale structure observables in our universe. To match the BOSS data, we need the spectrum for redshifts $z = 3.0, 3.2, ..., 4.2$. Our cosmological parameters are fixed according to the 2018 Planck data [3] which are listed in Table 4.1. Ω_Λ is left free and determined by fulfilling the Friedmann equation. Apart from these typical parameters, we also choose massless neutrinos.

h	0.6781
ω_b	0.0224
ω_{cdm}	0.1201
$\log(10^{10} A_s)$	3.0448
n_s	0.9666

Table 4.1: Cosmological parameters used in generating the ΛCDM spectra.

The computation of the 1-loop spectra is based on the scheme explained in 3.3. With the linear spectrum as input, we can use the code described in [64] and [65] to determine the $\delta\delta$, $\delta\theta$ and $\theta\theta$ corrections.
The resulting linear matter power spectrum as well as $P_{\delta\delta}$, $P_{\delta\theta}$ and $P_{\theta\theta}$ are plotted in Figure 4.1. The top plot shows the absolute spectra, the bottom one the relative spectra for the respective linear spectrum. In general, since we are including higher order contributions to the power spectrum, the 1-loop spectra all cause a correction upwards for mid to high k-values. These corrections are already starting in the pink region which marks the k-values encompassed by the BOSS data, and are at around 100% for the lowest redshift. Therefore, they are pretty significant and should definitely be considered in our model. For higher redshifts, these deviations are smaller since there was less time to build the small scale structure.

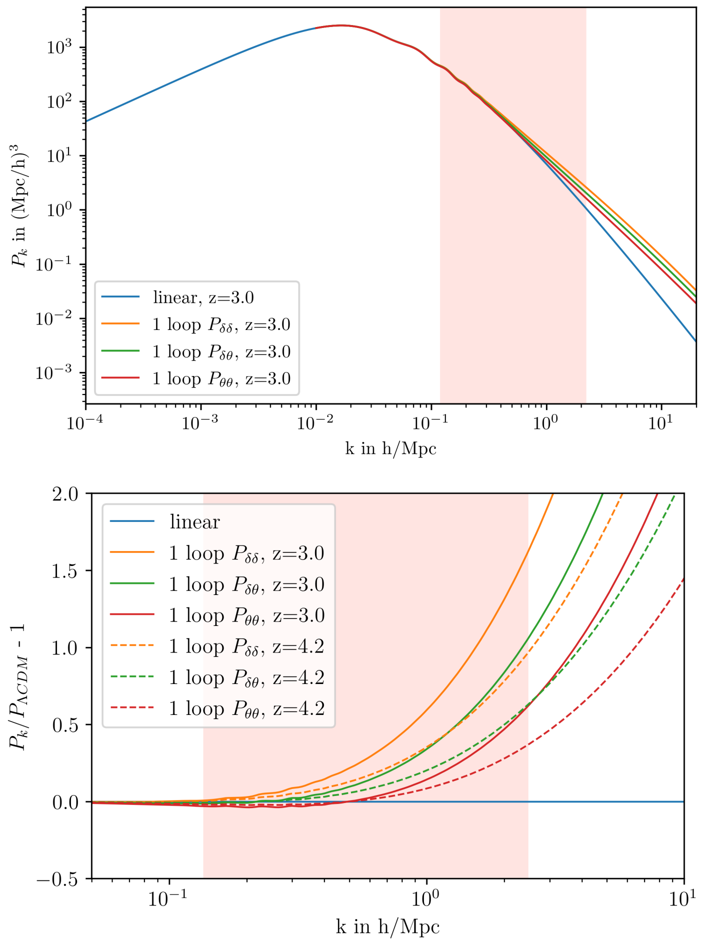

Figure 4.1: The linear and 1-loop power spectra $P_{\delta\delta}$, $P_{\delta\theta}$ and $P_{\theta\theta}$ for a ΛCDM model at $z = 3.0$ at the top and normalized to the linear spectrum and zoomed in towards the relevant scales at the bottom. The pink region highlights the range of k-values that are contained in the BOSS data. In the 1-loop case, there are upwards corrections in this region starting at around $k = 0.2$h/Mpc. This effect is the most dominant for $P_{\delta\delta}$.

4.2 Integrals

With the generated power spectra, we can now compute the integrals which is the only way the different linear and 1-loop models enter the fit. In Figure 4.2 all integrals in the 1-loop (solid line) and linear (dashed line) case are plotted for all redshifts.
The overall shape of the integrals and their differences are determined by an interplay of a few factors:
At first, our integration range decreases for higher $k_{\|}$ which causes also a decrease in the integral.

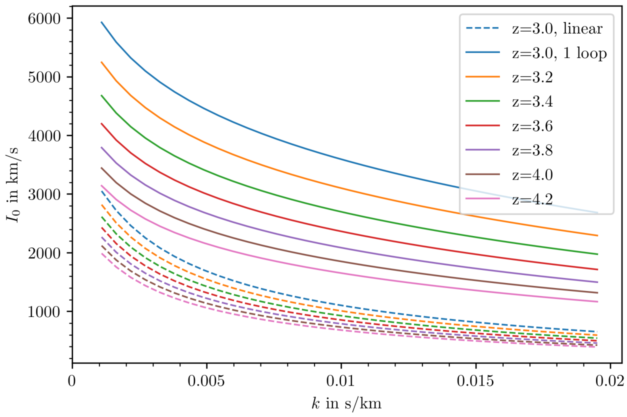

(a) I_0 for all redshifts with a cutoff of 20h/Mpc.

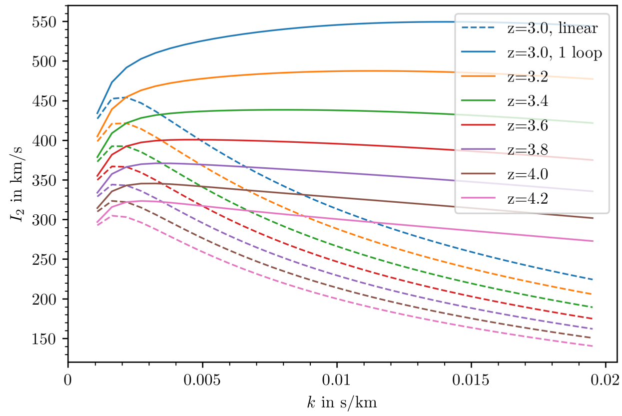

(b) I_2 for all redshifts with a cutoff of 20h/Mpc.

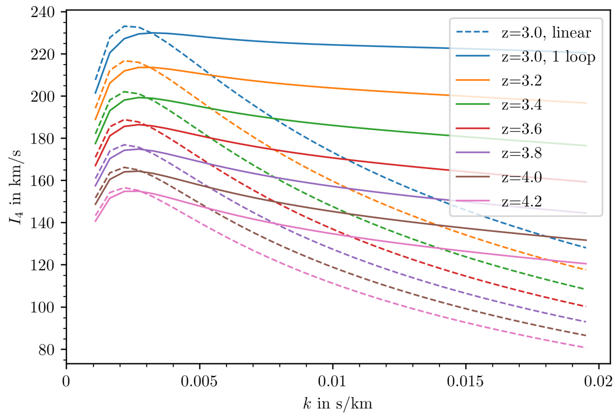

(c) I_4 for all redshifts with a cutoff of 20h/Mpc.

Figure 4.2: The integrals I_0, I_2 and I_4 for our ΛCDM model and redshifts $z = 3.0$ to $z = 4.2$. The dashed lines refer to the linear integrals and are generally smaller compared to the 1-loop case, especially for small scales. The used cutoff scale is 20h/Mpc.

Secondly, there are different powers of k in the integrals namely k, k^{-1} and k^{-3} which lead to a stronger suppression for higher integrals in the latter cases. Additionally, we have also different powers of $k_\parallel$ namely $k_\parallel^0$, $k_\parallel^2$ and $k_\parallel^4$. This makes it possible for the integral to actually increase despite the suppression factors like in the case of I_2. At last, the input spectra have of course an effect which is solely responsible for the difference in shape between linear and 1-loop integrals. The increase in the 1-loop case for small scales, ensures that its integrals are also larger than the linear ones and have a different scale dependency.
To investigate the validity of our cutoff approach, we tested the dependency of the integrals - as well as the fits later on - on their cutoff scale. Due to the exponential suppression factor the integrands itself will converge to 0 for high k. For I_2 and I_4, this suppression is even stronger because of the additional k^{-1} and k^{-3} factor. Therefore, the only question left is which cutoff scale is sufficient. Like in [54] and [57] we choose to make the cut at 20h/Mpc.
In Figure 4.3 the integrals with a cutoff of 10h/Mpc are shown normalized to the respective ones with a cutoff scale of 20h/Mpc. The deviations for I_0 are visibly the largest which is expected since I_0 is the most sensitive to smaller scales. However, due to our introduced counterterm that absorbs the effect of these scales, this should not be a problem. For the higher integrals, the deviations are $\lesssim 2\%$ and also not worrying. In general, one can also see a larger dependency for the 1-loop case due to their larger spectra.

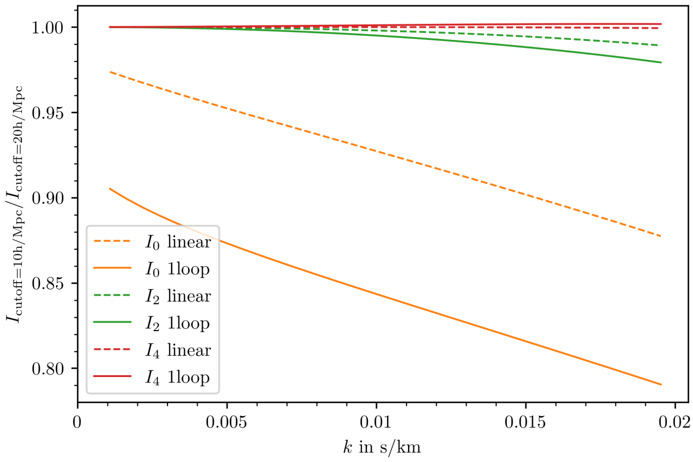

Figure 4.3: The linear and 1-loop I_0, I_2 and I_4 integrals with a cutoff of 10 h/Mpc normalized to their respective integrals with a cutoff of 20 h/Mpc. The deviations are only large for I_0 which is balanced by our introduced counterterm.

4.3 Fits

To compute the fits we used Mathematica. After the integrals were calculated, the difference of the fitting model to the BOSS data points squared divided by the error squared was minimized. This minimized quantity represents our χ^2 helping us to compare and value our fits. All seven redshifts are hereby fitted at the same time, so with 35 k values per redshift bin there are $7 \cdot 35 = 245$

fitting points.
To make sure Mathematica does not get stuck in local minima, the minimization was done scanning different parameter range combinations. Additionally, we added a factor of 100 to the counterterm as well as an overall factor of 1/100 to ensure that A and α_{ct} are at the order of $\mathcal{O}(1)$ avoiding possible precision issues with small or large numbers in the computation. Furthermore, the fits were often repeated with a different cutoff scale which not only tests the cutoff dependence but is also an extra check for possible minimization errors. Together, these measures should reassure that the computation results can be trusted.

4.3.1 Original Fit

The results of the fit in its original form is plotted in Figure 4.4. At the top, the dimensionless spectrum is plotted for each redshift as well as the corresponding BOSS data points with their error bars whereas the bottom shows the spectrum in km/s. The linear fit is indicated with the dashed line and the 1-loop fit with the solid one. In both cases our model seems to capture the shape of the data quite good with the 1-loop case fitting visibly better to mainly the small scales as expected. This is reflected by the χ^2 values of 206.12 and 193.74 listed with the other parameters in table 4.2. Overall, we have an improvement of $\Delta\chi^2 = 12.4$. It is difficult to consistently interpret the other parameters but we can make a few observations.
The overall amplitude is significantly smaller in the 1-loop case, which is not surprising regarding the larger spectra. The redshift-dependence for the average transmission is stronger in the 1-loop case whereas it is weaker for the β parameter that also undergoes a switch in signs. The counterterm shows in both cases a very strong redshift dependence and while generally negative, it is approximately twice as large for the 1-loop case.
These parameters all not only capture the effects of the complex intergalactic medium but also of the non-linear scales. While we already consider non-linear corrections, these are still at first order and are not sufficient in the extremely small scales influencing I_0. Overall, the parameters for this baseline model while complex can still be used to make comparisons to the other tested models later on.

	linear	1-loop
χ^2	206.12	193.74
$100A$	1.27	0.94
β_f	1.72	2.60
α_b	0.80	-3.22
β_b	3.91	1.48
$\alpha_{ct}/100$	-0.85	-1.77
β_{ct}	47.70	35.95

Table 4.2: ΛCDM original fit results for the linear and 1-loop case.

Like explained in section 3.2, we have fixed the two parameters $k_s = 0.11$s/km and $k_f = 18$h/Mpc. Since the IGM is a complex topic, we explicitly checked that the fit is not very sensitive to these two parameters and the complex nature can actually be sufficiently captured by our remaining free parameters. In Figure 4.5 we plot the linear χ^2 value for a range of k_s and k_f values normalized to the χ^2 of the actual chosen values. In both cases the deviations are at the most 1%. Additionally, the fixed values also lie in a minimum and represent the best fit. Therefore, the choice of the two parameters seems to be good and not overly important.

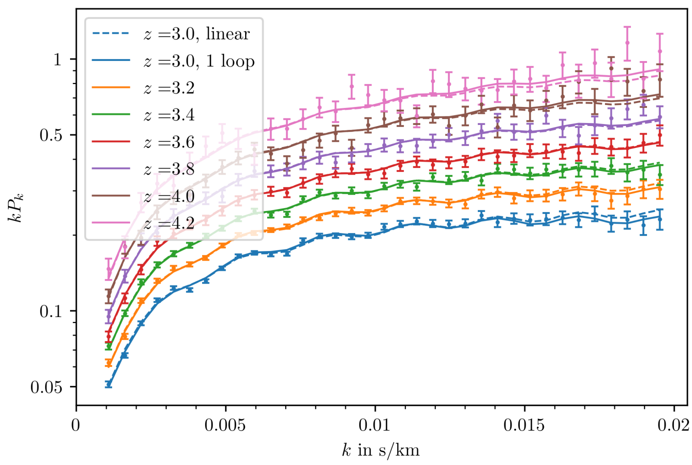

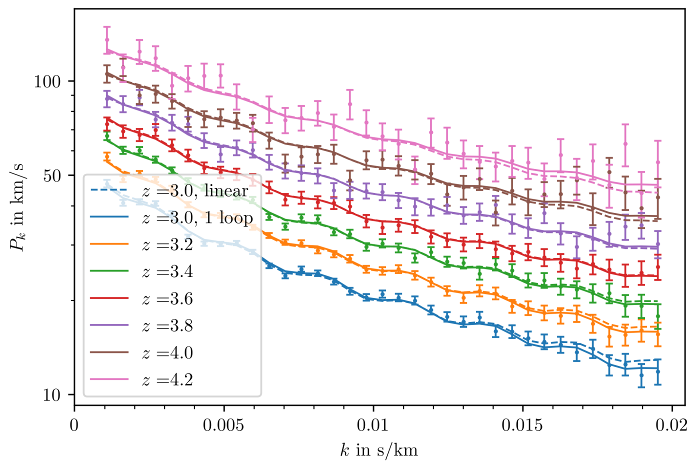

Figure 4.4: The linear (dashed) and 1-loop (solid) fit for all redshifts $z = 3.0-4.2$ to the BOSS data with its errorbars.

4.3.2 Fits with β_b and β_{ct} Restrictions

The β_x parameters all describe a certain z-dependency we modeled with a polynomial law which is only physically plausible for small variations across the redshifts. Whereas β_f is always at a suitable value, this isn't always true for the two other ones. β_{ct} is already extremely large in the original ΛCDM fit and β_b displays jumps to high values from time to time - at least for the later tested models. Therefore, it makes sense to restrict them with a prior ranging from

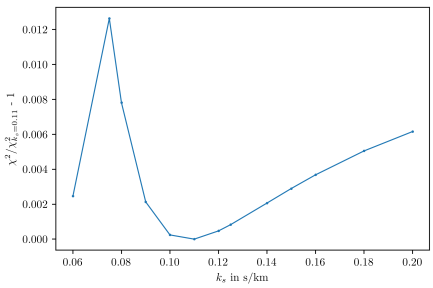

(a) Dependency of fit on the value of k_s given in s/km. The chosen value of 0.11 s/km is the minimum.

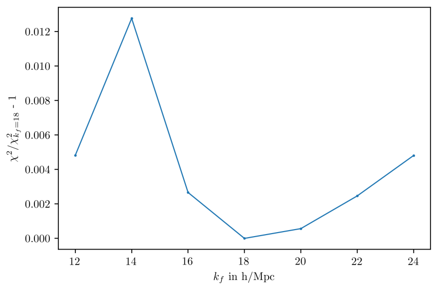

(b) Dependency of fit on the value of k_f given in h/Mpc. The chosen value of 18 h/Mpc is the minimum.

Figure 4.5: χ^2 for different values of k_s and k_f normalized to the χ^2 with the chosen values. The chosen values produce in both cases the best fit with deviations around or under 1%.

-10 to 10. While still allowing for a generous range of parameters, this prior filters the really high and all together quite unphysical values of β_b and β_{ct}.
The result of this fit with the restrictions $-10 \leq \beta_b \leq 10$ and $-10 \leq \beta_{ct} \leq 10$ can be seen on the right in table 4.3. Since β_{ct} was larger before, it is now fitted to the largest possible value of 10. The other parameters are only slightly varied to before while the fit worsens to 211.11 and 203.77 for linear and 1-loop respectively.
Another restriction we can impose, is to fix the β_b parameter completely. We already mentioned before, that the famous Zel'dovich approximation describing gravitational collapse predicts a β parameter with no z-dependence [59]. In accordance to this, we can also try to describe β by only a constant and hence set $\beta_b = 0$. The result of such a fit is seen on the left in table 4.3. Due to the five instead of six free parameters, the fit worsens of course again with a χ^2 of 223.91 and 243.45 for linear and 1-loop. Notably, the 1-loop fit is now for the first time worse than the linear one and not only slightly. It seems much better to only restrict β_b to reasonable values instead of imposing this strong requirements.

	$\beta_b = 0$		β_b and β_{ct} priors	
	linear	1-loop	linear	1-loop
χ^2	223.91	243.45	211.11	203.77
$100A$	1.23	0.89	1.23	0.92
β_f	2.61	3.17	1.75	2.62
α_b	0.75	-2.94	0.93	-3.55
β_b	0.00	0.00	3.37	1.09
$\alpha_{ct}/100$	0.47	0.89	-1.43	-2.73
β_{ct}	-7.55	-5.65	10.00	10.00

Table 4.3: ΛCDM β_b and $\beta_c t$ restriction fit results for the linear and 1-loop case.

4.3.3 Fits with counterterm Restrictions

Another way to modify our fit further is by altering our counterterm. In principle, this counterterm is proportional to the used spectrum squared. The spectrum itself is in linear order proportional to the scale factor $a = \frac{1}{1+z}$ and in second order proportional to a^2. In return, this would result in a linear counterterm proportional to a^2 and a 1-loop counterterm proportional to a^4. According to this approximation, our first alteration 'CT1' is made up of

$$\begin{aligned} I_{ct1,\text{linear}} &= \alpha_{ct1} \cdot \left(\frac{1+z_{pivot}}{1+z}\right)^2 \\ \text{and} \quad I_{ct1,1-\text{loop}} &= I_{ct1,\text{linear}} + \alpha_{ct1} \cdot \left(\frac{1+z_{pivot}}{1+z}\right)^4, \end{aligned} \tag{4.1}$$

so only α_{ct1} and α_{ct2} are fitted in each case respectively.
For our second alteration 'CT2', we allow for more freedom with a quartic term in the linear and 1-loop case and a completely independent 1-loop counterterm:

$$\begin{aligned} I_{ct2,\text{linear}} &= \alpha_{ct1} \cdot \left(\frac{1+z_{pivot}}{1+z}\right)^2 + \alpha_{ct2} \cdot \left(\frac{1+z_{pivot}}{1+z}\right)^4 \\ I_{ct2,1-\text{loop}} &= \alpha_{ct1} \cdot \left(\frac{1+z_{pivot}}{1+z}\right)^2 + \alpha_{ct2} \cdot \left(\frac{1+z_{pivot}}{1+z}\right)^4 \end{aligned} \tag{4.2}$$

Here, α_{ct1} and α_{ct2} are fitted for each case, so we have 6 instead of 5 free parameters.
The results of these variations are listed in table 4.4. For CT1, the counterterm

	CT1		CT2	
	linear	1-loop	linear	1-loop
χ^2	222.11	212.22	211.38	205.44
$100A$	1.18	0.89	1.25	0.95
β_f	1.95	2.64	1.80	2.70
α_b	1.00	-4.11	0.87	-2.95
β_b	2.99	0.80	3.29	1.14
$\alpha_{ct1}/100$	-1.19	-1.19	4.23	13.17
β_{ct1}	2.00	2.00	2.00	2.00
$\alpha_{ct2}/100$		-4.12	-5.33	-14.23
β_{ct2}		4.00	4.00	4.00

Table 4.4: ΛCDM ct restriction fit results for the linear and 1-loop case.

is always negative with an increase due to the extra term in the 1-loop case. For CT2, the counterterm is also always negative but only due to the larger quartic terms resulting in a more nuanced redshift-dependence. Due to the additional free parameter CT2 gives overall a better χ^2. The fact that the higher order term is larger, hints to a counterterm that doesn't really behave according to such an expansion approach. Therefore, these counterterm alterations are to be taken with a grain of salt. While CT2 provides a similar freedom which results in not too bad χ^2 values, it also behaves not as intended, so this alteration doesn't provide really new perspectives compared to the original fit.

4.3.4 Summary

Here, we give a quick overview over all the ΛCDM fit variations as listed in table 4.5. The original fit leaves all 6 parameters completely free, whereas "β_b prior"

	linear χ^2	1-loop χ^2
original	206.12	193.74
β_b prior	206.12	193.74
β_b and β_{ct} prior	211.11	203.77
$\beta_b = 0$	223.91	243.45
$\beta_b = 0$ and β_{ct} prior	223.91	243.45
CT1	222.11	212.22
CT2	211.38	205.44

Table 4.5: Summary of all the χ^2 values of the different fit variations in the linear and 1-loop case for ΛCDM.

and "β_b and β_{ct} prior" set the additional requirement of $-10 \leq \beta_x \leq 10$ to limit the z-dependency to reasonable values. The "β_b prior" is a bit redundant since its restrictions are already fulfilled by the original fit, but it was included for better comparisons with the following dark matter model.
Leaving 5 parameters free, we have the "$\beta_b = 0$" as well as the "$\beta_b = 0$ and β_{ct} prior" fit where the latter is again redundant and only included for completion. This change was motivated by the Zel'dovich approximation and its prediction for the β parameter. However, they don't seem very helpful for now.
The last two fits each alter the counterterm in a different way. The first one, CT1, fits a quadratic term in the linear case and the same quadratic term plus a fitted quartic term for the 1-loop case - so overall 5 parameters. In the second one, CT2, a quadratic plus quartic term is fitted in the linear and 1-loop case, leaving 6 parameters free again. They also don't seem too useful but are again discussed for WDM.
Overall, the priors seem like the best choice for a fit variation. While the fit worsens of course, it only denies unphysical behavior while not imposing lots of restrictions. With these reference results, we can now turn to the more interesting models of first warm dark matter and then decaying cold dark matter.

5 | Warm Dark Matter Model

5.1 Overview

Before going on towards DCDM, we first want to look at a WDM model. This not only allows us to test our fitting method against a not too complex model, it is also well studied and its effects well understood. Thus, it can help in uncovering possible issues with the method or implementation and can be used to test different fit variations and their impact. Additionally, it already encompasses a feature also appearing in DCDM, namely the suppression caused by WDM. Overall, it therefore serves well as a "test model" and still allows us to derive mass constraints at the end.
The difference between CDM and WDM lies in the free-streaming length which describes the velocity dispersion. CDM has an extremely small free-streaming length, meaning it is massive enough to always be non-relativistic. Warm dark matter, on the other hand, is actually partly relativistic during structure formation which causes it to slow down. This happens for scales smaller than the free-streaming scale k_{fs}, since fluctuations are washed out. The lighter the particle, the larger the free-streaming scale and the earlier clustering is inhibited. This results in a characteristic suppression in the matter power spectrum for $k > k_{fs}$ and is the reason why it is proposed as a possible solution for small-scale problems. One is the cusp-core problem, meaning that the inner mass density of dark matter halos is more cuspy in simulations than it is in observations [18]. The other one is the missing satellites problem, describing the larger amount of low mass halos predicted by N-body simulations than observed [69]. Lots of simulations have been performed on these and both problems can actually be eased by WDM. It can lower core densities and increase the core radii as well as also reduce the number and concentration of low-mass halos [70]. However, while improving these issues, WDM can't eliminate them completely [71, 71, 72, 73, 74]. Numerical simulations are however not only very complex computationally, they are also criticized for not being precise enough. One problematic topic for example, is including baryonic processes and feedback which is challenging to simulate. Increasing computational power will make it possible to implement more of such complexities. We can therefore look forward to more accurate simulations and thus more insight on the impact of DM models on the small-scale structure formation.
There are two popular theories describing WDM particles. One is thermal dark matter that was in thermal equilibrium at some point and decouples as soon as it falls out of equilibrium due to the decreasing temperature. Another, is sterile neutrinos that were never in thermal equilibrium in the first place ([75], [76],

[77]). They are produced by active neutrinos and can be quite heavy due to the seesaw-mechanism. The important property of WDM is hereby the distribution function which can be described as $f = \chi/e^(p/T_x) + 1$ [78, 57]. For $\chi = 1$ and $T_x << T_\nu$, we have the fermionic thermal relic and for $\chi << 1$ and $T_x = T_\nu$ the sterile neutrino. The free-streaming scale depends on the momentum and therefore the distribution function which changes for different models [17]. However, for observables like the power spectrum, only the ratio T_x/m_x is actually important. Thus, the thermal and the sterile masses can actually be related via [79]

$$m_{st} = 4.47keV \left(\frac{m_{th}}{keV}\right)^{\frac{4}{3}} \left(\frac{0.12}{\omega_x}\right)^{\frac{1}{3}}. \tag{5.1}$$

Additionally, the temperature is given by the relation

$$\omega_x = \chi \left(\frac{T_x}{T_\nu}\right)^3 \frac{m_x}{94eV}. \tag{5.2}$$

This allows us to only set one mass and then convert them into each other. In our case, we set sterile masses with a temperature of $T_\nu = \frac{4}{11}^{1/3} T_\gamma$ where t_γ is the photon temperature.

m_{st} in keV	m_{th} in keV	T_{th} in T_ν
0.05	0.034	0.61
0.1	0.058	0.48
0.2	0.097	0.38
0.3	0.132	0.34
0.4	0.164	0.3
0.5	0.193	0.28
0.6	0.222	0.27
0.7	0.249	0.25
0.8	0.275	0.24
0.9	0.301	0.23
1.0	0.325	0.22
1.5	0.441	0.20
2.0	0.547	0.18
2.5	0.647	0.17
3.0	0.741	0.16
3.5	0.832	0.15
4.0	0.92	0.14
4.5	1.005	0.14
5.0	1.008	0.13
5.5	1.168	0.13
10.0	1.829	0.1
15.0	2.479	0.09
20.0	3.076	0.08

Table 5.1: Chosen sterile masses with corresponding thermal masses and temperatures.

5.2 Power Spectra and Integrals

To generate the power spectra, we use again CLASS with the same parameters as in Table 4.1. The cold dark matter is then replaced with non-cold dark matter and its mass is varied. The sterile masses we choose, encompass the range $m_{st} = 0.05 - 20$ keV and the corresponding thermal ones $m_{th} = 0.03 - 3.1$ keV. All masses are listed in Table 5.1 with the additional temperature in the thermal case. We can see nicely, how it decreases for larger masses since the WDM gets gradually less warm and converges towards CDM.

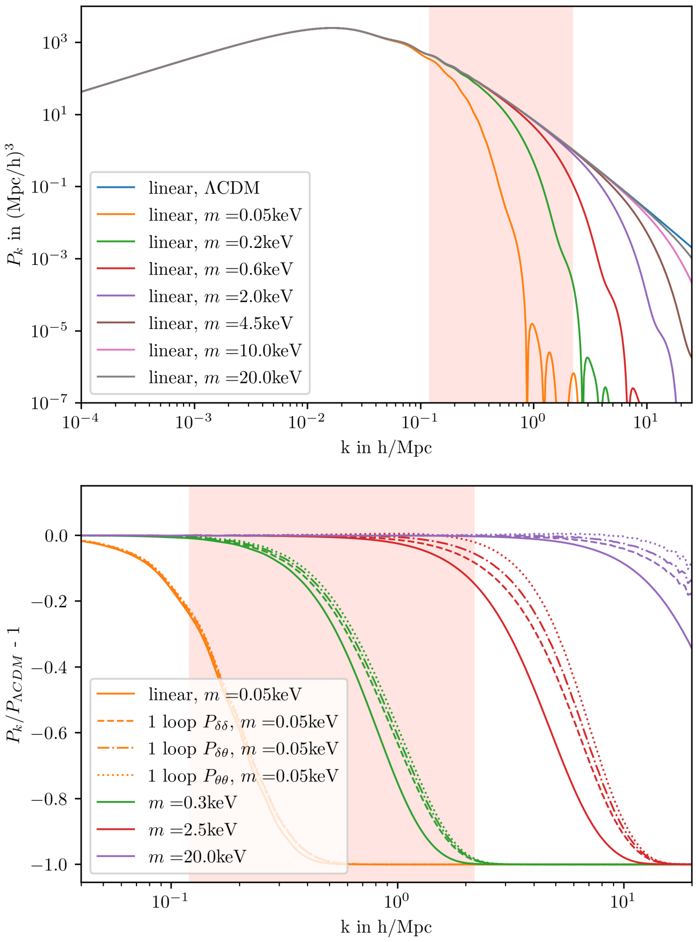

Figure 5.1: The linear and 1-loop power spectra $P_{\delta\delta}$, $P_{\delta\theta}$ and $P_{\theta\theta}$ for a WDM model at $z = 3.0$ at the top and normalized to the linear spectrum and zoomed in towards the relevant scales at the bottom. The pink region highlights the range of k-values that are contained in the BOSS data. The suppression visibly sets in much earlier for lower masses.

The power spectra for a few selected masses are shown in Figure 5.1. At the top, the linear spectra for the whole k range can be seen at $z = 3.0$. At the bottom, we also show the 1-loop corrections $P_{\delta\delta}$, $P_{\delta\theta}$ and $P_{\theta\theta}$, that are always normalized to their respective non-linear ΛCDM spectrum, and zoom in to only the relevant k regimes. Like always, the pink region indicates the BOSS region. For the largest mass of $m = 20$keV, we see in both plots, how the spectrum converges towards ΛCDM. The suppression sets in well after our region of interest and is only slightly present for very small scales. For the non-linear spectra, this suppression is even more lessened. On the other end of the mass range, $m = 0.05$keV has a much smaller free-streaming scale k_{fs}, washing out the matter fluctuations even before the BOSS region where it converges quickly to 0. Due to its features being located at larger k values, its non-linear spectra don't deviate much from the linear one. Starting from $m \sim 0.3$keV, the suppression is now located inside the BOSS region with larger masses shifting the cutoff to smaller and smaller scales. The ΛCDM spectrum is traced until the free-streaming scale is reached and the matter fluctuations drop to basically 0. The 1-loop spectra get more important towards the smaller and more non-linear scales. Interestingly, we also see that spectra including the velocity divergence receive the most corrections compared to ΛCDM. Also, the non-linearities affect the start of the suppression which is now delayed.

Overall we see, that our masses encompass three regimes with the cutoff setting

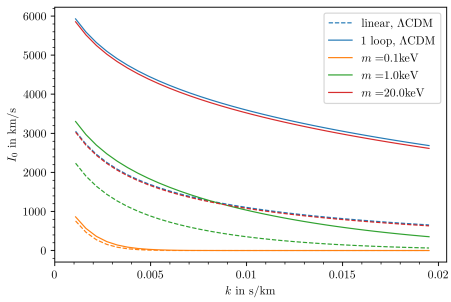

(a) I_0.

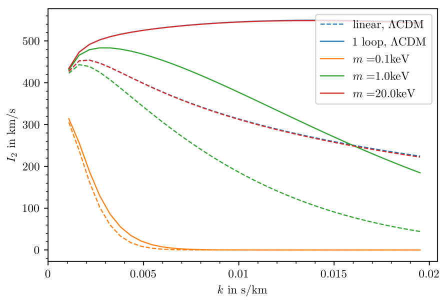

(b) I_2.

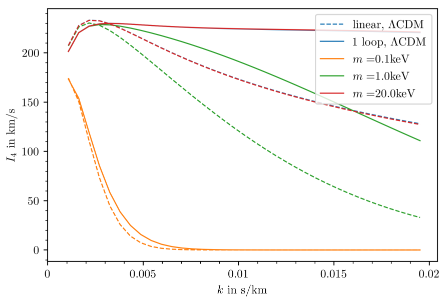

(c) I_4.

Figure 5.2: I_0, I_2 and I_4 for WDM with three different masses $m = 0.1, 1.0, 20.0$keV and a redshift of $z = 3.0$. The ΛCDM model is also plotted for better comparison. The dashed lines refer to the linear integrals, the solid ones to the 1-loop case. The used cutoff scale is 20h/Mpc. The lower the mass, the stronger is the suppression and thus the integral decreases.

in before, during and after the BOSS region.
The same behavior for the masses can also be seen in the computed integrals in 5.2 where they are shown for the linear and 1-case for three different masses. The smallest mass with $m = 0.1$keV quickly converges to 0 as its respective power spectrum. For more intermediate masses, the suppression causes a constant drop in the overall amplitude for I_0. For the higher integrals, the amplitude is affected differently. While ΛCDM is almost constant, the suppression for WDM induces an additional scale-dependency for the linear and the 1-loop case. The largest mass off $m = 20$keV experiences no cutoff in the BOSS regime and therefore perfectly aligns with ΛCDM for I_2 and I_4, and almost perfectly for I_0.
When we look at the cutoff dependency, we observe that the cutoff scale for small masses is almost irrelevant due to them being already 0 beforehand. Only for intermediate and high masses, the integrals aren't that small anymore and the cutoff scale makes a visible difference. Thus, we show the cutoff dependency for the highest mass $m = 20$keV in Figure 5.3. Again, only I_0 is affected much which is absorbed by our counterterm, while I_2 and I_4 experience deviations of $\lesssim 2\%$. Regarding these behaviors, we expect large masses to reproduce ΛCDM results and small masses to cause really high amplitudes to try and lift the integrals. The intermediate values will of course be the more interesting ones. If a slight suppression on small scales is actually supported by our data, the fit should improve for these masses.

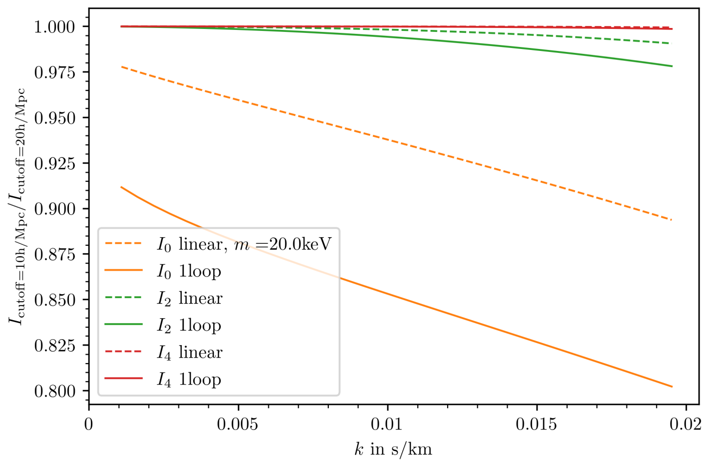

Figure 5.3: The linear and 1-loop I_0, I_2 and I_4 integrals with a cutoff of 10h/Mpc normalized to their respective integrals with a cutoff of 20h/Mpc. The deviations are the largest for high masses, so the plot uses the WDM model with $m = 20$keV. The behavior in this case is the same as for ΛCDM.

5.3 Fits

5.3.1 Original Fit

With these expectations, we can now turn towards our fit results. We always show the linear and 1-loop case, allowing us to observe the non-linear effects, as

well as the exclusion regions. The yellow and green bands show the confidence intervals of 68 and 95%, respectively, around ΛCDM. $\Delta\chi^2$ values in this band agree with our ΛCDM fit, while values above leads to exclusion and values below to a preference. Note, that the reference value for ΛCDM changes depending on the fit with them being summarized in Table 4.5.
In Figure 5.4 the results of the original fit are shown. At the top, the linear $\Delta\chi^2$ values are plotted for the different masses, whereas the bottom shows the 1-loop fits.
In the linear case, the fit actually fulfills our expectations from before. Towards extremely small masses, the χ^2 value diverges together with the amplitude that tries to do everything in its power to counterbalance the too strong suppression. This obviously still produces the wrong shape and is thus strongly excluded. With the shifting of the suppression in the BOSS regime, the fit improves a lot and actually leads to a preference over ΛCDM. The minimum is around $m \sim 2.5$keV which we also showed in the power spectra plots (5.1) and which corresponds to a suppression for $k \gtrsim 1$h/Mpc. This hits apparently the sweet spot for the BOSS data, since an earlier and later suppression worsens the fit. For the high-mass regime, we also reproduce ΛCDM as expected. The black dotted line corresponds to the same fit with an integral cutoff of 10h/Mpc and follows the fit with a cutoff of 20h/Mpc quite nicely. We also confirm, that the deviations become larger for higher masses as explained before. These cutoff checks are however mostly done to probe the minimization process since large deviations in shape would be a reason for concern. Thus, we don't require a complete overlay of the results but only similar behavior. Since this is given here, and the overall results are very reasonable, the implementation of the method seems to work pretty well.
Regarding this validation of our fitting method, we can now turn towards the more complex 1-loop case at the bottom. Here, the linear fit is also plotted with the different ΛCDM reference value to allow for a more direct comparison. The high and low-mass regimes of the fit show a very similar behavior compared to the linear fit, including the compatibility for late suppressions. Additionally, the fit for the small masses is shifted a bit to the left. This can be explained, by the corrections causing the suppression to be a bit delayed, so a similar cutoff scale is achieved by a lower mass. This is also responsible for the earlier deviation from the 10h/Mpc cutoff case compared to ΛCDM. The strongest differences to the linear case, happen however before and are thus confirmed by the other cutoff fit. These differences occur for the intermediate mass range where at first, the fit seems to improve similarly, but then it worsens into the excluded region instead of the preferred one. The minimum in this range is reached at $m \sim 1.5$keV, so slightly before the linear one, as expected. In the sudden rise afterwards, the fit actually produces worse absolute χ^2 values than the linear case, which only happens in this problematic regime. This indicates, that the data is indeed very sensitive to the shape of the suppression which is altered by the non-linearities and causes a stronger k dependence. The higher the mass, the more strongly differs our shape to the linear case as the suppression occurs at smaller scales. For high enough masses this is not a problem, since the shape can't be fully probed by the BOSS data. Instead, more intermediate mass values are affected, where the shape differs already significantly but it can still be probed. That is why, the compatible mass ranges are actually split in two. A very small mass range at the lower end, which doesn't yet include a strongly different shape and

a higher mass range, which can't probe it sufficiently anymore.
Overall, the original fit provides us with the mass constraints

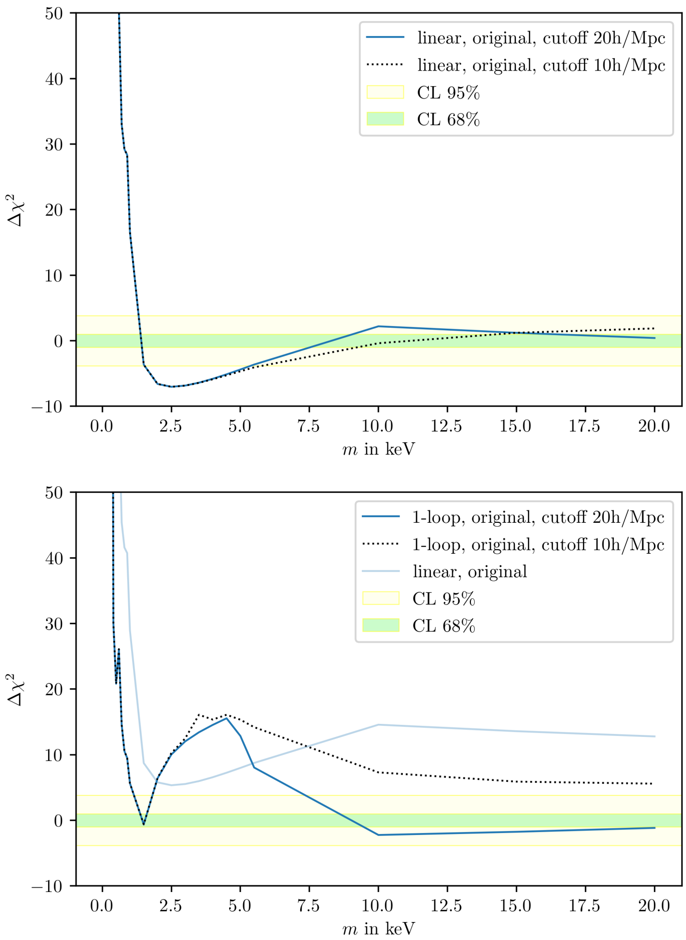

Figure 5.4: The linear (top) and 1-loop (bottom) χ^2 values minus the respective $\chi^2_{\Lambda CDM}$ for the original fit. The fit with a cutoff of 10h/Mpc (black, dotted) is also shown. The green and yellow band shows the region around ΛCDM with a confidence limit of 68% and 95% – meaning $\Delta\chi^2 = 0.989$ and $\Delta\chi^2 = 3.841$ respectively.

$$
\begin{aligned}
\text{linear} \quad & m \geq 1.31\,\text{keV} \\
1\text{−loop} \quad & 1.14\,\text{keV} \leq m \leq 1.82\,\text{keV} \\
& m \geq 7.34\,\text{keV}
\end{aligned}
$$

We see, that the linear case causes weaker constraints but we also know, that this description is ultimately not valid. Thus, our final mass constraints from the original fit, as well as the fits later on, are of course given by the 1-loop case.

5.3.2 β_b and β_{ct} Restrictions

Now, we turn to the fit variations which impair the β_b and β_{ct} parameters that were already explained for ΛCDM.
In Figure 5.5 the results of the β_b prior fit can be seen at the top, and the β_b and β_{ct} fit at the bottom. Linear fits are always located on the left side and 1-loop fits on the right side. Each plots also shows the original fit result to directly see the differences.

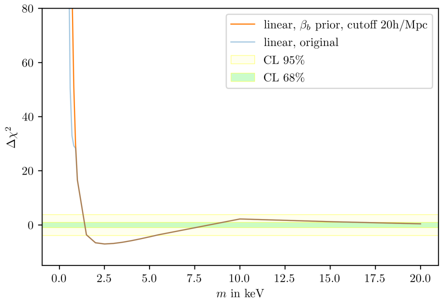

(a) linear, β_b prior

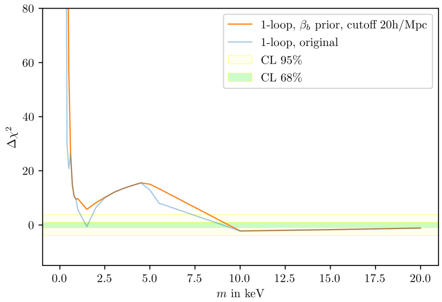

(b) 1-loop, β_b prior

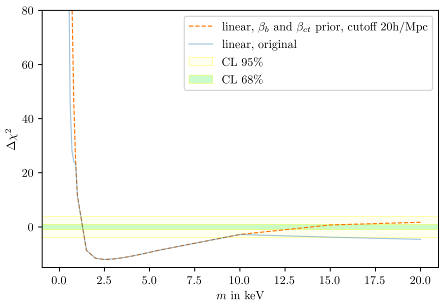

(c) linear, β_b and β_{ct} priors

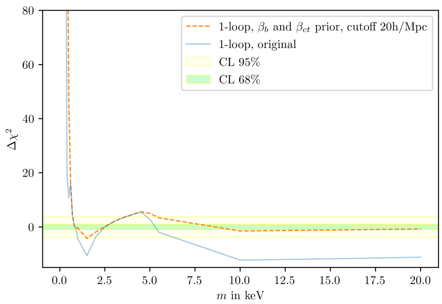

(d) 1-loop, β_b and β_{ct} priors

Figure 5.5: The linear (left) and 1-loop (right) χ^2 values minus the respective $\chi^2_{\Lambda CDM}$ for the β_b prior at the top and the β_b and β_{ct} priors at the bottom.

For the β_b prior fit, we see immediately that the overall behavior doesn't change much for both cases. The linear fit only exhibits small deviations for the low-mass regime, where the fit is excluded anyway. The remaining χ^2 values are reproduced perfectly, validating again our original fit. In the 1-loop case, we also see slight differences for the intermediate mass regimes. The excluded bump shape is much smoother and the first small compatible mass region erased. This suggests, that this compatibility is produced artificially by unphysical high β_b values and is not a result coming from the actual power spectra. Thus, it improves the constraints from the original fit a lot while still not imposing strong assumptions. The derived mass constraints should still be robust while also being more sensitive to the actual underlying physics. This provides us with mass bounds that are similar to before, but exclude one of the compatibility regions for the 1-loop case, tightening the constraints:

$$\begin{aligned} \text{linear} \quad & m \geq 1.31\,\text{keV} \\ 1\text{−loop} \quad & m \geq 8.25\,\text{keV} \end{aligned}$$

Regarding the additional included β_{ct} prior at the bottom, we observe a higher χ^2 for the high-mass regime. The same effect was observed for the ΛCDM case. The fit preferred a very large β_{ct} value, which resulted in a strong worsening of the fit when constraining β_{ct}. Seeing this also occur for the WDM which approaches CDM, shows that we also have that convergence towards ΛCDM in the fit. In itself, these are great news, however, this also imposes a problem. Our derived $\Delta\chi^2$ values are always set in reference to a ΛCDM fit. When this reference value worsens a lot, the resulting constraints can actually be way more lax despite limiting the freedom. In our case, the high and low-mass regimes are then treated somewhat unfairly, especially when considering that they also have differing cutoff dependencies. This is responsible for the large difference in mass bounds to the previous variation, even though they actually include each other. The constraints from an imposed β_b and β_{ct} prior are given by

$$\begin{aligned} \text{linear} \quad & m \geq 1.19\,\text{keV} \\ 1\text{−loop} \quad & 0.72\,\text{keV} \leq m \leq 3.70\,\text{keV} \\ & m \geq 5.36\,\text{keV} \end{aligned}$$

Due to the reference problem, we see such constraints as very robust ones that help in understanding the method and its problems but can't be used to constrain the WDM model sensibly.

Another stronger restriction, is the setting of $\beta_b = 0$ which removes the z-dependency from the bias parameter. The case without and with an additional β_{ct} prior are shown in Figure 5.6 at the top and bottom, respectively. Again, we see the same problem as before. The ΛCDM reference value is strongly worsened and suddenly, almost all masses are not only allowed but also preferred for the linear and 1-loop case. Also similarly, we observe that the absolute χ^2 deviations are increasing going towards higher masses. Regarding the unreasonable result, we can say that $\beta_b = 0$ is simply not a very good description of ΛCDM. This in turn produces mass constraints and preference regions for WDM, that can probably be discarded. Nonetheless, these are the mass constraints from purely $\beta_b = 0$

$$\begin{aligned} \text{linear} \quad & m \geq 0.97\,\text{keV} \\ 1\text{−loop} \quad & 0.39\,\text{keV} \leq m \leq 0.48\,\text{keV} \\ & m \geq 0.52\,\text{keV}, \end{aligned}$$

as well as from an additional β_{ct} prior

$$\begin{aligned} \text{linear} \quad & m \geq 0.97\,\text{keV} \\ 1\text{−loop} \quad & m \geq 0.52\,\text{keV}. \end{aligned}$$

5.3.3 Counterterm Restrictions

In another fit variation, we apply the counterterm restrictions CT1 (see 4.1) and CT2 (see 4.2), resulting in fits shown in 5.7.

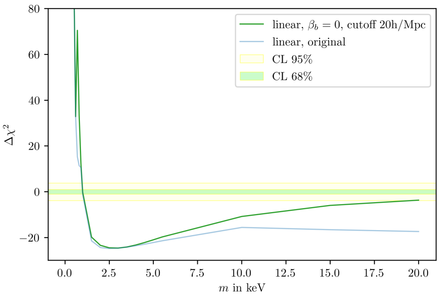

(a) linear, $\beta_b = 0$

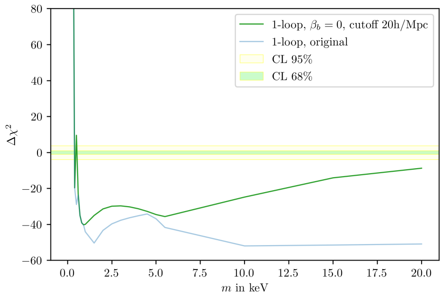

(b) 1-loop, $\beta_b = 0$

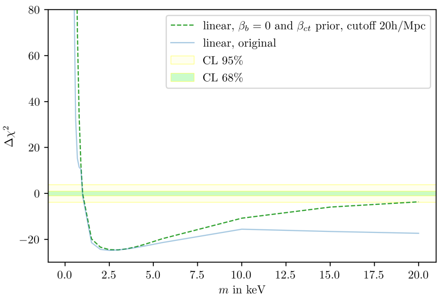

(c) linear, $\beta_b = 0$ and β_{ct} prior

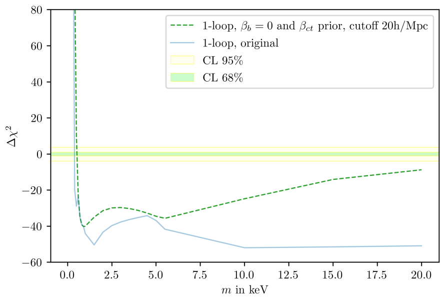

(d) 1-loop, $\beta_b = 0$ and β_{ct} prior

Figure 5.6: The linear (left) and 1-loop (right) χ^2 values minus the respective $\chi^2_{\Lambda CDM}$ for $\beta_b = 0$ at the top and for $\beta_b = 0$ and a β_{ct} prior at the bottom.

For the first one, the linear fit shows a large difference for the first time, as well as the 1-loop case. This happens for both in the intermediate mass regime, which is the most sensitive to non-linearities. For the high mass regime, we at least still reach ΛCDM.
When we look at the completely freely fitted counterterm, it is the largest for the intermediate to small mass regimes while converging towards small values for high masses. Since we already saw that non-linearities play the largest role in this first regime, this is not surprising. The quadratic counterterm which is now fitted for the linear case, exhibits the same behavior (with of course different absolute values) but is a bit larger in the low-mass regime while being reduced much earlier at around 2keV. Thus, we see that these masses are considerably worsened to before. For the 1-loop case, the freely fitted counterterm is usually much larger than the linear one and is slightly shifted to lower masses. When we now use the quadratic counterterm from the linear case, the quartic counterterm doesn't focus on increasing it, but more on getting a similar shape to its freely fitted one. The lower counterterm is obviously not ideal for the intermediate mass regimes which we see in the fit. Still, the quartic counterterm is mostly slightly smaller than the quadratic one, preserving our idea of a counterterm expansion at least somewhat. This makes this fit variation not the best one but it also can't be discarded completely. Due to lowering the number of free parameters to 5, this excludes much more strongly the lower to intermediate

mass regime with

$$\begin{aligned} \text{linear} \quad & m \geq 12.56\,\text{keV} \\ 1-\text{loop} \quad & m \geq 4.90\,\text{keV}. \end{aligned}$$

For the more detailed CT2, we don't have the properties of CT1. Instead, we get for the linear as well as the 1-loop case, two counterterm contributions that basically try to cancel each other out to get the perfect shape and are also of the same order. Here, our actual idea of an expansion of the counterterm is not preserved at all. However, this case with the same amount of parameters as the original fit then of course leads to not much worse or even slightly better χ^2 values. The same behavior was already observed for ΛCDM. Overall, we shift the freedom in the fit on the idea of an expanded counterterm. Since this is not accomplished, the fit doesn't really offer anything new and is of not much importance. Its mass constraints would be

$$\begin{aligned} \text{linear} \quad & 1.49\,\text{keV} \leq m \leq 4.84\,\text{keV} \\ & m \geq 7.03\,\text{keV} \\ 1-\text{loop} \quad & 0.94\,\text{keV} \leq m \leq 1.79\,\text{keV} \\ & m \geq 2.12\,\text{keV}. \end{aligned}$$

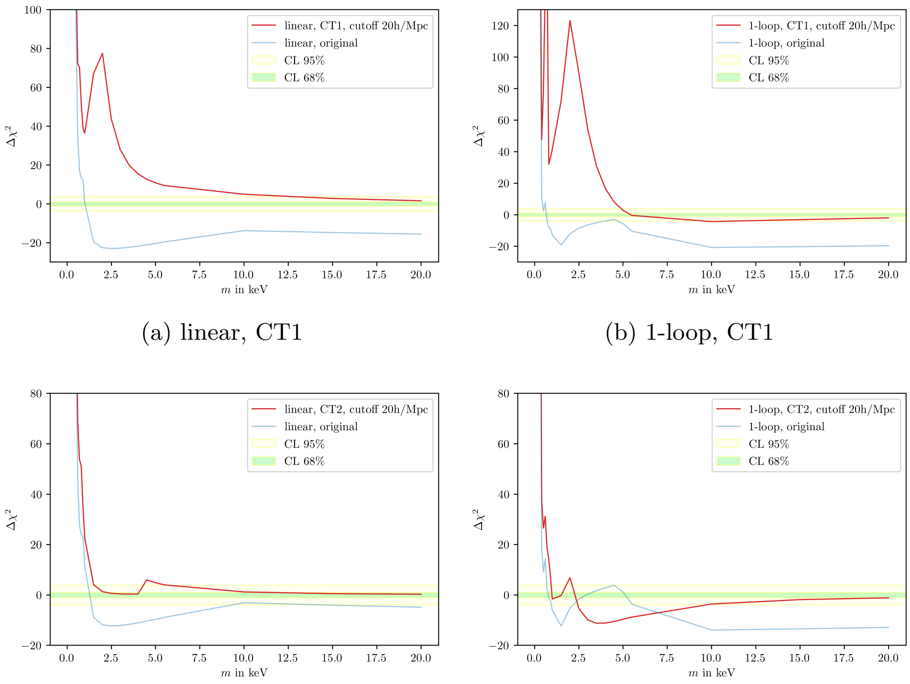

(a) linear, CT1

(b) 1-loop, CT1

(c) linear, CT2

(d) 1-loop, CT2

Figure 5.7: The linear (left) and 1-loop (right) χ^2 values minus the respective $\chi^2_{\Lambda CDM}$ for the CT1 case at the top and the CT2 case at the bottom.

5.3.4 Amplitude Restrictions

Now we get to the only new fit variation that fixes the amplitude to the values arising from the original LCDM fit. In the linear case this is $A_{lin} = 1.27$ and in the 1-loop case $A_{loop} = 0.94$. For this variation, the reference χ^2 values are the ones from the original LCDM fit. The idea is, that the only difference between the power spectra is the suppression for small scales which should be described by the counterterm and the β parameter. The amplitude shouldn't change much between the two models. However, especially the 1-loop case tries to improve the fit by preferring larger amplitudes in the regimes with stronger suppressions. When we remove this freedom, it worsens significantly in the intermediate mass regime. For large masses, we still recover ΛCDM which is a good sign. Ultimately, this fit variation also lowers the amount of free parameters which results in stronger constraints. While restrictive, they still

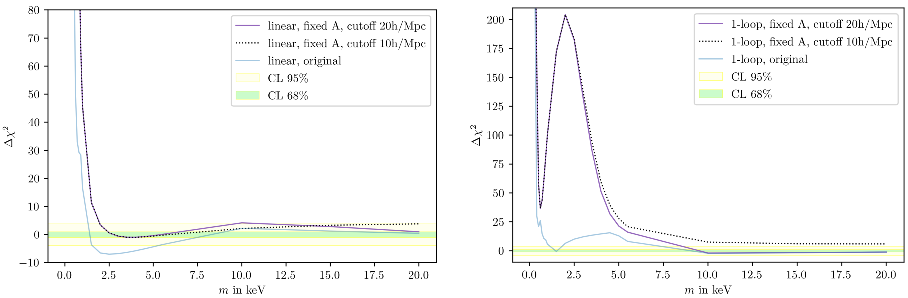

(a) linear, fixed amplitude

(b) 1-loop, fixed amplitude

Figure 5.8: The linear (left) and 1-loop (right) χ^2 values minus the respective $\chi^2_{\Lambda CDM}$ for the fixed amplitude.

seem very plausible with

$$\begin{aligned} \text{linear} \quad & 1.98\,\text{keV} \leq m \leq 9.66\,\text{keV} \\ & m \geq 11.16\,\text{keV} \\ 1\text{−loop} \quad & m \geq 8.54\,\text{keV}. \end{aligned}$$

and belong to the tightest constraints we can find.

5.4 Results

The results from all fit variations in the linear and 1-loop case are plotted all together in Figure 5.9. We can see clearly, that the fit worsens for all restrictions except CT2 which has the same amount of free parameters. This is of course expected, since we usually impose less freedom for the fit. The visibly most deviations for WDM are CT1 and a fixed Amplitude. The mass constraints we can gain from all fit variations are listed in Table 5.2 for the sterile masses and in 5.3 for the thermal ones.

One problem with these constraints are the reference values for ΛCDM explained before, because we have to compare the same fits with each other. Since the deviation allowed is only at $\chi^2 = 3.841$, a small shift in the reference

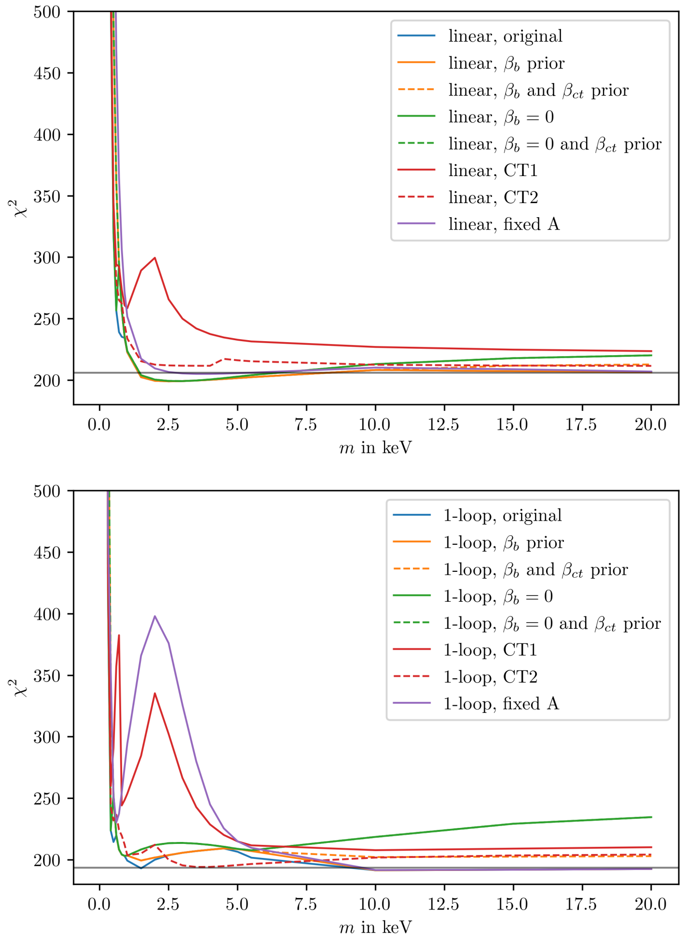

Figure 5.9: The linear (top) and 1-loop (bottom) χ^2 values for all fit variations.

fit can actually have a large impact. Thus, the fit with both priors has actually a lower value compared to only a β_b prior or to the original fit and the differences can be quite large. A similar problem arises for $\beta_b = 0$ which makes these results not very interesting. Also we have excluded the CT2 restriction since it doesn't behave according to the original idea and are also not that convinced of CT1. This leaves us with three fit variations, where we of course only use the valid 1-loop results. The most conservative one arises from the original fit with a lowest bound of

$$m_{st} \geq 1.14\text{keV} \quad m_{th} \geq 0.36\text{keV}. \tag{5.3}$$

We can arrive at much tighter constraints using the well motivated β_b prior, which leaves us with

$$m_{st} \geq 8.25\text{keV} \quad m_{th} \geq 1.58\text{keV}. \tag{5.4}$$

The fixed amplitude also produces constraints around that value, making this result quite sensible. The CT1 case results in somewhat intermediate constraints

	linear m_{st}-bounds	1-loop m_{st}-bounds
original	$m \geq 1.31\,\mathrm{keV}$	$1.14\,\mathrm{keV} \leq m \leq 1.82\,\mathrm{keV}$ $m \geq 7.34\,\mathrm{keV}$
β_b prior	$m \geq 1.31\,\mathrm{keV}$	$m \geq 8.25\,\mathrm{keV}$
β_b and β_{ct} priors	$m \geq 1.19\,\mathrm{keV}$	$0.72\,\mathrm{keV} \leq m \leq 3.70\,\mathrm{keV}$ $m \geq 5.36\,\mathrm{keV}$
$\beta_b = 0$	$m \geq 0.97\,\mathrm{keV}$	$0.39\,\mathrm{keV} \geq m \geq 0.48\,\mathrm{keV}$ $m \geq 0.52\,\mathrm{keV}$
$\beta_b = 0$ and β_{ct} prior	$m \geq 0.97\,\mathrm{keV}$	$m \geq 0.52\,\mathrm{keV}$
CT1	$m \geq 12.56\,\mathrm{keV}$	$m \geq 4.90\,\mathrm{keV}$
CT2	$1.49\,\mathrm{keV} \leq m \leq 4.84\,\mathrm{keV}$ $m \geq 7.03\,\mathrm{keV}$	$0.94\,\mathrm{keV} \leq m \leq 1.79\,\mathrm{keV}$ $m \geq 2.12\,\mathrm{keV}$
fixed A	$1.98\,\mathrm{keV} \leq m \leq 9.66\,\mathrm{keV}$ $m \geq 11.16\,\mathrm{keV}$	$m \geq 8.54\,\mathrm{keV}$

Table 5.2: WDM sterile mass bounds for all fit variations.

	linear m_{st}-bounds	1-loop m_{st}-bounds
original	$m \geq 0.40\,\mathrm{keV}$	$0.36\,\mathrm{keV} \leq m \leq 0.51\,\mathrm{keV}$ $m \geq 1.45\,\mathrm{keV}$
β_b prior	$m \geq 0.40\,\mathrm{keV}$	$m \geq 1.58\,\mathrm{keV}$
β_b and β_{ct} priors	$m \geq 0.37\,\mathrm{keV}$	$0.25\,\mathrm{keV} \leq m \leq 0.87\,\mathrm{keV}$ $m \geq 1.15\,\mathrm{keV}$
$\beta_b = 0$	$m \geq 0.32\,\mathrm{keV}$	$0.16\,\mathrm{keV} \geq m \geq 0.19\,\mathrm{keV}$ $m \geq 0.20\,\mathrm{keV}$
$\beta_b = 0$ and β_{ct} prior	$m \geq 0.32\,\mathrm{keV}$	$m \geq 0.20\,\mathrm{keV}$
CT1	$m \geq 2.17\,\mathrm{keV}$	$m \geq 1.07\,\mathrm{keV}$
CT2	$0.44\,\mathrm{keV} \leq m \leq 1.06\,\mathrm{keV}$ $m \geq 1.40\,\mathrm{keV}$	$0.31\,\mathrm{keV} \leq m \leq 0.50\,\mathrm{keV}$ $m \geq 0.57\,\mathrm{keV}$
fixed A	$0.54\,\mathrm{keV} \leq m \leq 1.78\,\mathrm{keV}$ $m \geq 1.99\,\mathrm{keV}$	$m \geq 1.63\,\mathrm{keV}$

Table 5.3: WDM thermal mass bounds for all fit variations.

but are not interesting.
Overall, our fit variations provide us with mass bounds ranging from very conservative to more tighter ones. Warm dark matter is a well studied model and therefore we have plenty of mass constraints to compare to. They are often derived from simulations, with stronger values like $m_{th} > 4.5$ [80] and others around $m_{th} > 0.55 - 3.3$ [81, 82, 78, 83]. However some concerns were raised over the accuracy of these lower limits [84, 56, 55, 85],coming primarily from the simulation of the complex IGM that doesn't follow completely the underlying dark matter density due to a few effects. First of all, it is heated from reionization which leads to thermal broadening that is together with the temperature not precisely known. Additionally, the form of the absorbing hydrogen "clouds" rely on the past thermal history and is generically smoothed compared to the DM density. This is also influenced by the reionization happening between $z \sim 5.7$ and $z \sim 8$. This makes it difficult for simulations to predict the

IGM behavior accurately.
With regard to this discussion, our most conservative result is of course still not comparable, but our tightest constraints don't deviate that much anymore. We can also compare to the results in [57] that use the same model and arrive at comparable mass bounds for WDM.
Overall, we see that our fitting method provides us with more conservative and robust constraints. With this result we can now consider DCDM.

6 | Decaying Cold Dark Matter Model

To generate the linear power spectrum for the DCDM model, we use the modified CLASS code presented in this paper [16], which is kindly freely available online. We opted for the fluid approximation explained in appendix A to compute the power spectra.
The cosmological parameters are set to almost identical values as before as seen in Table 6.1. However, since DCDM actually has an effect on the Hubble rate, it also affects the angular diameter distance $D_A(z) = \frac{1}{(1+z)H_0}\int_0^z \mathrm{d}z' \frac{H_0}{H(z')}$. This in turn shifts the angular scale of the sound horizon $\theta_s = \frac{r_s}{D_A(z_{dec})}$, so the position of the first peak in the CMB angular spectrum. However, θ_s is a very well known observable, so we decide to fix θ_s instead of H_0.
ω_{dcdm}^{ini} is fixed to the same value normal cold dark matter would have today, if no decay is happening. The densities are also always fixed via ω and not Ω which would depend on h and therefore change for very small τ and large ϵ. For CLASS to work, we also set ω_{cdm} to a very small value needed for the gauge. Our reference ΛCDM model needs to build on the same parameters, so we have a slightly different one than described before in section 4. Its results are almost identical though. To span a decent amount of parameter space, we choose 9

$100\theta_s$	1.0411
ω_b	0.0224
ω_{cdm}	0.00001
ω_{dcdm}^{ini}	0.12
$\log(10^{10}A_s)$	3.047
n_s	0.965

Table 6.1: Cosmological parameters used in generating the DCDM spectra.

different lifetimes τ as well as 14 different ϵ values being

$$\tau = \Big\{1, 3, 5, 10, 15, 20, 30, 50, 80\Big\}\text{Gyrs} \quad \text{and} \tag{6.1}$$

$$\begin{aligned}\epsilon = \Big\{&0.0001, 0.0003, 0.0007, 0.001, 0.002, 0.004,\\ &0.008, 0.01, 0.02, 0.05, 0.08, 0.1, 0.3, 0.5\Big\}.\end{aligned} \tag{6.2}$$

This results in overall 126 different parameter combinations.

6.1 Background Evolution

Before we look at the power spectra and fits, we want to give a more detailed description of the changes to the background dynamics in the DCDM model. More precisely, we focus on the Hubble rate, the cosmic microwave background (CMB) anisotropy spectra, the volume averaged distance D_V coming from baryonic acoustic oscillation (BAO) data as well as the growth rate f. This not only leads to a better understanding of the model dynamics, we can also use PLANCK and BAO data to restrict the parameter space.

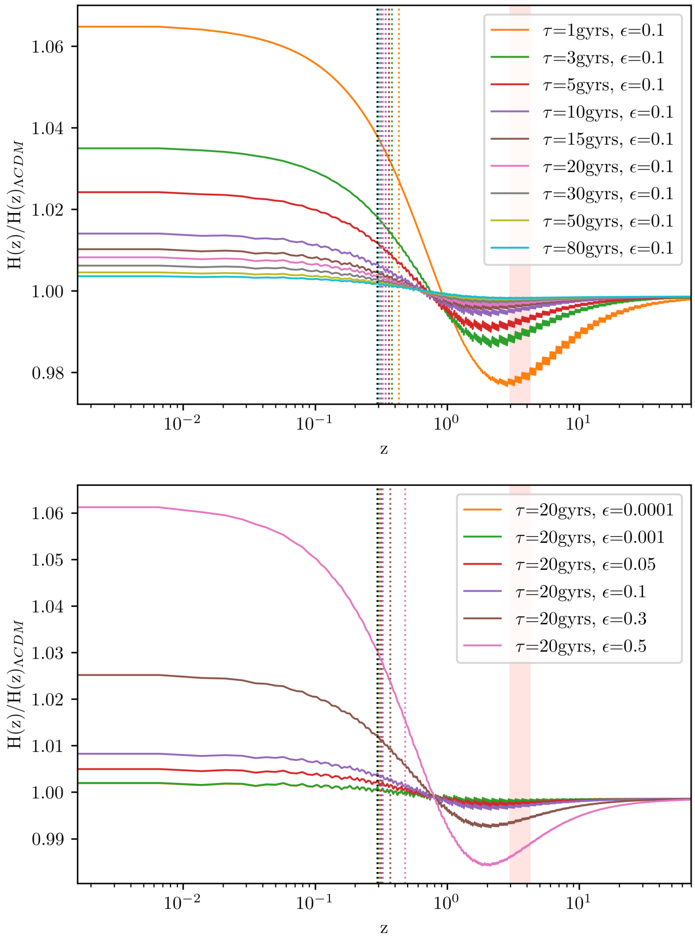

Figure 6.1: The Hubble rate depending on redshift normalized to ΛCDM for the fixed parameter $\epsilon = 0.1$ at the top and $\tau = 20$Gyrs at the bottom. The dotted colored lines correspond to the equality of matter and dark energy and the pink region to the redshifts spanned by our used data.

The Hubble rate was already shortly explained in section 2, however, here we show the Hubble rate with fixed θ_s instead of H_0. In Figure 6.1, it can be seen normalized to our ΛCDM model and for $\epsilon = 0.1$ at the top and $\tau = 20$Gyrs at the bottom. For large z, it is identical to ΛCDM as no decay has happened yet. In both cases, the Hubble rate is then first lowered and afterwards increases again. The first drop in the matter dominated universe is caused by the lower mass density which was replaced partly by dark radiation. Due to the different scaling of matter and radiation in time, radiation has a much lower contribution to the Hubble rate here. To still fulfill our required θ_s, the only remaining free parameter Ω_Λ has to increase. This accounts for the overall rise when transferring into a dark-energy dominated universe. The dotted lines correspond to the times where dark energy and matter equality is reached for the different parameter combinations. We see, that the dark energy contribution starts to dominate here. When we have very short lifetimes τ, the deviations to $\mathcal{H}$ are the largest. The drop sets in earlier in time since the matter density decreases faster and has to be compensated by a larger Ω_Λ. For large lifetimes, the deviations are in turn very small. For ϵ, it is the other way round. Large values produce the most radiation and therefore the largest deviations whereas small values are almost identical to ΛCDM. In the most extreme case of $\tau = 1$gyr and $\epsilon = 0.5$, Hubble today is almost 70% larger. All values of H_0 and Ω_Λ for each combination are summarized in tables in appendix B.1.3.

The changed Ω_Λ also has an impact on the angular CMB anisotropy spectrum. The increase in dark energy leads to more a strongly time-dependent gravitational potential which is responsible for the late integrated Sachs-Wolfe effect (LISW). Photons traveling through a density fluctuation experience a slightly different potential when moving into it compared to moving out of it. This results in a red- or blue-shift and affects only the largest modes. In the CMB spectrum, it manifests as a rise for low multipoles. In Figure 6.2 this effect is clearly visible. At the top, the extreme case of $\epsilon = 0.5$ can be seen compared to ΛCDM in blue and Planck 2018 [3] data in black, where the errorbars have been binned in steps of 10. As expected, the LISW is the largest for small lifetimes τ and gets almost negligible for large ones. At the bottom with $\tau = 20$Gyrs, we see the contrary trend for ϵ. Large values give the most deviation, small values the least.

Another set of measurements comes from utilizing baryonic acoustic oscil-

Measurement	z	D_V in Mpc
6dF [86]	0.11	456±27
BOSS DR10 [87]	0.32	1262±36
	0.57	2034±28
SDSS-3 DR12 [88]	0.38	1477±16
	0.51	1877±19
	0.61	2140±22
SDSS-4 [89]	0.85	2689±56
eBOSS DR14 [90]	2.34	4626±200

Table 6.2: BAO datapoints for 8 different redshifts.

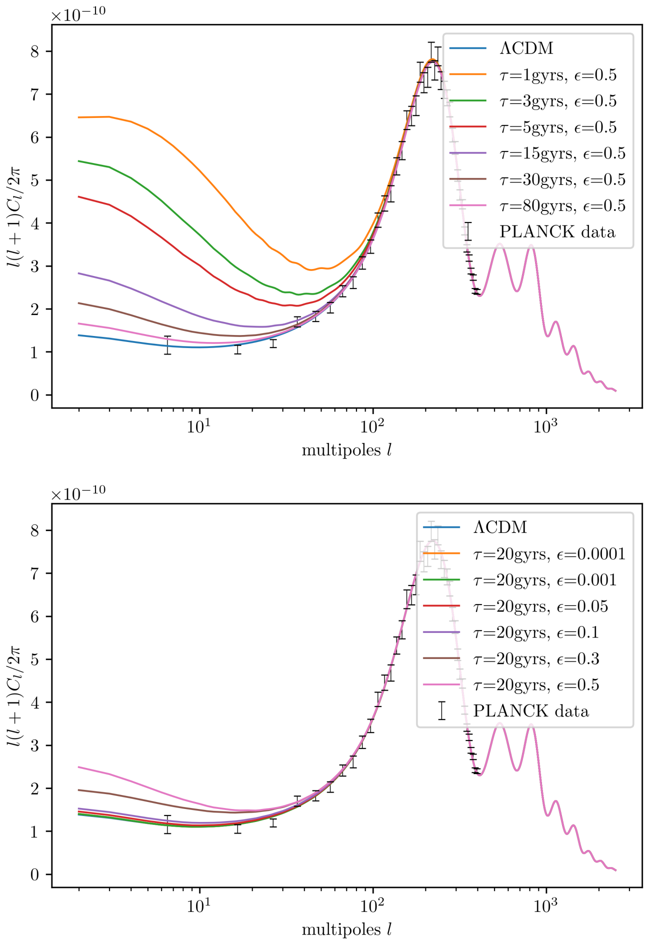

Figure 6.2: The CMB anisotropy spectrum for $\epsilon = 0.5$ at the top and $\tau = 20$Gyrs at the bottom. The errorbars are from Planck 2018 [3] and are binned in steps of 10 to increase the readability of the plot. For comparison, ΛCDM is plotted in blue.

lations. Its scale is determined by the sound horizon $r_s = \int_{z_d}^{\infty} c_s(z)/H(z)\mathrm{d}z$ with the sound-speed c_s and decoupling redshift z_d. Usually, ratios of the co-moving angular diameter distance D_M to r_d and Hubble to r_d are measured [91], where we have $D_M(z) = \int_0^z \mathrm{d}z'/H(z')$, when disregarding curvature. This then effectively constrains the volume averaged distance

$$D_V(z) = \left(\frac{zD_M(z)^2}{H(z)}\right)^{1/3}. \tag{6.3}$$

A few datapoints for redshifts between 0.1 and 2.4 are summarized in Table 6.2. They were taken from [86, 87, 88, 89, 90], each analyzing different data sets. This data can then be compared to D_V from our models that can be seen in Figure 6.3. A lifetime of $\tau = 1$Gyrs is plotted at the top and $\epsilon = 0.1$ at the bottom. Due to the larger Hubble radius at small redshifts, the angular diameter distance decreases up until large enough z, where the decrease in Hubble balances this effect out again. Thus, we see a suppression that disappears again for larger z. Like before, small τ and large ϵ produce the strongest deviations while medium values only have small differences.

For the growth factor, we have to solve the Mészáros equation describing the

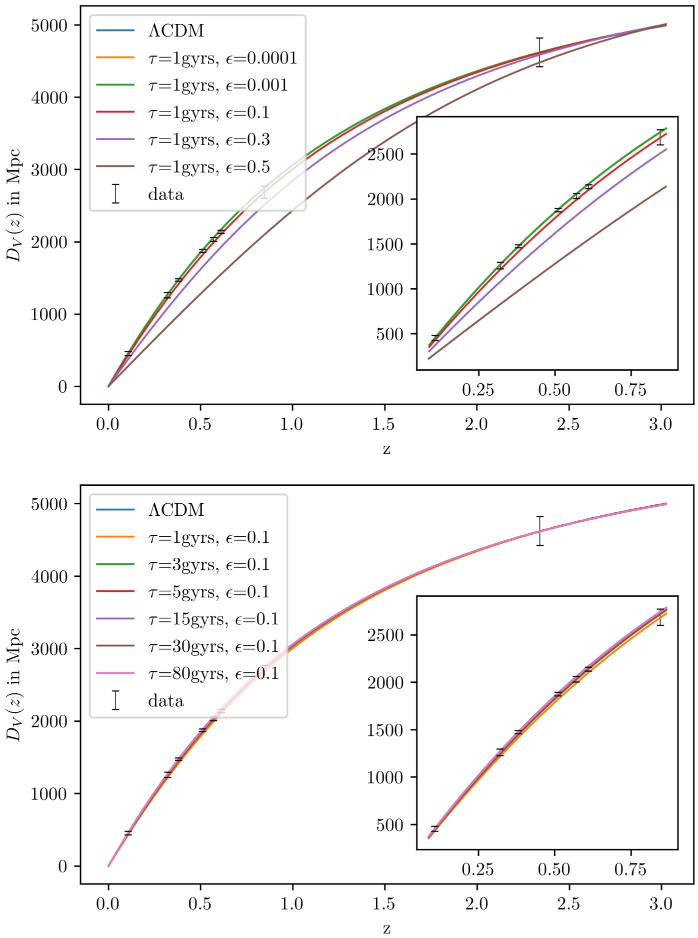

Figure 6.3: The volume averaged distance $D_V(z)$ for $\tau = 20$Gyrs at the top and $\epsilon = 0.1$ at the bottom. The deviations are only small and only really relevant for extreme τ and ϵ values.

evolution of matter densities. For subhorizon scales with $k \ll \mathcal{H}$ and neglecting radiation perturbations, it takes the form

$$\frac{\mathrm{d}^2\delta}{\mathrm{d}a^2} + \left(\frac{\mathrm{d}\ln(H)}{\mathrm{d}a} + \frac{3}{a}\right)\frac{\mathrm{d}\delta}{\mathrm{d}a} - \frac{3}{2a^2}\frac{\rho_m}{\rho_{\mathrm{crit},0}}\frac{H_0^2}{H^2}\delta = 0 \tag{6.4}$$

where $\rho_m = \rho_{dcdm} + \rho_{wdm}$ for our DCDM model. Initially, at an a after decoupling but way before equality between matter and dark energy is reached, we are in a matter dominated universe and hence expect $\delta = a$. With this starting condition, we can solve equation 6.4 numerically and plot the growth function $D(a)$ as well as the growth rate $f(a) = \mathrm{d}\ln(D)/\mathrm{d}\ln(a)$. The solution can be seen for $\tau = 20$Gyrs in Figure 6.4 with $D(a)$ at the top and $f(a)$ at the bottom. We see that the growth of structure is impaired compared to pure CDM. This is not surprising considering the lower amount of matter density that can actually cluster. Again, deviations are the largest for small τ and large ϵ.

The space telescope Euclid developed by the European Space Agency and

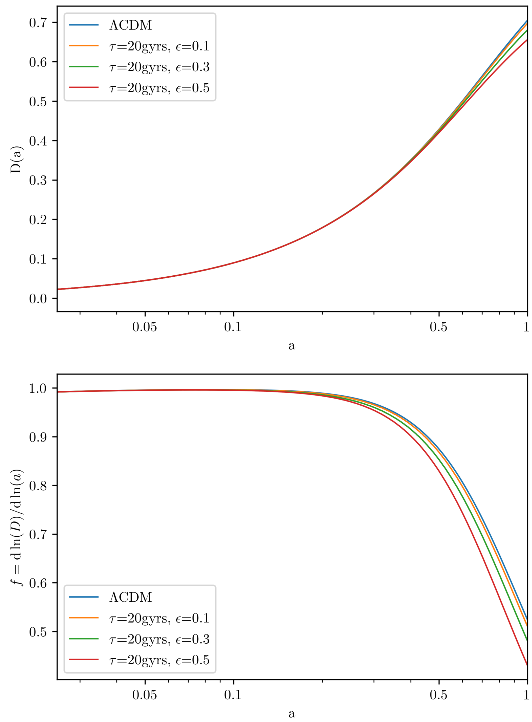

Figure 6.4: The growth function $D(a)$ for $\tau = 20$Gyrs at the top and the growth rate f at the bottom. The growth of density fluctuations is slowed for the DCDM models due to the higher dark energy density. Therefore, the deviations also occur for later times.

scheduled for takeoff in 2023 will focus mostly on dark energy and its effect on cosmic structures. It will however also constrain the growth rate. Estimates for the precision of the upcoming measurements are at around $1 - 2.5\%$ for the growth rate depending on the redshift [43]. Their data can be used to constrain various cosmological models including DCDM. In Figure 6.5 the deviations for $\epsilon = 0.1$ at the top and $\tau = 10$Gyrs at the bottom to ΛCDM are plotted. We can see that the large $\epsilon \gtrsim 0.1$ values and smaller $\tau \lesssim 10$Gyrs will definitely be in the precision range currently proposed. Depending on the actual measurements and a more accurate analysis for the DCDM models, even more parameter space might be testable via the growth rate.

For each of these background quantities, we already see one important property of DCDM: The two describing parameters τ and ϵ are degenerate and can bal-

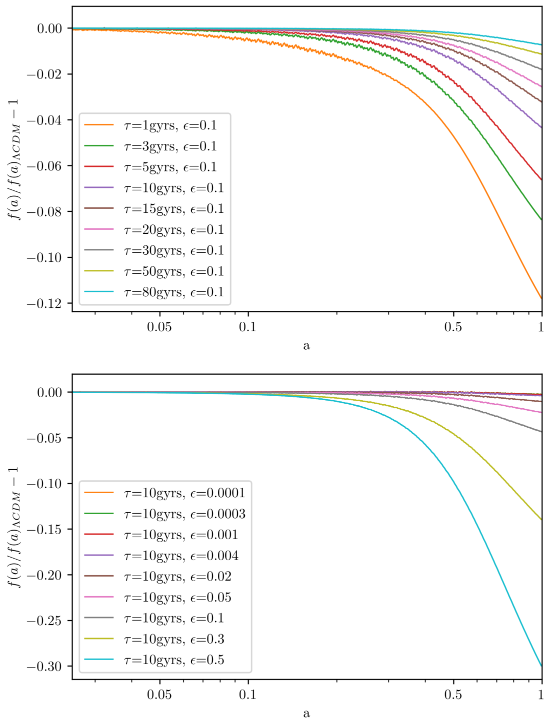

Figure 6.5: The growth rate f normalized to ΛCDM for $\epsilon = 0.1$ at the top and $\tau = 10$Gyrs at the bottom.

ance out each others effects. For either large lifetimes or very small ϵ we should always generate ΛCDM regardless of the other parameter choice. In turn, the small τ and large ϵ regime can be constrained the most by the background evolution. For a complete analysis an MCMC approach would of course be the best but goes a bit beyond the scope of this work. With our limited setup, we can at least analyze our data compared to the ΛCDM one. For this, our ΛCDM model is set as the "best fit" and we compute the χ^2 of the DCDM models as the difference of the data points to the model divided by the error squared. This is done for the BAO data as well as the Planck data since we have errorbars to work with. In Figure 6.6, the computed $\Delta\chi^2$ values which are compared to the ΛCDM values, are shown for the Planck Data as well as for the BAO data. The allowed maximum deviation can now be set admittedly a bit arbitrary. We show both a tight (dashed line) and a more lax (solid line) constraint in the parameter space. For Planck we allow for maximally $\Delta\chi^2 \leq 30$ while we allow for $\Delta\chi^2 \leq 10$ for BAO which has much less data points and therefore a much lower χ^2 in the first place. The excluded parameter space is marked by the black lines. In both cases, we see nicely that it worsens towards the upper left corner and shows the degeneracy for τ and ϵ. For the BAO data, we actually see a band spanning from the left bottom to the right top corner with a better fit to the data than our reference model. Interestingly, it doesn't encompass the lower right corner including the parameters for which DCDM converges to ΛCDM indicating it may not be the best explanation for the BAO data.

In the end, we will still fit to all parameters later on, but this treatment of CMB and BAO data still serves as an indicator which parameter combinations are actually compatible with other measurements and are therefore more interesting to look at. In-depth analyses are commonly done in the literature and we will later compare them.

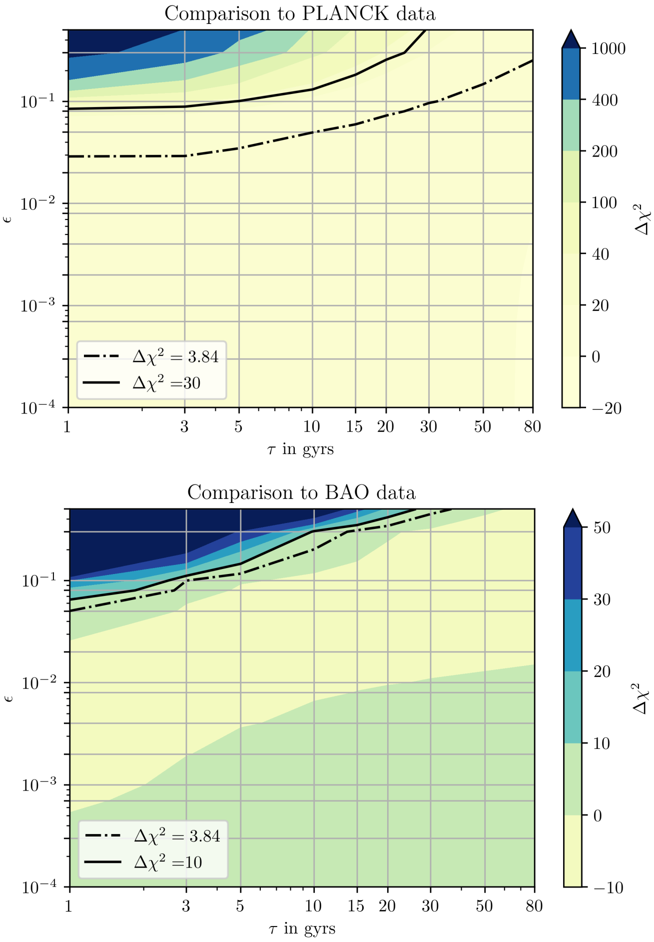

Figure 6.6: The $\Delta\chi^2$ values for the Planck and BAO data compared to ΛCDM. The black line shows what parameter space would be excluded for a deviation of 30 at the

6.2 Power Spectra and Integrals

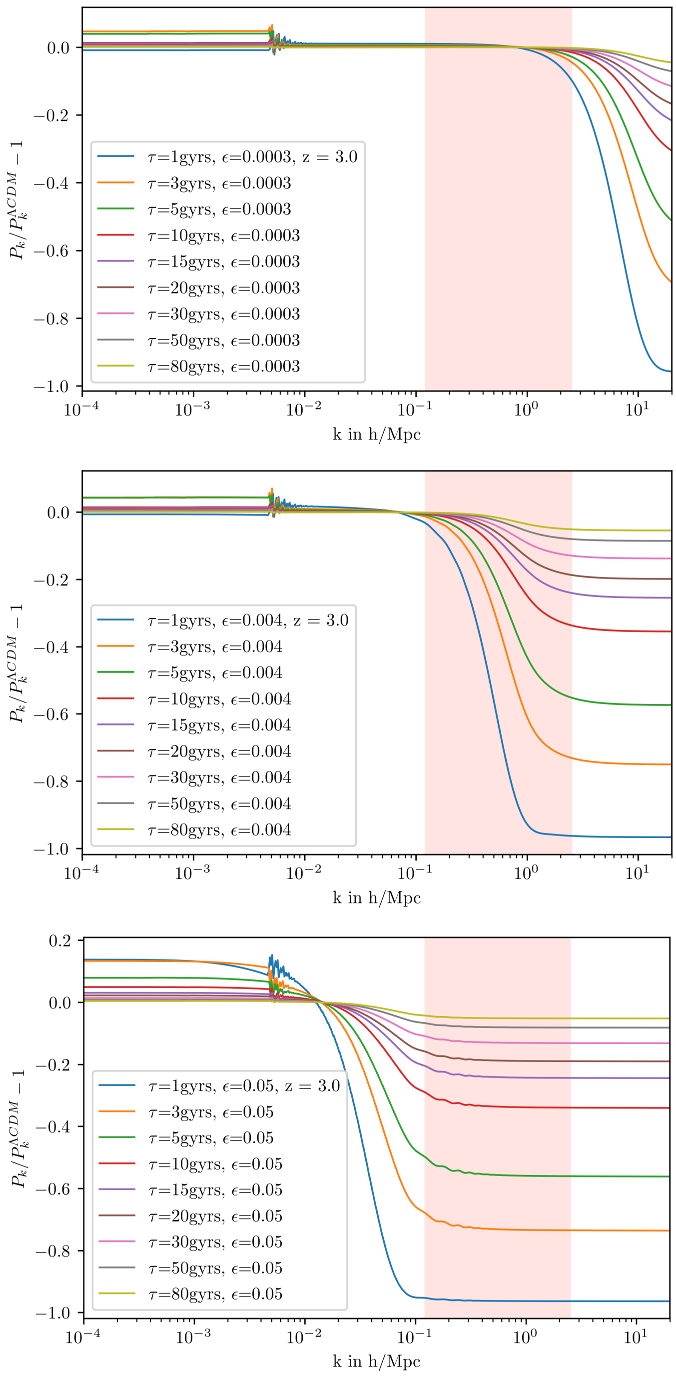

Figure 6.7: The DCDM power spectrum normalized to ΛCDM for $\epsilon = 0.0003, 0.004, 0.05$ from top to bottom. The pink region represents as always the BOSS data regime.

The effects of the WDM and DR can be nicely seen in the power spectra. In Figure 6.7, three plots for all lifetimes and with the values $\epsilon = 0.0003, 0.004, 0.05$ can be seen from top to bottom. The oscillatory behavior at around $k \approx 0.005$h/Mpc stems from the switching to the fluid approximation happening far away from our region of interest. The power spectra are normalized to ΛCDM and show the suppression based on τ. The smaller the lifetime, the stronger is the suppression while it sets in at the same time. Additionally, this parameter sequence shows the suppression shifting more to larger scales, the higher ϵ gets. With our ϵ parameters, we can look at three different cases. One, where the suppression starts left of the BOSS region and it is constant in this regime for $\epsilon \gtrsim 0.05$. A second one, where the suppression is happening in the region of interest for $0.05 > \epsilon > 0.0003$. And a third one, where the suppression has not happened yet and there is almost no difference to ΛCDM for $\epsilon \lesssim 0.0003$.

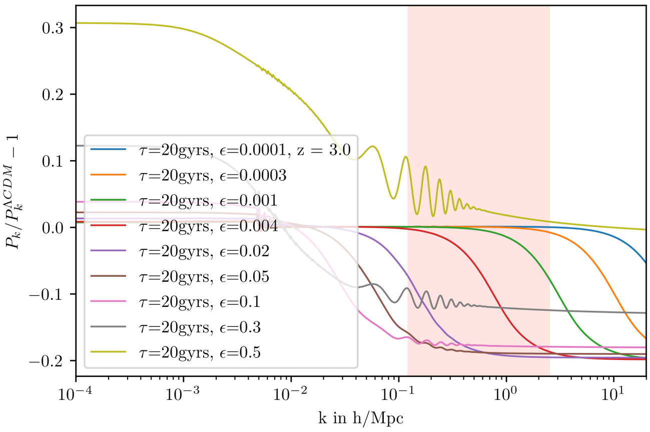

Figure 6.8: The DCDM power spectrum normalized to ΛCDM for $\tau = 20$Gyrs.

In Figure 6.8, we switch to a fixed $\tau = 20$Gyrs and show several ϵ values. Again we see that ϵ is responsible for the position of the cutoff. This is the same as in the WDM model where the mass determines the cutoff scale. A difference in behavior only starts for $\epsilon \leq 0.1$ where the warm daughter isn't warm anymore but quite hot. This causes the free streaming scale to be larger than the Hubble scale and no clustering can happen for WDM. Thus, we get two competing effects. The density responsible for clustering is of course decreasing leading naively to a stronger suppression. However, the smaller Hubble rate leads to an easier clustering process, compensating for the lower density. In turn, there is no suppression for $\epsilon = 0.5$ at $z = 3.0$ anymore. This trend is already visible for $\epsilon = 0.1$ and 0.3. Another effect comes from the larger H_0 and therefore h today shifting the k values to the left. This includes the peak of the power spectrum at k_{eq} which is determined by radiation and matter equality that is unchanged in our model. Thus, the peak is shifted towards the left for large H_0 deviations and the large scales are elevated. Lastly, in Figure 6.9, we show the z-dependency as well as the 1-loop spectra for $\tau = 20$Gyrs and $\epsilon = 0.001$. It is normalized to the respective ΛCDM $P_{\delta\delta}$, $P_{\delta\theta}$ and $P_{\theta\theta}$ spectra but all at $z = 3.0$. Thus, we see the overall lowered amplitude for higher redshifts as well

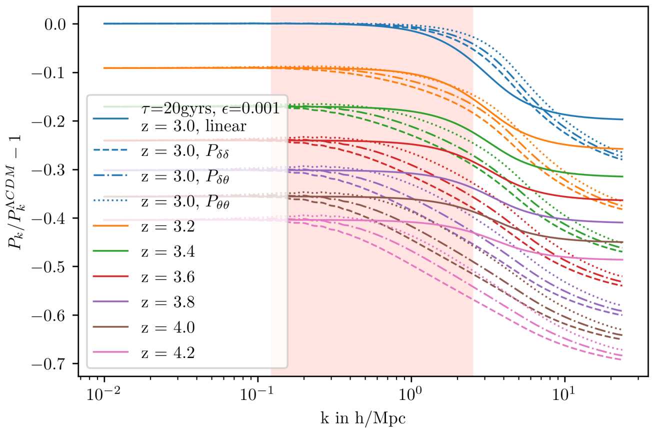

Figure 6.9: The $P_{\delta\delta}$, $P_{\delta\theta}$ and $P_{\theta\theta}$ spectra for $\tau = 20$Gyrs and $\epsilon = 0.001$ and all redshifts. The normalization is with respect to the respective ΛCDM spectra but always at $z = 3.0$

as the suppression in the 1-loop spectra. Similar to WDM, the $P_{\theta\theta}$ spectrum receives the largest deviations compared to ΛCDM. Additionally, we see again the different shape, that arises from the 1-loop spectra. The cutoff scale is again shifted slightly towards larger k values and the suppression is afterwards a bit steeper.

The characteristics of the power spectrum are naturally imprinted on the integrals. The effect on I_0 can be seen in Figure 6.10 on the top row, with the linear (dotted) and 1-loop (solid) case at $z = 3.0$. I_2 and I_4 are visible at the bottom for $\tau = 20$Gyrs. We observe, that small τ are suppressed tremendously. Regarding the plotted ϵ, we see the largest suppression for $\epsilon = 0.01$. For larger values, the shape is significantly changed and it increases again, which we have also seen in the power spectra.

Again, we also test the cutoff dependency of the integrals and additionally include a check for the cutoff scale of 25h/Mpc. All integrals for 10h/Mpc compared to 20h/Mpc as well as 20h/Mpc compared to 25h/Mpc can be seen on the left and right of Figure 6.11. Even for I_0, the deviations are only at about 2% for the latter case, and only around 0.1% for the higher integrals. This proves nicely their convergence. Nonetheless, we still compute our upcoming fits for both cutoffs to make sure, the minimization is doing its job properly.

6.3 Fits

6.3.1 Original Fit

Now, we can look at our performed fit and its variations, namely a β_b and β_{ct} prior as well as an amplitude restriction for the larger ϵ values. Since we have slightly different cosmological parameters, the χ^2 for ΛCDM also changes in the decimal place. In Table 6.3, we show the new reference values for the two cases that interest us here. As usual, the different fits are compared to their respective reference value.

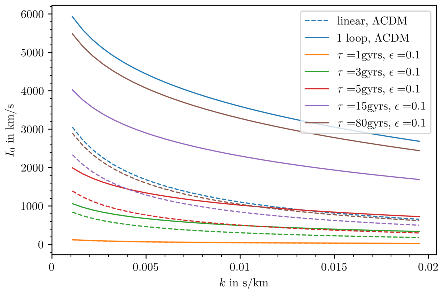

(a) I_0 for $\epsilon = 0.1$

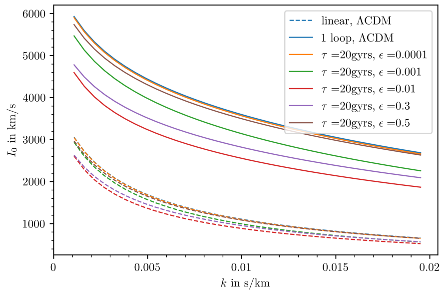

(b) I_0 for $\tau = 20$Gyrs

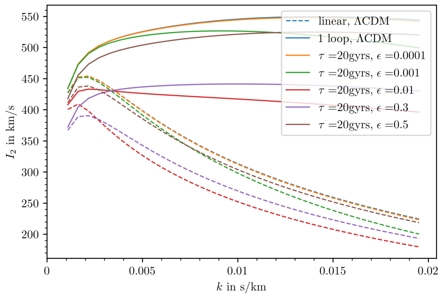

(c) I_2 for $\tau = 20$Gyrs

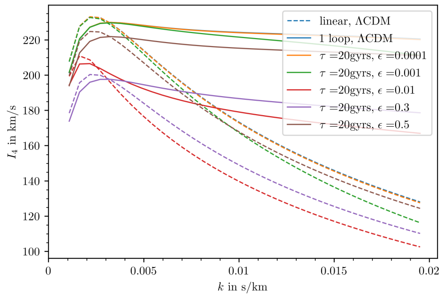

(d) I_4 for $\tau = 20$Gyrs

Figure 6.10: The shape of the integrals I_0, I_2 and I_4.

First, we start with the original fit in Figure 6.12. Here, all $\Delta\chi^2$ values are

	linear χ^2	1-loop χ^2
original	206.20	193.44
β_b and β_{ct} prior	211.24	203.52

Table 6.3: The reference χ^2 ΛCDM values for the DCDM fits.

plotted for each point in the parameter space. Dark colors indicate a large deviation from ΛCDM and aren't compatible, while lighter colors indicate a similar or even better fit.
In the linear case, we can see a larger excluded region starting from the intermediate ϵ values for the smallest lifetimes and tapering towards a lifetime around the age of the universe. The parameter space below, with smaller ϵ values, is actually preferred over ΛCDM. These are values that produce a decent suppression in the BOSS regime when compared to the power spectra as seen in Figure 6.7. Higher lifetimes will produce less of a suppression but can compensate somewhat with higher ϵ values due to their degeneracy. Thus, the shape of this preferred region curves upwards. In the excluded region directly above, the suppression sets in too early, which doesn't fit well to the BOSS data. Only starting at $\epsilon \simeq 0.05$, where the suppression starts before the BOSS region and is already a constant in the relevant k regime, the fit improves again. The suppression can be counterbalanced by a higher amplitude in this regime, to get

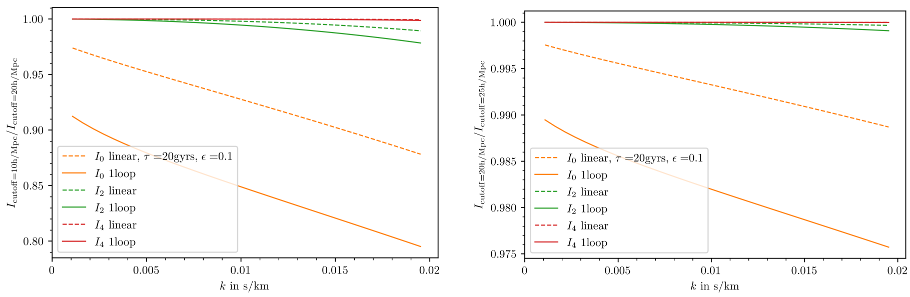

Figure 6.11: The integral ratio for the cutoff scales 10 and 20h/Mpc at the top and 20 and 25h/Mpc at the bottom. The deviation decreases greatly and shows the convergence of the integrals.

effectively ΛCDM again. For high lifetimes and low ϵ, all effects are reduced and we also have a similar fit to ΛCDM.
In the 1-loop case, the excluded region is much broader in the ϵ regime. Especially the high ϵ regime isn't compatible with ΛCDM anymore. This stems from the 1-loop corrections causing the power spectrum to not be a constant anymore in the BOSS regime but to actually experience a suppression and scale dependency. For small τ, this effect is too strong and can't be properly absorbed by a larger amplitude. The lower end of the ϵ regime is also more tightly constrained. Overall, this suggests that the 1-loop case is much more sensitive for the shape and strength of the suppression which is more dependent on τ. Additionally, we don't have a preferred region anymore as in the linear case. The only relic is a small parameter region that performs slightly better than the ones around. For large τ, we again converge to ΛCDM as expected.
Overall, we observe a similar effect as in WDM. While the linear case prefers a certain parameter region depending solely on the onset of the suppression, the 1-loop case is much more sensitive to the actual shape of it and removes the preference. Thus, it can help in reducing the degeneracy in τ and ϵ. Additionally, it also provides tighter constraints.

In Figure 6.13, we see a similar plot but for concrete contours at $\Delta\chi^2 = \pm 3.841$ corresponding to a 95% confidence interval around ΛCDM and at $\Delta\chi^2 = \pm 0.989$ corresponding to 68%. These define the range where DCDM is compatible to ΛCDM. A larger $\Delta\chi^2$ leads to an exclusion and a lower one to a preference. This visualizes better the actual constraints for which the DCDM model agrees with the data. Dark blue is excluded, middle blue, turquoise and middle green is compatible and the light yellow-green shows a better fit.
In the linear case, we see that the excluded region starts from $\epsilon \sim 0.0007$ and reaches $\tau = 50$Gyrs at $\epsilon = 0.08$. The preferred region goes up to $\epsilon \sim 0.002$ at $\tau \sim 20$Gyrs. In the 1-loop case, we see better how large the excluded region is for the ϵ values. Starting from $\tau \sim 18$Gyrs all values are actually compatible to ΛCDM. Additionally, the fit converges better towards ΛCDM for higher τ. We can overall notice, that the linear case is more sensitive to the ϵ values, so the onset of suppression, whereas the 1-loop case is more sensitive towards the τ values, so the strength of the suppression.

In Figure 6.14, the contours around the best fit value of DCDM are plotted. Since we are now comparing to a model with 2 free variables, the contours

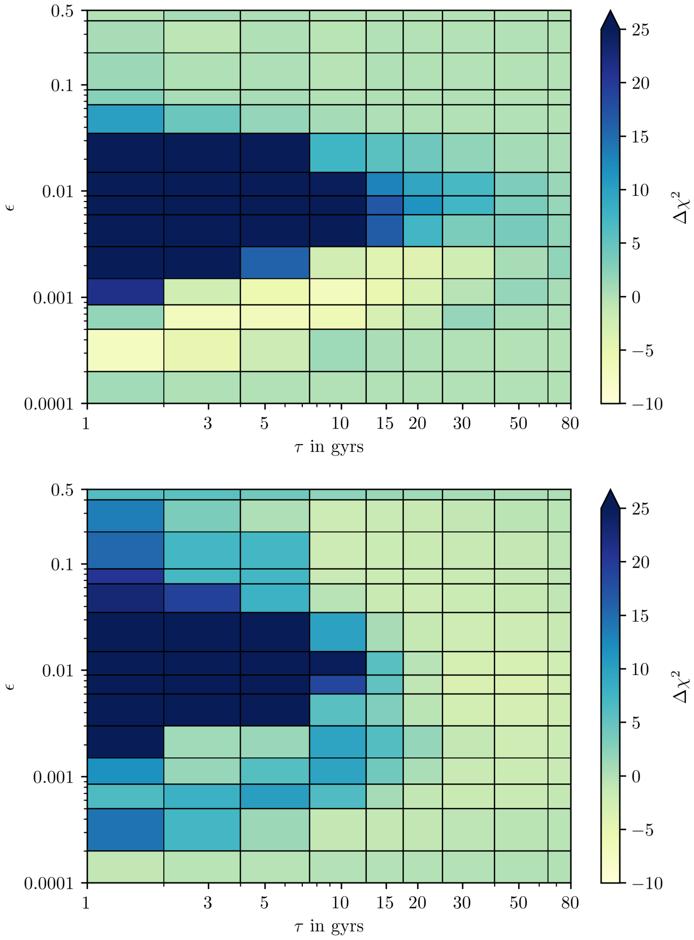

Figure 6.12: $\Delta\chi^2$ plot in the 2d parameter space for τ and ϵ. Light colors indicate a good fit, while darker colors indicate a worse fit.

change to $\Delta\chi^2 = 5.991$ and $\Delta\chi^2 = 2.279$ for 95% and 68%, respectively. These are indicated by the solid and dashed lines, while the best fit position is marked with a black dot.
In the linear case, we can clearly see the preference for the low τ regimes with the best fit being actually at $\tau_{\text{bestfit}} = 1\text{Gyrs}$, $\epsilon_{\text{bestfit}} = 0.003$ with an uncorrected $\chi^2 = 199.00$. It is so strong, that the other compatible regimes that converge to ΛCDM aren't included here anymore. Since it disappears after non-linear corrections, this stems from a different shape of the integrals due to a false treatment of the smaller scales and shows how much impact non-linearities can have. The 1-loop case looks much more sensible, with a best fit value at $\tau_{\text{bestfit}} = 30\text{Gyrs}$, $\epsilon_{\text{bestfit}} = 0.008$ with $\chi^2 = 190.02$. and a general preference for large τ values. $\epsilon = 0.0001$ is also still included, since it imitates ΛCDM. This result has of course more validity than the linear one and also seems to be quite reasonable.

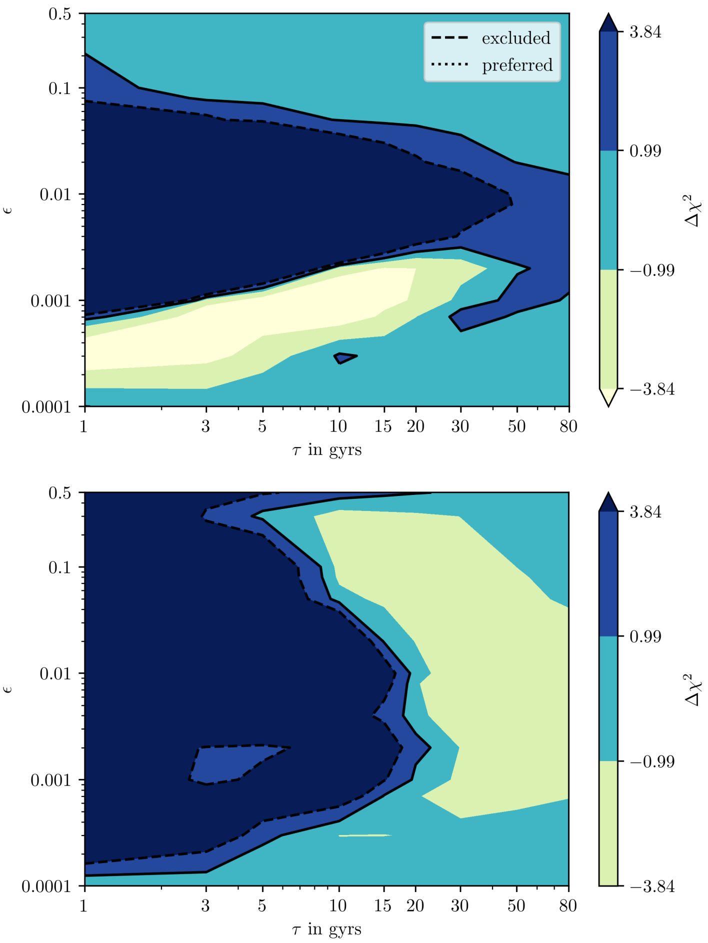

Figure 6.13: Contours for the comparison to ΛCDM in the 2d parameter space. Dark blue indicates the excluded region, light green the preferred one.

6.3.2 β_b and β_{ct} Restrictions

Now, we get to the first fit variation, an implementation of a β_b and β_{ct} prior with again $-10 < \beta_{b,ct} < 10$. We already discussed before, that this is physically well motivated. In Figure 6.15, the resulting contours with comparison to ΛCDM are shown at the top. On the left hand side, the linear plots can be seen, on the right hand side, the 1-loop ones. The overall shape, especially of the excluded regions, is very similar to before. Mostly, the boundaries are shifted a bit to more conservative values. Naively, we would expect the opposite to happen. However, this shows again the problem with the reference value we get from ΛCDM. In the the linear as well as the 1-loop case, we get additional preferred regions and the overall plot seems less smooth and more patchy. For a better understanding, we also display the contours more highly resolved under the normal plots. This shows, that the new preferred regions are relatively small and don't have a strong decrease in $\Delta\chi^2$. Instead the values are relatively close

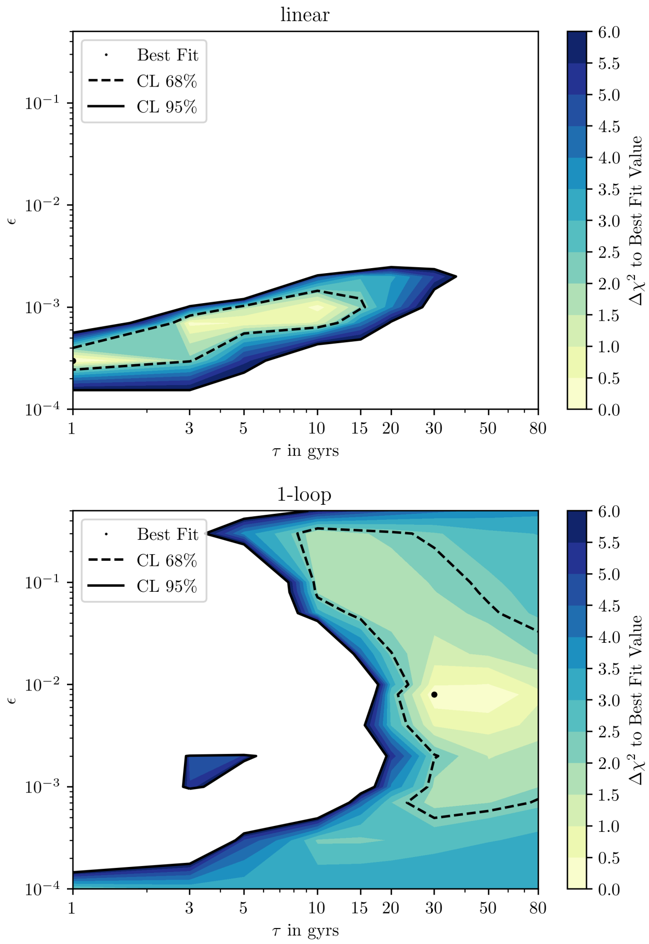

Figure 6.14: Contours around the best fit DCDM value, marked by a black dot, in the 2d parameter space. The solid and dashed black lines indicate the 95% and 68% confidence intervals.

and these preferred regions are not very sensible.
Thus, we can mostly see, that the exclusion shape is preserved which reinforces their robustness in the original fit.

6.3.3 Amplitude Restrictions

The last fit variation we apply, is a restriction for the amplitude. This idea comes originally from studying massive neutrinos with Lyman α data (see [92] and [64]) but can be partially applied here.
The argument goes as follows: Massive neutrinos lead to a suppression which starts well before the BOSS regime and is almost scale-independent there. The fit amplitude can now absorb this suppression almost completely by increasing. This makes it difficult to differentiate between effects from the neutrino masses and the normalization of the primordial power spectrum and causes a degener-

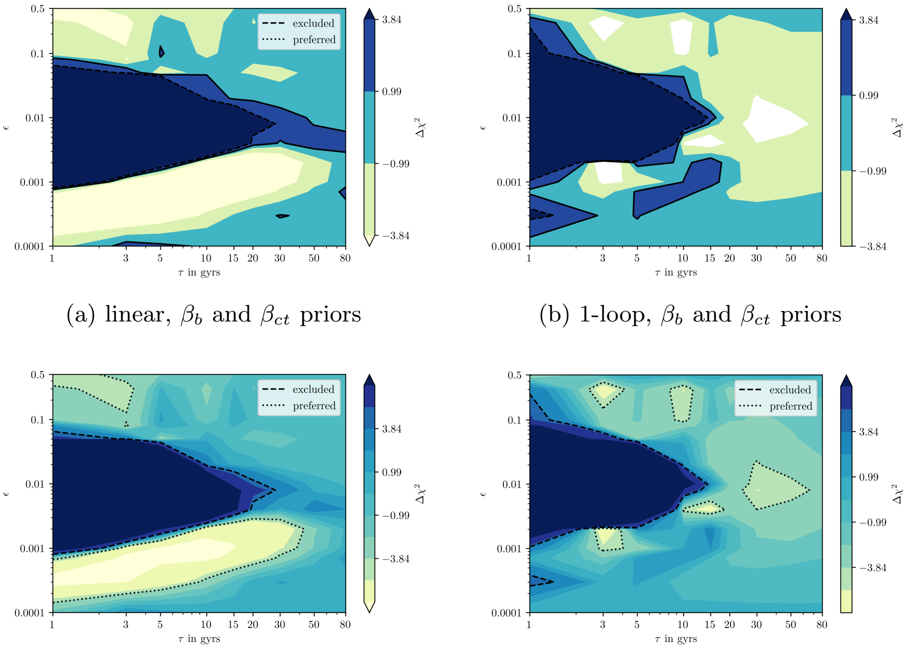

(a) linear, β_b and β_{ct} priors

(b) 1-loop, β_b and β_{ct} priors

(c) linear, more detailed

(d) 1-loop, more detailed

Figure 6.15: Contours for the comparison to ΛCDM in the 2d parameter space with priors for β_b and β_{ct}. On the left side are the linear results, on the right side the 1-loop results. Dark blue indicates the excluded regions, light green the preferred ones on the top. The bottom row shows the same plot but in more detail.

acy.
The same concept applies to the DCDM spectra under certain conditions. For $\epsilon \geq 0.05$, the cutoff in the power spectrum has happened before the BOSS regime and we get also an almost scale-independent suppression similar to massive neutrinos. Thus, we would also expect a degeneracy between A and the physical properties of DCDM in this regime. To deal with this, we follow the same approach as in [64]: We look at the linear DCDM and ΛCDM spectra for $k \ll k_{fs}$, so long after the drop, and compute their ratio $R^{-1} = P_{\Lambda\text{CDM}}/P_{\text{DCDM}}$. To account for the lower spectrum, the fit amplitude A should increase and compensate for this. We can calculate this new amplitude by

$$A = A_0 \cdot R^{-c}, \tag{6.5}$$

where A_0 is the fitting amplitude for the ΛCDM in the linear or 1-loop case, respectively. In that way, we relate A to the ΛCDM case, which already includes the primordial normalization, and keep it the same. The parameter c allows for more flexibility in this model and was calibrated by mock simulation data in [64] for neutrinos. We are not doing this here however, instead we use the simplest case with $c = 1$. This gives us a fixed amplitude for every set of τ and ϵ parameters this method can be applied to. Since we can't describe the cutoff, we restrict the parameter space here to $\epsilon \geq 0.05$ and thus test 45 parameter

points.
One issue is, that we fit several redshifts at the same time but also have a slightly z dependent R ratio. In the most extreme case, the deviations can go up to $\sim 50\%$ and are still at $\sim 5\%$ at $\tau = 20$Gyrs. There are several ways, we can deal with this problem. Naively, one could take the mean amplitude in the z regime as a fixed value. This however has one certain disadvantage. The z_{pivot} used in our analysis is at $z = 3.0$, so this redshift takes a bit of a special place. In this case, the β parameters describing the redshift dependency are irrelevant and we effectively only have 3 instead of 6 parameters left, that actually have an impact on the goodness of fit. Therefore, a mean amplitude is way more problematic for $z = z_{pivot}$ since there are less parameters to compensate for a deviating amplitude. Instead, this redshift is the most important one while fitting. This is why we decided to fix the amplitude for $z = 3.0$. To account for the z dependency, we instead impose priors for A around a fixed amplitude so we allow for more variance. Overall, we study three different cases. A fixed amplitude at $z = 3.0$ as the strongest restriction, an allowed 5% and 10% deviation around the fixed value as an intermediate limitation and of course the free amplitude case as the most conservative one. This should give us a good range to investigate the role of the amplitude.
In Figure 6.16, the different amplitudes for $\tau = 20$Gyrs are plotted. The green

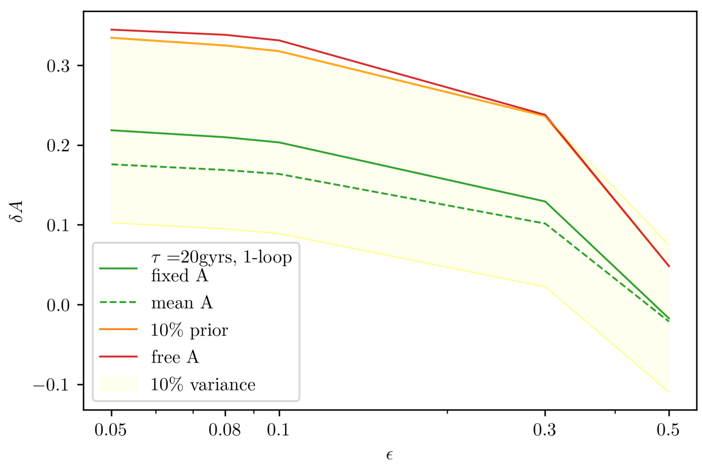

Figure 6.16: The deviation to the ΛCDM amplitude for the different A restrictions at $\tau = 20$Gyrs and 1-loop. The yellow band indicates the 10% region around the fixed amplitude. A with imposed prior traces the free amplitude as long as it is allowed.

line corresponds to the fixed one and we indicate the 10% range around it. The dashed line also shows the mean amplitude we checked. It is visibly smaller than the fixed one, while the fit prefers larger values as seen with the free case. Thus, we discarded it. The A with prior strives as far as it is allowed towards the free one and stops when it reaches it.

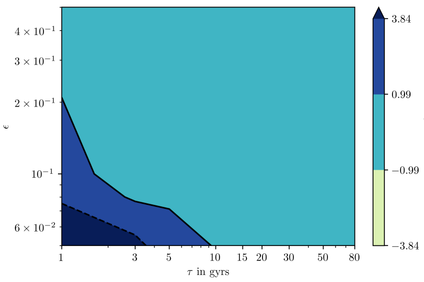

(a) linear, free amplitude

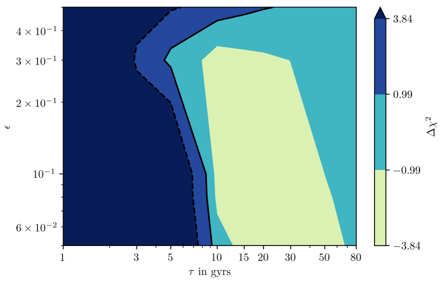

(b) 1-loop, free amplitude

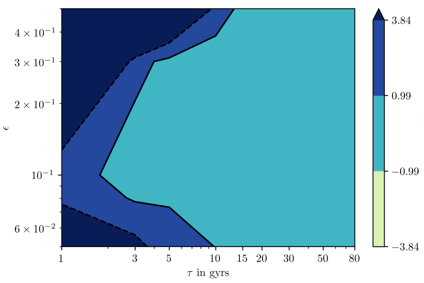

(c) linear, A prior at 10%

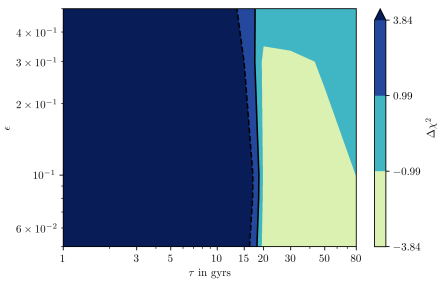

(d) 1-loop, A prior at 10%

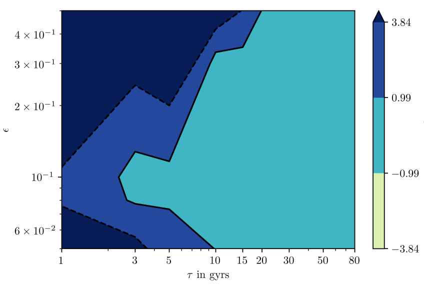

(e) linear, A prior at 5%

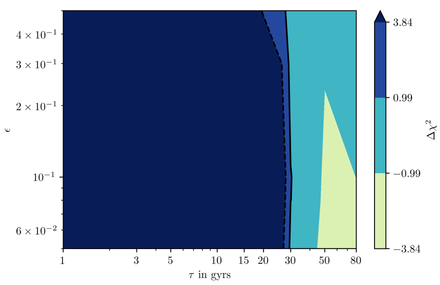

(f) 1-loop, A prior at 5%

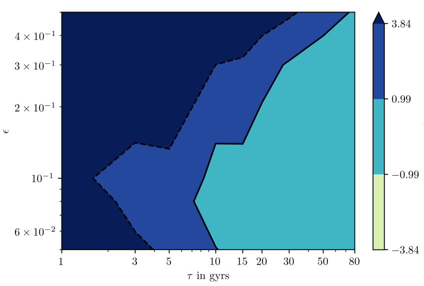

(g) linear, fixed amplitude

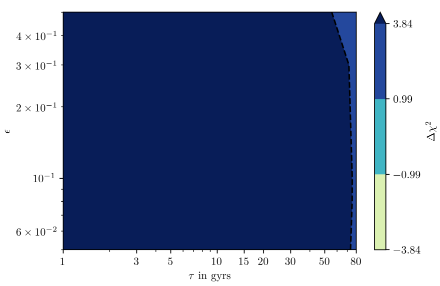

(h) 1-loop, fixed amplitude

Figure 6.17: Contours for the comparison to ΛCDM in the 2d parameter space with different levels of amplitude restriction. The left side shows the linear plots, the right one the 1-loop plots. Dark blue indicates the excluded region, light green the preferred one.

We also see an overall decline for higher ϵ. This comes from the same effect we have already seen for the power spectra, where the radiation balances the suppression more and more due to the lower Hubble friction.
The contours compared to ΛCDM for these discussed cases can be seen in Figure 6.17. On the left side, we have the series of linear fits going from the free amplitude to the completely fixed one. On the right side, the same is plotted for the 1-loop fits. In both cases, we can nicely see how the parameter space gets more and more restrained. For the linear case, the amplitude mainly restricts the upper ϵ area whereas in the 1-loop case, it is pretty insensitive to the ϵ value and is also more restrictive in general. This confirms, what we have already seen before. The non-linear corrections lead to a scale dependency that can exclude more from the parameter space. For the fixed A, almost everything is excluded and only the highest lifetimes with $\tau \geq 80$Gyrs are compatible again. The 5% and 10% priors give intermediate results at $\tau \geq 30$Gyrs and $\tau \geq 20$Gyrs, respectively. They give probably the most sensible constraints. The most conservative result comes from the free amplitude with $\tau \geq 10$Gyrs. The best fit values with its contours are shown in the appendix, since they are not that interesting compared to the more robust excluded regions. They show a similar behavior though.
Overall, these cases show nicely the convergence of the exclusion regions towards larger τ values. The strong suppression for small τ values can't be at least partially artificially absorbed anymore and is therefore excluded.

6.4 Results

The final result of our analysis can be seen in Figure 6.20. This shows first of all, the $\Delta\chi^2$ values with the exclusion bounds for a confidence interval of 68% and 95% marked by a solid black line and dashed black line, respectively. Also, we use of course the 1-loop case since this is needed to account for the non-linearities. Mind, that we switched the x axis from τ to $\log_{10}(\Gamma/Gyrs^{-1})$ to better compare to other results in a moment. Secondly, we see the excluded region for an amplitude restriction in gray. We chose the 10% prior here, meaning a stronger value than for the original case but still not the most restrictive one. Thus, it is still on the conservative side and pretty stable. We see, that we successfully can exclude more of the high ϵ region, which is still allowed in the original fit. All ϵ values with approximately $\epsilon \gtrsim 0.001$ are then excluded for a lifetime of $\tau \lesssim 18$Gyrs. For larger lifetimes, our fit doesn't restrain the ϵ value anymore, whereas for lower lifetimes only $\epsilon < 0.001$ values are still allowed. This is expected, as the model converges towards ΛCDM at this point.
Additionally, we plotted our strongest approximated exclusion from PLANCK (dashed) and BAO (dotted) data in red. Since these are not exclusions relying on an in-depth analysis, they should mostly serve as an indicator of what parameter space is expected to be further constrained.
We can compare this however to an in-depth analysis – namely the PLANCK likelihood analysis, they have done in reference [16] which we show in Figure 6.19 on the left. Here, they compare the full (red) and lite (blue) likelihood MCMC analysis of PLANCK data. Mind, that they are going towards even larger lifetimes and also a bit smaller lifetimes, so we can only compare the plot for $0 \geq \log_{10}(\Gamma/Gyrs^{-1}) \gtrsim -2$. In this regime, even at $\tau = 80$Gyrs, almost all

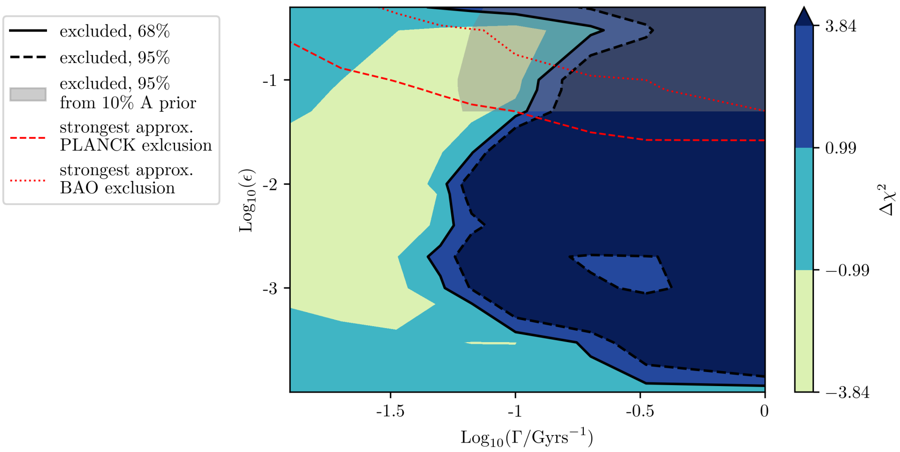

Figure 6.18: Results for the 1-loop original fit and the indicated exclusion region from a restricted amplitude with 10% prior. The excluded regions we get from PLANCK and BAO data when using the strongest approximation are shown in red, indicating their general behavior.

$\epsilon \gtrsim 10^{-2}$ are excluded. Even with the strongest bounds from our background analysis, we don't reach these values which is not surprising because we are only considering the TT-CMB spectrum. Still, we preserve a similar shape of the exclusion bound validating our general approach.

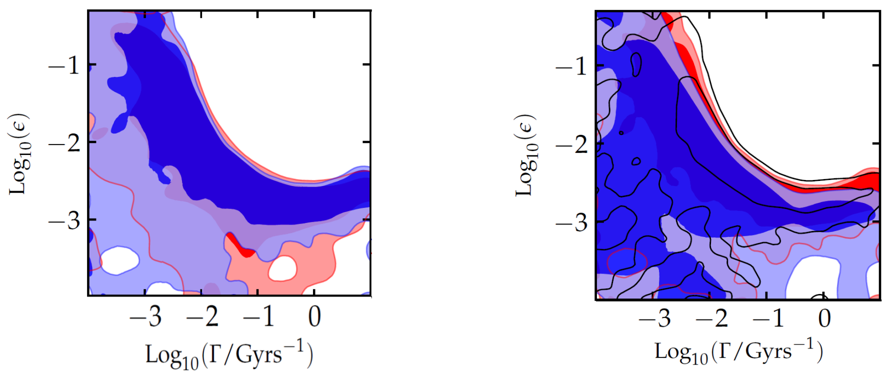

(a) Planck-likelihood analysis taken from [16]. The full one is described in red, the lite one in blue

(b) The posterior distributions from imposing three different S_8 priors from weak lensing measurements, taken from [16].

Figure 6.19: Results of the in-depth analysis in [16] which we use here only for comparison.

Other studies of DCDM usually all do an MCMC with CMB and BAO data. Therefore, it is not surprising, that we have less constraints on the small τ and large ϵ regimes compared to other results. Combining a full analysis with our

fit should hence result in much stronger bounds.
In Figure 6.20, we show the same plot but with indicated σ_8 values replacing the PLANCK and BAO exclusion. They were computed by CLASS with our linear spectra. The dashed line corresponds here to the PLANCK result of $\sigma_8 = 0.8111 \pm 0.0060$ [3]. Our computed values are slightly larger when converging towards ΛCDM with $\sigma_8 = 0.82$, so the dashed line divides the lower ϵ regime. The dash-dotted and dotted line belong to a value of $\sigma_8 = 0.7$ and $\sigma_8 = 0.6$, respectively. Small lifetimes and larger ϵ values lead again to the largest decrease, since their suppression is very strong in the $0.1 - 1$h/Mpc region. Disallowing too large deviations of σ_8 would hereby constrain a similar region compared to Planck data. We also note, that our model itself would allow a lot of σ_8 deviations towards lower values.
When using the exclusion contours from the Planck likelihood, a small regime with lowered σ_8 data is still allowed. It is located at around $\tau = 50 - 80$Gyrs and $0.004 \lesssim \epsilon \lesssim 0.01$ which fits relatively well to the best fit parameters of [35] at $\tau = 55$Gyrs and $\epsilon = 0.007$. While this is of course good news, we still have to admit that our model doesn't really provide much for this value, because it is mainly constructed by the σ_8 lines and the transferred Planck exclusion. It is not in contradiction though either, so BOSS data allows for such lower σ_8 values at regions that are preferred in other analyses.

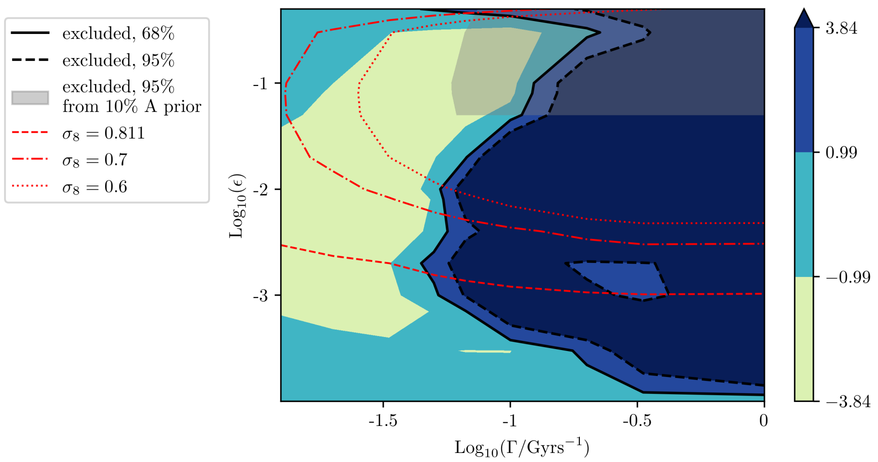

Figure 6.20: Results for the 1-loop original fit with the indicated exclusion region from a restricted amplitude with 10% prior. A few values of σ_8 are marked by red lines, with the dashed line corresponding to the PLANCK result.

We can also compare our result directly to the ones from [16] on the right. Here, they apply different S_8 priors that rely on different weak lensing datasets with the lowest one in black and the largest one in blue. The biggest difference is that their results allow for approximated ϵ values in the $0.001 - 0.005$ regime up to the lowest lifetimes, while ours actually exclude them. This effect can probably be accounted to our 1-loop corrections. In the latest paper from the same authors as before [30], they also include a treatment of the non-linear scales. They observe that due to this, lower lifetimes are more strongly excluded and the degeneracy between τ and ϵ is decreasing. This is exactly, what we observe when comparing our linear and 1-loop case, which confirms further the important effects of non-linearities.

Overall, we can observe several properties of our method: First of all, it produces bounds that rely on a conservative modeling of the flux power spectra and should thus be very robust.
Secondly, our method is not really suited for finding sensible best fit values. When doing fit variations, their position can change significantly and are not really stable. Thus, the preserved exclusion bounds are here of the most importance.
Thirdly, the inclusion of the 1-loop corrections changes the final result heavily and we are able to filter more of the smaller lifetimes almost independently of the ϵ parameter. This is a similar observation to the one in [30], where they experience likewise effects when including non-linearities even though they look at different data sets. This strengthens the importance of going beyond linear effects.
Fourthly, regarding the fact that our model uses only one kind of data set, our results are still promising. When including CMB data in a more professional manner, we would expect to get similar exclusion bounds as in other works, while being even slightly more constrictive in the lower τ regime.
Last but not least, we want to add, that our model tests data on larger redshifts compared to most other works with $z \lesssim 1$. Thus, it not only probes a different data set, it also provides an independent result to other studies. The fact, that no contradictions but even similarities are found, gives our approach even more validation. The additional ability to more strongly constrain part of the parameter space for smaller τ, also shows our models success.

7 | Summary and Conclusion

In this work, we have studied a decaying dark matter model, where cold dark matter decays into dark radiation and warm dark matter, by comparing to Lyman-α BOSS data at $z = 3.0 - 4.2$. We modeled the observed flux power spectrum with overall 6 free parameters. This method is overall more on the conservative side since it doesn't use much assumptions, especially on the IGM. We adjusted for non-linearities in our power spectra via cosmological perturbation theory by considering 1-loop corrections. We find, that their inclusion already leads to a large difference in the fits compared to a linear treatment. Higher loops can of course be applied for an even better description, but the main effect is already captured for the first order. We therefore wouldn't expect strong changes in the fit behavior even for higher loops. The fitting model was then first applied to ΛCDM and found that 1-loop corrections improve the fit significantly. We then applied it to at first a WDM model to test our method. We found mass constraints ranging from more conservative to tighter values and are not too far away from constraints derived by simulations when comparing our strongest bound.

Then, we finally turned towards DCDM. We first looked at its background evolution and find that it can already strongly exclude the small τ and large ϵ regimes when applying an in-depth analysis. Applying the fit, we find an exclusion region around $\tau \gtrsim 18$Gyrs, and smaller lifetimes only allowed for the lowest ϵ values, where it converges towards ΛCDM. Large ϵ values are also less tightly constrained. However, we found that when dealing with degeneracies in the amplitude, they can be excluded much better and we arrive at sensible values between 20 and 30 Gyrs.
When looking at σ_8, we see that our result still allows for smaller values that were preferred in other works, which is promising regarding the σ_8 tension. Comparing our overall constraints, we derive much weaker bounds for the small τ and large ϵ regime. This is expected, since we are not applying a full MCMC analysis with Planck data. However, our method is able to provide stronger constraints for the lifetime in the $\epsilon \sim 0.001 - 0.005$ regime when comparing to e.g. [16]. This can be mostly attributed to our treatment of non-linearities. Overall, our approach seems quite successful.

Currently, it seems that DCDM can still provide an explanation for the σ_8 tension. However, it is at the moment not preferred over ΛCDM. Upcoming high precision surveys like Euclid, DESI and Rubin/LSST will probably help in further constraining or preferring the model. If DCDM will not be able to solve the σ_8 tension but is not excluded, more complex models that introduce new aspects like e.g interactions to it could be interesting to study. In conclusion, we can only be curios for the next years and the future of DCDM.

A | The Fluid Approximation and modified CLASS Code

To generate our DCDM spectra, we make use of the very helpful modified CLASS code that was developed in [16] which we want to summarize here shortly. They give us two possibilities for the computation, namely an hierarchical method or their new fluid approximation.
Generally, the phase-space distribution is split into its background part and the perturbation part, so $f = \bar{f} + \Delta f$. The perturbation is then normally expanded in Legendre Polynomials with

$$\Delta f = \sum_{l=0}^{\infty} (-i)^l (2l+1) \Delta f_l P_l \tag{A.1}$$

and applied to the Boltzmann equations. This results in an hierarchical series of differential equations for the different moments f_l. In the case of dark radiation, we have $E = q$ which enables one to simplify these expressions by integrating over the momentum with $F_{dr,l} \propto \int_0^\infty \mathrm{d}q 4\pi q^2 q \Delta f_{dr,l}$. The new series of equations for F_{dr_l} is then not q dependent anymore and is much easier to solve.
For the warm dark matter, this simplification doesn't apply since its energy differs to its momentum. Its momentum dependence requires in turn a computation of the full phase space distribution which is computationally very expensive. Therefore, [16] removes this q dependency for WDM by treating it as a viscous fluid. In that case, they introduce a sound speed c_s for WDM and can describe it with the new continuity and Euler equations

$$\dot{\delta}_{wdm} = -3\mathcal{H}(c_s^2 - \omega)\delta_{wdm} - (1+\omega)\left(\theta_{wdm} + \frac{\dot{h}}{2}\right) \tag{A.2}$$

$$+ (1-\epsilon)a\Gamma \frac{\bar{\rho}_{dcdm}}{\bar{\rho}_{wdm}}(\delta_{dcdm} - \delta_{wdm}) \quad \text{and} \tag{A.3}$$

$$\dot{\theta}_{wdm} = -\mathcal{H}(1-3c_g^2)\theta_{wdm} + \frac{c_s^2}{1+\omega}k^2\delta_{wdm} - k^2\sigma_{wdm} \tag{A.4}$$

$$-(1-\epsilon)a\Gamma \frac{1+c_g^2}{1+\omega}\frac{\bar{\rho}_{dcdm}}{\bar{\rho}_{wdm}}\theta_{wdm}, \tag{A.5}$$

where we have $c_s = \delta P_{wdm}/\delta\rho_{wdm}$ and the adiabatic soundspeed $c_g = \dot{\bar{P}}_{wdm}/\dot{\bar{\rho}}_{wdm}$. This makes it possible to only consider the first two multipoles which is of course much faster. For this to be valid, the high and low l mulitpoles need to be effectively decoupled which is the case for scales deeply inside the Hubble radius.

Ultimately, we decided to use the fluid approximation based on its behavior compared to the hierarchical method. In Figure A.1 both are plotted normalized to the ΛCDM spectrum and for $\epsilon = 0.1$ and $\tau = 10$Gyrs. The short oscillations on the left, indicate where the fluid approximation is switched on. The hierarchical spectrum is very shaky which could be problematic for the fit while not adding new physical attributes to it. The fluid approximation however, is perfectly smooth and describes the hierarchical method well.

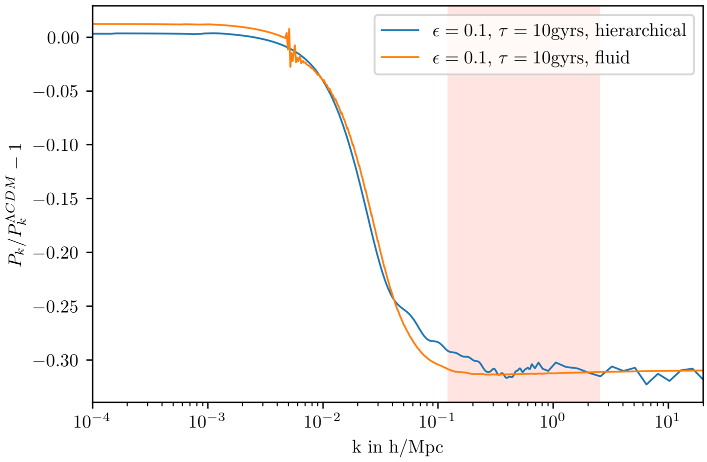

Figure A.1: Comparison between the normalized hierarchical and the fluid spectrum for $\epsilon = 0.1$ and $\tau = 10$Gyrs for the relevant scales.

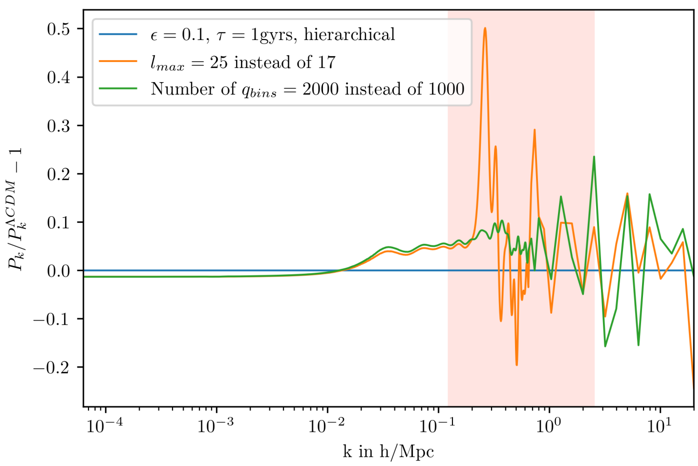

Figure A.2: Dependency of the hierarchical spectrum on the precision parameters for $\epsilon = 0.1$ and $\tau = 10$Gyrs.

Additionally, the hierarchical method relies strongly on the precision parameters l_{max} describing the highest multipole taken into account and the number of q_{bins} used. The default values used, are the same ones as recommended in [16] with

$l_{max} = 17$ and N$q_{bins} = 1000$. In Figure A.2, we compare the hierarchical spectrum with the default values to the one with larger precision parameters. It is normalized to the default spectrum.
The spectrum exhibits large deviations for the relevant scales and is dependent on the used parameters. Thus, we decided that the fluid approximation is overall better suited for our work. Not only does it run much faster and therefore allows for more parameters in ϵ and τ, it also provides a smoother spectrum being less error-prone when dealing with it.

B | Some Details for DCDM

B.1 Background Dynamics

B.1.1 Boltzmann Equations for DCDM

Here, we give the detailed derivation for equations 2.9. We start with DCDM and its Boltzmann equation in 2.5. Multiplying by $\int_0^\infty \mathrm{d}q \frac{1}{a^4} 4\pi q^2$ and using $E_{dcdm} = m_{dcdm} a$ as well as relations 2.6, the left-hand-side can be written as:

$$
\begin{aligned}
&\int_0^\infty \mathrm{d}q \frac{1}{a^4} 4\pi q^2 m_{dcdm} a \dot{\bar{f}}_{dcdm} = \\
&\int_0^\infty \mathrm{d}q 4\pi q^2 \frac{\mathrm{d}}{\mathrm{d}\tau}\left(\frac{m_{dcdm} a}{a^4} \bar{f}_{dcdm}\right) - \left(\frac{\mathrm{d}}{\mathrm{d}\tau} \frac{m_{dcdm} a}{a^4}\right) \bar{f}_{dcdm} = \\
&\frac{\mathrm{d}}{\mathrm{d}\tau} \int_0^\infty \mathrm{d}q 4\pi q^2 \frac{m_{dcdm} a}{a^4} \bar{f}_{dcdm} + 3\frac{\dot{a}}{a} \int_0^\infty \mathrm{d}q 4\pi q^2 \frac{m_{dcdm} a}{a^4} \bar{f}_{dcdm} = \\
&\dot{\bar{\rho}}_{dcdm} + 3\mathcal{H} \bar{\rho}_{dcdm}
\end{aligned}
$$

In turn, the right-hand-side takes the form

$$
-\int_0^\infty \mathrm{d}q \frac{a\Gamma}{a^4} 4\pi q^2 m_{dcdm} a \dot{\bar{f}}_{dcdm} = -a\Gamma \bar{\rho}_{dcdm}
$$

resulting in the first equation in 2.9.
For DR, where $E_{dr} = q$, the left-hand-side takes the form

$$
\begin{aligned}
&\int_0^\infty \mathrm{d}q \frac{1}{a^4} 4\pi q^2 q \dot{\bar{f}}_{dr} = \\
&\int_0^\infty \mathrm{d}q 4\pi q^2 \frac{\mathrm{d}}{\mathrm{d}\tau}\left(\frac{q}{a^4} \bar{f}_{dr}\right) - \left(\frac{\mathrm{d}}{\mathrm{d}\tau} \frac{q}{a^4}\right) \bar{f}_{dr} = \\
&\dot{\bar{\rho}}_{dr} + 4\mathcal{H} \bar{\rho}_{dr}.
\end{aligned}
$$

For the right-hand-side we make use of the relation for $\bar{N}$ and get

$$
\begin{aligned}
&\int_0^\infty \mathrm{d}q \frac{1}{a^4} 4\pi q^2 \frac{a\Gamma}{4\pi q^2} \frac{\bar{\rho}_{dcdm} a^3}{m_{dcdm}} q \delta(q - a p_{max}) = \\
&a\Gamma \frac{\bar{\rho}_{dcdm}}{m_{dcdm} a} a \epsilon m_{dcdm} = \epsilon a \Gamma \bar{\rho}_{dcdm}.
\end{aligned}
$$

Similarly, for WDM with $E_{wdm} = \sqrt{m_{wdm}^2 a^2 + q^2}$, the right-hand-side ends with $\sqrt{m_{wdm}^2 a^2 + a^2 p_{max}^2} = a m_{dcdm} \sqrt{m_{wdm}^2 / m_{dcdm} 2 + \epsilon^2} = a m_{dcdm} (1 - \epsilon)$.

Thus, we have $(1-\epsilon)a\Gamma\bar{\rho}_{dcdm}$. The left-hand-side is given by

$$\int_0^\infty \mathrm{d}q \frac{1}{a^4} 4\pi q^2 \sqrt{m_{wdm}^2 a^2 + q^2}\,\dot{\bar{f}}_{wdm} =$$

$$\int_0^\infty \mathrm{d}q 4\pi q^2 \frac{\mathrm{d}}{\mathrm{d}\tau}\left(\frac{\sqrt{m_{wdm}^2 a^2 + q^2}}{a^4}\bar{f}_{wdm}\right) - \left(\frac{\mathrm{d}}{\mathrm{d}\tau}\frac{\sqrt{m_{wdm}^2 a^2 + q^2}}{a^4}\right)\bar{f}_{wdm} =$$

$$\dot{\bar{\rho}}_{wdm} - \int_0^\infty \mathrm{d}q 4\pi q^2 \left(-4\frac{\sqrt{m_{wdm}^2 a^2 + q^2}}{a^4}\mathcal{H} + \frac{m_{wdm}^2 a^2}{a^4\sqrt{m_{wdm}^2 a^2 + q^2}}\mathcal{H}\right)\bar{f}_{wdm} =$$

$$\dot{\bar{\rho}}_{wdm} + 4\mathcal{H}\bar{\rho}_{wdm} - \int_0^\infty \mathrm{d}q 4\pi \frac{q^2}{a^4}\left(\sqrt{m_{wdm}^2 a^2 + q^2} - \frac{q^2}{\sqrt{m_{wdm}^2 a^2 + q^2}}\right)\mathcal{H}\bar{f}_{wdm} =$$

$$\dot{\bar{\rho}}_{wdm} + 4\mathcal{H}\bar{\rho}_{wdm} - \mathcal{H}\bar{\rho}_{wdm} + 3\mathcal{H}\bar{P}_{wdm}.$$

With the equation-of-state parameter $\omega = \bar{P}_{wdm}/\bar{\rho}_{wdm}$ the final equation is derived.

B.1.2 Own Implementation of Background Evolution

Solving the background evolution isn't completely straight forward since the densities depend on each other and can't be decoupled in time. To battle this problem, we first choose some starting values and then solve the system of equations in time steps.
The fixed parameters we will need are $H_0 = 67.7km/sMpc$ and $\rho_{\mathrm{crit},0} = 3H_0^2c^2/8\pi G$. Additionally, Ω_b for baryons, Ω_γ for photons and Ω_ν for neutrinos are fixed to typical ΛCDM values. At last, we choose $\omega_{dcdm}^{ini} = 0.12$, which describes the density DCDM would have today when not undergoing the decay. The only open parameter is Ω_Λ which runs through several possible values. The one that actually preserves our fixed H_0 is then chosen.
Now, we create a logarithmic range for the redshift with $10^{-4} \leq z \leq 10^4$. The starting point is at the largest redshifts, where the decay hasn't really set in. Thus, we choose as starting conditions $\omega_{wdm} = \omega_{dr} = 0$ and omit the exponential decay factor for DCDM. Our background quantities $\mathcal{H}$, t and ρ_{crit} are computed with the same starting values.
Then we are going through a number of steps in z. At first, we fix the new time parameter which is given by the old one plus the spent time between z_{old} and z_{new} which depends on the old densities. The new $\mathcal{H}$ is also computed with the old densities. Then, the densities are computed with the new background quantities. This method is of course not accurate, so we do this step a few times for each z-step to make sure we get the best possible approximation of the actual values. Afterwards the critical density is computed, so we can actually plot $\Omega(z)$.
So overall, the code returns a list of z, t, $\mathcal{H}$, ρ_{crit}, all individual densities and the total density parameter. Since we know the supposed value for the latter as well as $\mathcal{H}$ and thus ρ_{crit}, these quantities are checked to adjust Ω_Λ. In our case, there are 300 timesteps with 3 iterations each to get a sufficiently accurate result. Still, this code is certainly not efficient and precise enough to use for detailed analyses. However, we can still reproduce the background evolution quite well and it helped to gain a deeper understanding of the underlying dynamics.

B.1.3 Detailed Tables for H_0 and Ω_Λ

$\epsilon \backslash \tau$	1.00	3.00	5.00	10.00	15.00	20.00	30.00	50.00	80.00
0.0001	67.71	67.70	67.69	67.69	67.69	67.69	67.69	67.69	67.70
0.0003	67.71	67.70	67.70	67.69	67.69	67.69	67.69	67.69	67.70
0.0007	67.73	67.71	67.70	67.69	67.69	67.69	67.69	67.69	67.70
0.001	67.74	67.72	67.71	67.69	67.69	67.69	67.69	67.69	67.70
0.002	67.78	67.74	67.72	67.70	67.70	67.69	67.69	67.70	67.70
0.004	67.86	67.78	67.75	67.72	67.71	67.70	67.70	67.70	67.70
0.008	68.02	67.87	67.81	67.75	67.73	67.72	67.71	67.71	67.70
0.01	68.10	67.91	67.83	67.76	67.74	67.73	67.72	67.71	67.71
0.02	68.50	68.12	67.98	67.84	67.79	67.77	67.74	67.73	67.72
0.05	69.75	68.78	68.42	68.09	67.96	67.89	67.83	67.78	67.75
0.08	71.07	69.47	68.89	68.34	68.14	68.03	67.92	67.83	67.78
0.1	71.99	69.96	69.21	68.51	68.25	68.11	67.97	67.86	67.80
0.3	83.92	76.07	73.33	70.76	69.79	69.28	68.76	68.34	68.10
0.5	114.10	89.92	82.37	75.57	73.06	71.75	70.42	69.34	68.73

Table B.1: H_0 in km/sMpc for all parameter combinations ϵ and τ in Gyrs.

$\epsilon \backslash \tau$	1.00	3.00	5.00	10.00	15.00	20.00	30.00	50.00	80.00
0.0001	0.69	0.69	0.69	0.69	0.69	0.69	0.69	0.69	0.69
0.0003	0.69	0.69	0.69	0.69	0.69	0.69	0.69	0.69	0.69
0.0007	0.69	0.69	0.69	0.69	0.69	0.69	0.69	0.69	0.69
0.001	0.69	0.69	0.69	0.69	0.69	0.69	0.69	0.69	0.69
0.002	0.69	0.69	0.69	0.69	0.69	0.69	0.69	0.69	0.69
0.004	0.69	0.69	0.69	0.69	0.69	0.69	0.69	0.69	0.69
0.008	0.70	0.69	0.69	0.69	0.69	0.69	0.69	0.69	0.69
0.01	0.70	0.69	0.69	0.69	0.69	0.69	0.69	0.69	0.69
0.02	0.70	0.70	0.70	0.69	0.69	0.69	0.69	0.69	0.69
0.05	0.72	0.71	0.71	0.70	0.70	0.70	0.69	0.69	0.69
0.08	0.74	0.72	0.71	0.71	0.70	0.70	0.70	0.69	0.69
0.1	0.75	0.73	0.72	0.71	0.70	0.70	0.70	0.69	0.69
0.3	0.85	0.81	0.79	0.75	0.74	0.73	0.72	0.71	0.70
0.5	0.97	0.93	0.90	0.84	0.80	0.78	0.76	0.73	0.72

Table B.2: Ω_Λ for all parameter combinations ϵ and τ in Gyrs.

B.2 Fits

B.2.1 Best Fit Values for β_b and β_{ct} priors

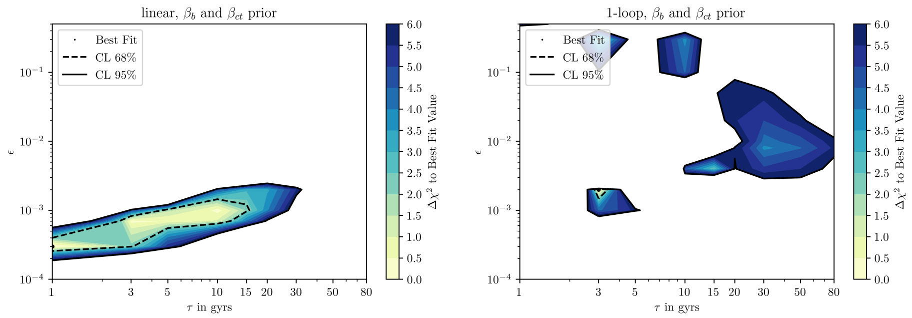

Figure B.1: Contours around the best fit DCDM value, marked by a black dot, in the 2d parameter space and with priors for β_b and β_{ct}. The solid and dashed black lines indicate the 95% and 68% confidence intervals. The linear fit is on the left, the 1-loop fit on the right.

Here, we show the best fit contours for the β_b and β_{ct} prior in Figure B.1. The best fit values are at $\tau_{\text{bestfit}} = 1$Gyrs, $\epsilon_{\text{bestfit}} = 0.0003$ with $\chi^2 = 199.00$ in the linear case, and at $\tau_{\text{bestfit}} = 3$Gyrs, $\epsilon_{\text{bestfit}} = 0.002$ with $\chi^2 = 194.60$ in the 1-loop case. The linear case doesn't really differentiate from the original fit. The 1-loop case though, only encompasses the patches we have seen before. Therefore, the best fit values are not of much use and are mostly added for completion. The important attribute is the exclusion shape which is still preserved.

B.2.2 Best Fit Values for the restricted Amplitude

Here, we show the best fit values for the restricted amplitude cases in Figure B.2. The parameter space is smaller and only includes $\epsilon \geq 0.05$ In the linear case, the best fit values are at $\tau_{\text{bestfit}} = 10$Gyrs, $\epsilon_{\text{bestfit}} = 0.3$ with $\chi^2 = 205.89$ for the 5% prior, at $\tau_{\text{bestfit}} = 10$Gyrs, $\epsilon_{\text{bestfit}} = 0.3$ with $\chi^2 = 205.94$ for the 10% prior and at $\tau_{\text{bestfit}} = 50$Gyrs, $\epsilon_{\text{bestfit}} = 0.08$ with $\chi^2 = 206.15$ for the fixed amplitude.
In the 1-loop case, we have values of $\tau_{\text{bestfit}} = 50$Gyrs, $\epsilon_{\text{bestfit}} = 0.05$ for the 5% prior with $\chi^2 = 192.23$, $\tau_{\text{bestfit}} = 30$Gyrs, $\epsilon_{\text{bestfit}} = 0.05$ with $\chi^2 = 191.77$ for the 10% prior and $\tau_{\text{bestfit}} = 80$Gyrs, $\epsilon_{\text{bestfit}} = 0.5$ with $\chi^2 = 195.37$ for the fixed amplitude.
Since the differences in the allowed regions are relatively small, these values aren't of that much importance and are again only shown here for completion. The excluded parameter space shows the same behavior as before and is therefore very robust.

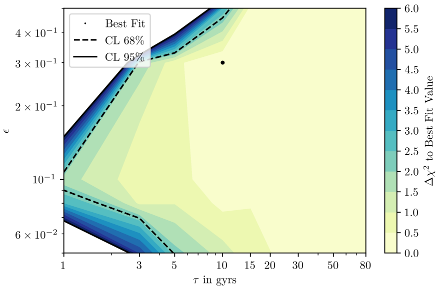

(a) linear, A prior at 10%

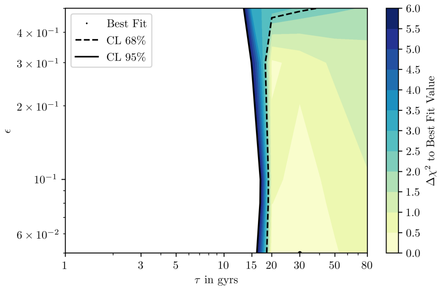

(b) 1-loop, A prior at 10%

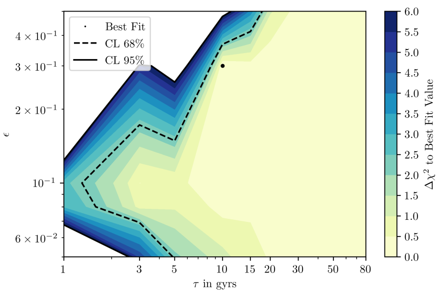

(c) linear, A prior at 5%

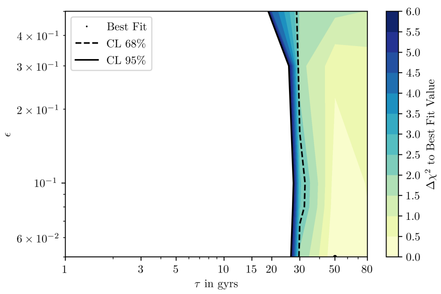

(d) 1-loop, A prior at 5%

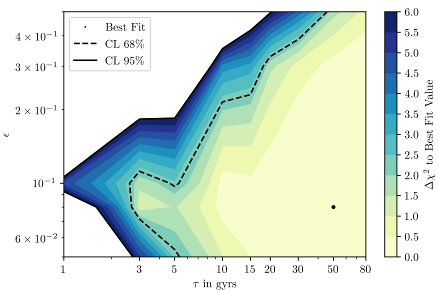

(e) linear, fixed amplitude

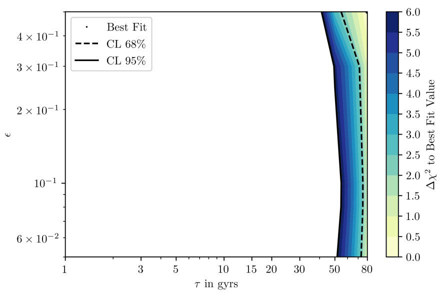

(f) 1-loop, fixed amplitude

Figure B.2: Contours around the best fit DCDM value, marked by a black dot, in the 2d parameter space and with different levels of amplitude restriction. The left side shows the linear plots, the right one the 1-loop plots. The solid and dashed black lines indicate the 95% and 68% confidence intervals.

Bibliography

[1] Elcio Abdalla et al. "Cosmology Intertwined: A Review of the Particle Physics, Astrophysics, and Cosmology Associated with the Cosmological Tensions and Anomalies". In: *2022 Snowmass Summer Study*. Mar. 2022. arXiv: 2203.06142 [astro-ph.CO].

[2] Nils Schöneberg et al. "The H_0 Olympics: A fair ranking of proposed models". In: (July 2021). arXiv: 2107.10291 [astro-ph.CO].

[3] N. Aghanim et al. "Planck 2018 results. VI. Cosmological parameters". In: *Astron. Astrophys.* 641 (2020). [Erratum: Astron.Astrophys. 652, C4 (2021)], A6. DOI: 10.1051/0004-6361/201833910. arXiv: 1807.06209 [astro-ph.CO].

[4] Nils Schöneberg, Julien Lesgourgues, and Deanna C. Hooper. "The BAO+BBN take on the Hubble tension". In: *JCAP* 10 (2019), p. 029. DOI: 10.1088/1475-7516/2019/10/029. arXiv: 1907.11594 [astro-ph.CO].

[5] L. Verde, T. Treu, and A. G. Riess. "Tensions between the Early and the Late Universe". In: *Nature Astron.* 3 (July 2019), p. 891. DOI: 10.1038/s41550-019-0902-0. arXiv: 1907.10625 [astro-ph.CO].

[6] Adam G. Riess et al. "A Comprehensive Measurement of the Local Value of the Hubble Constant with 1 km/s/Mpc Uncertainty from the Hubble Space Telescope and the SH0ES Team". In: (Dec. 2021). arXiv: 2112.04510 [astro-ph.CO].

[7] Eleonora Di Valentino et al. "In the realm of the Hubble tension—a review of solutions". In: *Class. Quant. Grav.* 38.15 (2021), p. 153001. DOI: 10.1088/1361-6382/ac086d. arXiv: 2103.01183 [astro-ph.CO].

[8] Eleonora Di Valentino et al. "Cosmology intertwined III: $f\sigma_8$ and S_8". In: *Astropart. Phys.* 131 (2021), p. 102604. DOI: 10.1016/j.astropartphys.2021.102604. arXiv: 2008.11285 [astro-ph.CO].

[9] Simone Aiola et al. "The Atacama Cosmology Telescope: DR4 Maps and Cosmological Parameters". In: *JCAP* 12 (2020), p. 047. DOI: 10.1088/1475-7516/2020/12/047. arXiv: 2007.07288 [astro-ph.CO].

[10] Marika Asgari et al. "KiDS-1000 Cosmology: Cosmic shear constraints and comparison between two point statistics". In: *Astron. Astrophys.* 645 (2021), A104. DOI: 10.1051/0004-6361/202039070. arXiv: 2007.15633 [astro-ph.CO].

[11] Chiaki Hikage et al. “Cosmology from cosmic shear power spectra with Subaru Hyper Suprime-Cam first-year data”. In: *Publ. Astron. Soc. Jap.* 71.2 (2019), p. 43. DOI: 10.1093/pasj/psz010. arXiv: 1809.09148 [astro-ph.CO].

[12] T. M. C. Abbott et al. “Dark Energy Survey Year 3 results: Cosmological constraints from galaxy clustering and weak lensing”. In: *Phys. Rev. D* 105.2 (2022), p. 023520. DOI: 10.1103/PhysRevD.105.023520. arXiv: 2105.13549 [astro-ph.CO].

[13] Eleonora Di Valentino et al. “Interacting dark energy in the early 2020s: A promising solution to the H_0 and cosmic shear tensions”. In: *Phys. Dark Univ.* 30 (2020), p. 100666. DOI: 10.1016/j.dark.2020.100666. arXiv: 1908.04281 [astro-ph.CO].

[14] Richard A. Battye and Adam Moss. “Evidence for Massive Neutrinos from Cosmic Microwave Background and Lensing Observations”. In: *Phys. Rev. Lett.* 112.5 (2014), p. 051303. DOI: 10.1103/PhysRevLett.112.051303. arXiv: 1308.5870 [astro-ph.CO].

[15] Stefan Heimersheim et al. “Cannibalism hinders growth: Cannibal Dark Matter and the S_8 tension”. In: *JCAP* 12 (2020), p. 016. DOI: 10.1088/1475-7516/2020/12/016. arXiv: 2008.08486 [astro-ph.CO].

[16] Guillermo F. Abellán, Riccardo Murgia, and Vivian Poulin. “Linear cosmological constraints on two-body decaying dark matter scenarios and the S_8 tension”. In: *prd* 104.12, 123533 (Dec. 2021), p. 123533. DOI: 10.1103/PhysRevD.104.123533. arXiv: 2102.12498 [astro-ph.CO].

[17] James S. Bullock and Michael Boylan-Kolchin. “Small-Scale Challenges to the ΛCDM Paradigm”. In: *Ann. Rev. Astron. Astrophys.* 55 (2017), pp. 343–387. DOI: 10.1146/annurev-astro-091916-055313. arXiv: 1707.04256 [astro-ph.CO].

[18] W. J. G. de Blok. “The Core-Cusp Problem”. In: *Adv. Astron.* 2010 (2010), p. 789293. DOI: 10.1155/2010/789293. arXiv: 0910.3538 [astro-ph.CO].

[19] Michael Kuhlen, Mark Vogelsberger, and Raul Angulo. “Numerical Simulations of the Dark Universe: State of the Art and the Next Decade”. In: *Phys. Dark Univ.* 1 (2012), pp. 50–93. DOI: 10.1016/j.dark.2012.10.002. arXiv: 1209.5745 [astro-ph.CO].

[20] Mihai Tomozeiu, Lucio Mayer, and Thomas Quinn. “TIDAL STIRRING OF SATELLITES WITH SHALLOW DENSITY PROFILES PREVENTS THEM FROM BEING TOO BIG TO FAIL”. In: *The Astrophysical Journal* 827.1 (2016), p. L15. DOI: 10.3847/2041-8205/827/1/l15. URL: https://doi.org/10.3847/2041-8205/827/1/l15.

[21] Keith Bechtol et al. “Snowmass2021 Cosmic Frontier White Paper: Dark Matter Physics from Halo Measurements”. In: *2022 Snowmass Summer Study*. Mar. 2022. arXiv: 2203.07354 [hep-ph].

[22] David N. Spergel and Paul J. Steinhardt. “Observational Evidence for Self-Interacting Cold Dark Matter”. In: *Phys. Rev. Lett.* 84 (17 2000), pp. 3760–3763. DOI: 10.1103/PhysRevLett.84.3760. URL: https://link.aps.org/doi/10.1103/PhysRevLett.84.3760.

[23] Eric D. Carlson, Marie E. Machacek, and Lawrence J. Hall. "Self-interacting Dark Matter". In: *apj* 398 (Oct. 1992), p. 43. DOI: 10.1086/171833.

[24] Benjamin Audren et al. "Strongest model-independent bound on the lifetime of Dark Matter". In: *JCAP* 12 (2014), p. 028. DOI: 10.1088/1475-7516/2014/12/028. arXiv: 1407.2418 [astro-ph.CO].

[25] Shohei Aoyama et al. "Evolution of perturbations and cosmological constraints in decaying dark matter models with arbitrary decay mass products". In: *JCAP* 07 (2014), p. 021. DOI: 10.1088/1475-7516/2014/07/021. arXiv: 1402.2972 [astro-ph.CO].

[26] Gordon Blackadder and Savvas M. Koushiappas. "Dark matter with two- and many-body decays and supernovae type Ia". In: *Phys. Rev. D* 90.10 (2014), p. 103527. DOI: 10.1103/PhysRevD.90.103527. arXiv: 1410.0683 [astro-ph.CO].

[27] Kari Enqvist et al. "Decaying dark matter and the tension in σ_8". In: *JCAP* 09 (2015), p. 067. DOI: 10.1088/1475-7516/2015/09/067. arXiv: 1505.05511 [astro-ph.CO].

[28] Vivian Poulin, Pasquale D. Serpico, and Julien Lesgourgues. "A fresh look at linear cosmological constraints on a decaying dark matter component". In: *JCAP* 08 (2016), p. 036. DOI: 10.1088/1475-7516/2016/08/036. arXiv: 1606.02073 [astro-ph.CO].

[29] Andreas Nygaard, Thomas Tram, and Steen Hannestad. "Updated constraints on decaying cold dark matter". In: *JCAP* 05 (2021), p. 017. DOI: 10.1088/1475-7516/2021/05/017. arXiv: 2011.01632 [astro-ph.CO].

[30] Théo Simon et al. "Constraining decaying dark matter with BOSS data and the effective field theory of large-scale structures". In: (Mar. 2022). arXiv: 2203.07440 [astro-ph.CO].

[31] Luis A. Anchordoqui et al. "Decay of multiple dark matter particles to dark radiation in different epochs does not alleviate the Hubble tension". In: (Mar. 2022). arXiv: 2203.04818 [astro-ph.CO].

[32] Balakrishna S. Haridasu and Matteo Viel. "Late-time decaying dark matter: constraints and implications for the H_0-tension". In: *Mon. Not. Roy. Astron. Soc.* 497.2 (2020), pp. 1757–1764. DOI: 10.1093/mnras/staa1991. arXiv: 2004.07709 [astro-ph.CO].

[33] Steven J. Clark, Kyriakos Vattis, and Savvas M. Koushiappas. "Cosmological constraints on late-universe decaying dark matter as a solution to the H_0 tension". In: *Phys. Rev. D* 103.4 (2021), p. 043014. DOI: 10.1103/PhysRevD.103.043014. arXiv: 2006.03678 [astro-ph.CO].

[34] Zahra Davari and Nima Khosravi. "Can decaying dark matter scenarios alleviate both H_0 and σ_8 tensions?" In: (Mar. 2022). arXiv: 2203.09439 [astro-ph.CO].

[35] Guillermo Franco Abellán et al. "Implications of the S_8 tension for decaying dark matter with warm decay products". In: *Phys. Rev. D* 105.6 (2022), p. 063525. DOI: 10.1103/PhysRevD.105.063525. arXiv: 2008.09615 [astro-ph.CO].

[36] Renyue Cen. "Decaying cold dark matter model and small-scale power". In: *Astrophys. J. Lett.* 546 (2001), pp. L77–L80. DOI: 10.1086/318861. arXiv: astro-ph/0005206.

[37] Annika H. G. Peter and Andrew J. Benson. "Dark-matter decays and Milky Way satellite galaxies". In: *Phys. Rev. D* 82 (2010), p. 123521. DOI: 10.1103/PhysRevD.82.123521. arXiv: 1009.1912 [astro-ph.GA].

[38] S. Mau et al. "Milky Way Satellite Census. IV. Constraints on Decaying Dark Matter from Observations of Milky Way Satellite Galaxies". In: (Jan. 2022). arXiv: 2201.11740 [astro-ph.CO].

[39] Mei-Yu Wang and Andrew R. Zentner. "Effects of Unstable Dark Matter on Large-Scale Structure and Constraints from Future Surveys". In: *Phys. Rev. D* 85 (2012), p. 043514. DOI: 10.1103/PhysRevD.85.043514. arXiv: 1201.2426 [astro-ph.CO].

[40] Rachel Mandelbaum et al. "The LSST Dark Energy Science Collaboration (DESC) Science Requirements Document". In: (Sept. 2018). arXiv: 1809.01669 [astro-ph.CO].

[41] LSST Science Collaboration et al. *LSST Science Book, Version 2.0*. 2009. DOI: 10.48550/ARXIV.0912.0201. URL: https://arxiv.org/abs/0912.0201.

[42] Amir Aghamousa et al. "The DESI Experiment Part I: Science,Targeting, and Survey Design". In: (Oct. 2016). arXiv: 1611.00036 [astro-ph.IM].

[43] Luca Amendola et al. "Cosmology and fundamental physics with the Euclid satellite". In: *Living Reviews in Relativity* 21.1, 2 (Apr. 2018), p. 2. DOI: 10.1007/s41114-017-0010-3. arXiv: 1606.00180 [astro-ph.CO].

[44] David H. Weinberg et al. "The Lyman - alpha forest as a cosmological tool". In: *AIP Conf. Proc.* 666.1 (2003). Ed. by Jacques Dumarchez, Yannick Giraud-Heraud, and Jean Tran Thanh Van, pp. 157–169. DOI: 10.1063/1.1581786. arXiv: astro-ph/0301186.

[45] Michael Rauch. "The lyman alpha forest in the spectra of quasistellar objects". In: *Ann. Rev. Astron. Astrophys.* 36 (1998), pp. 267–316. DOI: 10.1146/annurev.astro.36.1.267. arXiv: astro-ph/9806286.

[46] Solène Chabanier et al. "The one-dimensional power spectrum from the SDSS DR14 Lyα forests". In: *JCAP* 07 (2019), p. 017. DOI: 10.1088/1475-7516/2019/07/017. arXiv: 1812.03554 [astro-ph.CO].

[47] Isabelle Pâris et al. "The Sloan Digital Sky Survey Quasar Catalog: Fourteenth data release". In: *aap* 613, A51 (May 2018), A51. DOI: 10.1051/0004-6361/201732445. arXiv: 1712.05029 [astro-ph.GA].

[48] S. S. Vogt et al. "HIRES: the high-resolution echelle spectrometer on the Keck 10-m Telescope". In: *Proc. SPIE Int. Soc. Opt. Eng.* 2198 (1994), p. 362. DOI: 10.1117/12.176725.

[49] Matteo Viel, Martin G. Haehnelt, and Volker Springel. "Inferring the dark matter power spectrum from the Lyman α forest in high-resolution QSO absorption spectra". In: *Monthly Notices of the Royal Astronomical Society* 354.3 (Nov. 2004), pp. 684–694. ISSN: 0035-8711. DOI: 10.1111/j.1365-2966.2004.08224.x. eprint: https://academic.oup.com/mnras/article-pdf/354/3/684/18653214/354-3-684.pdf. URL: https://doi.org/10.1111/j.1365-2966.2004.08224.x.

[50] N. Kaiser and J. A. Peacock. "Power-Spectrum Analysis of One-dimensional Redshift Surveys". In: *apj* 379 (Oct. 1991), p. 482. DOI: 10.1086/170523.

[51] Andreu Arinyo i Prats et al. "The Non-Linear Power Spectrum of the Lyman Alpha Forest". In: *Journal of Cosmology and Astroparticle Physics* 2015 (June 2015). DOI: 10.1088/1475-7516/2015/12/017.

[52] Nathalie Palanque-Delabrouille et al. "The one-dimensional Ly-alpha forest power spectrum from BOSS". In: *Astron. Astrophys.* 559 (2013), A85. DOI: 10.1051/0004-6361/201322130. arXiv: 1306.5896 [astro-ph.CO].

[53] Christopher P. Ahn et al. "THE NINTH DATA RELEASE OF THE SLOAN DIGITAL SKY SURVEY: FIRST SPECTROSCOPIC DATA FROM THE SDSS-III BARYON OSCILLATION SPECTROSCOPIC SURVEY". In: *The Astrophysical Journal Supplement Series* 203.2 (Nov. 2012), p. 21. ISSN: 1538-4365. DOI: 10.1088/0067-0049/203/2/21. URL: http://dx.doi.org/10.1088/0067-0049/203/2/21.

[54] Mathias Garny et al. "Neutrino mass bounds from confronting an effective model with BOSS Lyman-α data". In: *JCAP* 03 (2021), p. 049. DOI: 10.1088/1475-7516/2021/03/049. arXiv: 2011.03050 [astro-ph.CO].

[55] Alexey Boyarsky et al. "Realistic sterile neutrino dark matter with keV mass does not contradict cosmological bounds". In: *Phys. Rev. Lett.* 102 (2009), p. 201304. DOI: 10.1103/PhysRevLett.102.201304. arXiv: 0812.3256 [hep-ph].

[56] Antonella Garzilli et al. "The Lyman-α forest as a diagnostic of the nature of the dark matter". In: *mnras* 489.3 (Nov. 2019), pp. 3456–3471. DOI: 10.1093/mnras/stz2188. arXiv: 1809.06585 [astro-ph.CO].

[57] Mathias Garny et al. "Lyman-α forest constraints on interacting dark sectors". In: *JCAP* 09 (2018), p. 011. DOI: 10.1088/1475-7516/2018/09/011. arXiv: 1805.12203 [astro-ph.CO].

[58] Ya. B. Zel'dovich. "Gravitational instability: An approximate theory for large density perturbations." In: *aap* 5 (Mar. 1970), pp. 84–89.

[59] Lam Hui and Nickolay Y. Gnedin. "Equation of state of the photoionized intergalactic medium". In: *Mon. Not. Roy. Astron. Soc.* 292 (1997), p. 27. DOI: 10.1093/mnras/292.1.27. arXiv: astro-ph/9612232.

[60] Nickolay Y. Gnedin and Lam Hui. "Probing the universe with the Lyman alpha forest: 1. Hydrodynamics of the low density IGM". In: *Mon. Not. Roy. Astron. Soc.* 296 (1998), pp. 44–55. DOI: 10.1046/j.1365-8711.1998.01249.x. arXiv: astro-ph/9706219.

[61] Roman Scoccimarro. "Redshift-space distortions, pairwise velocities and nonlinearities". In: *Phys. Rev. D* 70 (2004), p. 083007. DOI: 10.1103/PhysRevD.70.083007. arXiv: astro-ph/0407214.

[62] F. Bernardeau et al. “Large-scale structure of the Universe and cosmological perturbation theory”. In: *Physics Reports* 367.1 (2002), pp. 1–248. ISSN: 0370-1573. DOI: https://doi.org/10.1016/S0370-1573(02)00135-7. URL: https://www.sciencedirect.com/science/article/pii/S0370157302001357.

[63] Martin Crocce and Roman Scoccimarro. “Renormalized cosmological perturbation theory”. In: *Phys. Rev. D* 73 (2006), p. 063519. DOI: 10.1103/PhysRevD.73.063519. arXiv: astro-ph/0509418.

[64] Mathias Garny and Petter Taule. “Loop corrections to the power spectrum for massive neutrino cosmologies with full time- and scale-dependence”. In: *JCAP* 01 (2021), p. 020. DOI: 10.1088/1475-7516/2021/01/020. arXiv: 2008.00013 [astro-ph.CO].

[65] Diego Blas, Mathias Garny, and Thomas Konstandin. “Cosmological perturbation theory at three-loop order”. In: *JCAP* 01 (2014), p. 010. DOI: 10.1088/1475-7516/2014/01/010. arXiv: 1309.3308 [astro-ph.CO].

[66] Bhuvnesh Jain and Edmund Bertschinger. “Second-Order Power Spectrum and Nonlinear Evolution at High Redshift”. In: *apj* 431 (Aug. 1994), p. 495. DOI: 10.1086/174502. arXiv: astro-ph/9311070 [astro-ph].

[67] Diego Blas, Julien Lesgourgues, and Thomas Tram. “The Cosmic Linear Anisotropy Solving System (CLASS). Part II: Approximation schemes”. In: *Journal of Cosmology and Astroparticle Physics* 2011.07 (2011), 034–034. ISSN: 1475-7516. DOI: 10.1088/1475-7516/2011/07/034. URL: http://dx.doi.org/10.1088/1475-7516/2011/07/034.

[68] Julien Lesgourgues. “The Cosmic Linear Anisotropy Solving System (CLASS) I: Overview”. In: *arXiv e-prints*, arXiv:1104.2932 (Apr. 2011), arXiv:1104.2932. arXiv: 1104.2932 [astro-ph.IM].

[69] Joel R. Primack. “Cosmology: small-scale issues”. In: *New Journal of Physics* 11.10, 105029 (Oct. 2009), p. 105029. DOI: 10.1088/1367-2630/11/10/105029. arXiv: 0909.2247 [astro-ph.CO].

[70] Paul Bode, Jeremiah P. Ostriker, and Neil Turok. “Halo Formation in Warm Dark Matter Models”. In: *The Astrophysical Journal* 556.1 (2001), pp. 93–107. DOI: 10.1086/321541. URL: https://doi.org/10.1086/321541.

[71] Andrea V. Macciò et al. “Cores in warm dark matter haloes: a Catch 22 problem”. In: *mnras* 424.2 (Aug. 2012), pp. 1105–1112. DOI: 10.1111/j.1365-2966.2012.21284.x. arXiv: 1202.1282 [astro-ph.CO].

[72] Mark R. Lovell et al. “The properties of warm dark matter haloes”. In: *mnras* 439.1 (Mar. 2014), pp. 300–317. DOI: 10.1093/mnras/stt2431. arXiv: 1308.1399 [astro-ph.CO].

[73] Francisco Villaescusa-Navarro and Neal Dalal. “Cores and cusps in warm dark matter halos”. In: *Journal of Cosmology and Astroparticle Physics* 2011.03 (2011), pp. 024–024. DOI: 10.1088/1475-7516/2011/03/024. URL: https://doi.org/10.1088%2F1475-7516%2F2011%2F03%2F024.

[74] Pedro Colin, Vladimir Avila-Reese, and Octavio Valenzuela. “Substructure and halo density profiles in a warm dark matter cosmology”. In: *Astrophys. J.* 542 (2000), pp. 622–630. DOI: 10.1086/317057. arXiv: astro-ph/0004115.

[75] Steen Hannestad. "Massive warm dark matter". In: *arXiv e-prints*, astro-ph/0008451 (Aug. 2000), astro–ph/0008451. arXiv: astro-ph/0008451 [astro-ph].

[76] Scott Dodelson and Lawrence M. Widrow. "Sterile-neutrinos as dark matter". In: *Phys. Rev. Lett.* 72 (1994), pp. 17–20. DOI: 10.1103/PhysRevLett.72.17. arXiv: hep-ph/9303287.

[77] Alexey Boyarsky, Oleg Ruchayskiy, and Mikhail Shaposhnikov. "The Role of sterile neutrinos in cosmology and astrophysics". In: *Ann. Rev. Nucl. Part. Sci.* 59 (2009), pp. 191–214. DOI: 10.1146/annurev.nucl.010909.083654. arXiv: 0901.0011 [hep-ph].

[78] Katarina Markovič and Matteo Viel. "Lyman-\alpha Forest and Cosmic Weak Lensing in a Warm Dark Matter Universe". In: *Publ. Astron. Soc. Austral.* 31 (2014), e006. DOI: 10.1017/pasa.2013.43. arXiv: 1311.5223 [astro-ph.CO].

[79] Matteo Viel et al. "Constraining warm dark matter candidates including sterile neutrinos and light gravitinos with WMAP and the Lyman-α forest". In: *prd* 71.6, 063534 (Mar. 2005), p. 063534. DOI: 10.1103/PhysRevD.71.063534. arXiv: astro-ph/0501562 [astro-ph].

[80] Matteo Viel et al. "How cold is cold dark matter? Small scales constraints from the flux power spectrum of the high-redshift Lyman-alpha forest". In: *Phys. Rev. Lett.* 100 (2008), p. 041304. DOI: 10.1103/PhysRevLett.100.041304. arXiv: 0709.0131 [astro-ph].

[81] Julio F. Navarro, Carlos S. Frenk, and Simon D. M. White. "A Universal density profile from hierarchical clustering". In: *Astrophys. J.* 490 (1997), pp. 493–508. DOI: 10.1086/304888. arXiv: astro-ph/9611107.

[82] Uros Seljak, Anze Slosar, and Patrick McDonald. "Cosmological parameters from combining the Lyman-alpha forest with CMB, galaxy clustering and SN constraints". In: *JCAP* 10 (2006), p. 014. DOI: 10.1088/1475-7516/2006/10/014. arXiv: astro-ph/0604335.

[83] Matteo Viel et al. "Warm dark matter as a solution to the small scale crisis: New constraints from high redshift Lyman-α forest data". In: *Phys. Rev. D* 88 (2013), p. 043502. DOI: 10.1103/PhysRevD.88.043502. arXiv: 1306.2314 [astro-ph.CO].

[84] A. Garzilli et al. "How warm is too warm? Towards robust Lyman-α forest bounds on warm dark matter". In: *arXiv e-prints*, arXiv:1912.09397 (Dec. 2019), arXiv:1912.09397. arXiv: 1912.09397 [astro-ph.CO].

[85] Sinziana Paduroiu, Yves Revaz, and Daniel Pfenniger. "Structure formation in warm dark matter cosmologies: Top-Bottom Upside-Down". In: (June 2015). arXiv: 1506.03789 [astro-ph.CO].

[86] Florian Beutler et al. "The 6dF Galaxy Survey: baryon acoustic oscillations and the local Hubble constant". In: *mnras* 416.4 (Oct. 2011), pp. 3017–3032. DOI: 10.1111/j.1365-2966.2011.19250.x. arXiv: 1106.3366 [astro-ph.CO].

[87] Lauren Anderson et al. "The clustering of galaxies in the SDSS-III Baryon Oscillation Spectroscopic Survey: baryon acoustic oscillations in the Data Releases 10 and 11 Galaxy samples". In: *Mon. Not. Roy. Astron. Soc.* 441.1 (2014), pp. 24–62. DOI: 10.1093/mnras/stu523. arXiv: 1312.4877 [astro-ph.CO].

[88] Shadab Alam et al. "The clustering of galaxies in the completed SDSS-III Baryon Oscillation Spectroscopic Survey: cosmological analysis of the DR12 galaxy sample". In: *Mon. Not. Roy. Astron. Soc.* 470.3 (2017), pp. 2617–2652. DOI: 10.1093/mnras/stx721. arXiv: 1607.03155 [astro-ph.CO].

[89] Helion du Mas des Bourboux et al. "The Completed SDSS-IV Extended Baryon Oscillation Spectroscopic Survey: Baryon Acoustic Oscillations with Lyα Forests". In: *Astrophys. J.* 901.2 (2020), p. 153. DOI: 10.3847/1538-4357/abb085. arXiv: 2007.08995 [astro-ph.CO].

[90] Victoria de Sainte Agathe et al. "Baryon acoustic oscillations at z = 2.34 from the correlations of Lyα absorption in eBOSS DR14". In: *aap* 629, A85 (Sept. 2019), A85. DOI: 10.1051/0004-6361/201935638. arXiv: 1904.03400 [astro-ph.CO].

[91] Éric Aubourg et al. "Cosmological implications of baryon acoustic oscillation measurements". In: *Phys. Rev. D* 92.12 (2015), p. 123516. DOI: 10.1103/PhysRevD.92.123516. arXiv: 1411.1074 [astro-ph.CO].

[92] Christian Pedersen et al. "Massive neutrinos and degeneracies in Lyman-alpha forest simulations". In: *JCAP* 04 (2020), p. 025. DOI: 10.1088/1475-7516/2020/04/025. arXiv: 1911.09596 [astro-ph.CO].